UNIVERSITÄT FÜR BODENKULTUR WIEN
University of Natural Resources
and Life Sciences, Vienna

Master Thesis

Adaptation and Application of an Automated Avalanche Terrain Classification in Austria

submitted by

Christoph HESSELBACH, BSc

in the framework of the Master programme

Alpine Naturgefahren/

Wildbach- und Lawinenverbauung

in partial fulfillment of the requirements for the academic degree

Diplom-Ingenieur

Vienna, August 2023

Supervisor:

Priv.-Doz. Dipl.-Phys. Dr.techn. Jan-Thomas Fischer
Institute of Mountain Risk Engineering
Department of Civil Engineering and Natural Hazards

Affidavit

I hereby declare that I have authored this master thesis independently, and that I have not used any assistance other than that which is permitted. The work contained herein is my own except where explicitly stated otherwise. All ideas taken in wording or in basic content from unpublished sources or from published literature are duly identified and cited, and the precise references included.

I further declare that this master thesis has not been submitted, in whole or in part, in the same or a similar form, to any other educational institution as part of the requirements for an academic degree.

I hereby confirm that I am familiar with the standards of Scientific Integrity and with the guidelines of Good Scientific Practice, and that this work fully complies with these standards and guidelines.

Innsbruck, 15.08.2023 Christoph HESSELBACH (manu propria)

Acknowledgments

I am very thankful for completing my Master's thesis at the Austrian Forest Research Center (Bundesforschungszentrum für Wald, BFW), Institute of Natural Hazards, Snow and Avalanches Department, in collaboration with the Avalanche Warning Service (AWS) Tyrol.

I am deeply grateful to my supervisor and head of the Institute of Natural Hazards (BFW), Jan-Thomas Fischer. I express my special thanks and sincere appreciation to him. His invaluable guidance, ideas, and unwavering support have been crucial at every step of this research journey. His mentorship has contributed significantly to my academic growth by expanding my expertise. His guidance and encouraging words have been a constant inspiration.

My sincere thanks to Christoph Mitterer (AWS Tyrol) for initiating the project, Laura Stephan (AWS Tyrol) for preparing the reference data, and both Harvard B. Tøft (Norwegian Water Resources and Energy Directorate, NVE) and John Sykes (Chugach National Forest Avalanche Center, Alaska) for their invaluable contributions and resources that formed the cornerstone of my research.

A special acknowledgment is owed to my colleague Andreas Huber. His invaluable insights, advice, and ideas have enriched my work, deepened my understanding, and elucidated complex programming aspects crucial to this work. Additionally, I am grateful to him for his diligent proofreading of my work.

I would also like to thank all my colleagues, especially Michaela Teich, my team leader and Felix Oesterle, and my fellow students whose presence greatly enriched my journey.

My deepest gratitude goes to my Family and Girlfriend for their unwavering support. Their constant encouragement has been the driving force that kept me moving forward, especially during uncertain and exhausting moments.

Table of content

Kurzfassung

Die Avalanche Terrain Exposure Scale (ATES) klassifiziert die Exposition und Komplexität des Geländes in Bezug auf potenzielle Lawinengefahren in vier Klassen, von einfachem bis extremem Gelände. ATES-Karten unterstützen Personen oder Organisationen bei der Kommunikation, Planung und Durchführung von Freizeit- oder Berufsaktivitäten im Gelände. Der ursprünglich manuelle ATES-Workflow wurde durch automatisierte Prozesse ergänzt oder ersetzt, indem hochauflösende digitale Geodaten und kürzlich entwickelte Open-Source-Tools verwendet wurden. Diese Arbeit präsentiert eine Machbarkeitsstudie zur Anwendung und Bewertung einer automatisierten ATES-Klassifizierungsmethode für eine 700 km² große Pilotregion in Tirol, Österreich. Die Methode basiert auf frei verfügbaren Geodaten und umfasst drei Teilmodelle: (i) automatische Ausweißung potenzieller Auslösegebiete, (ii) Abgrenzung potenzieller Auslaufgebiete für Lawinen der Größe 3 (EAWS-Skala) mit Hilfe eines datenbasierten Simulationstools für gravitative Massenbewegungen (Flow-Py) und (iii) einen Klassifizierungs- und Kartierungsschritt. Im letzten Schritt werden die Resultate der Teilmodelle mit lokalen Hangneigungen, Waldbedeckungsgrad und vergletscherten Flächen kombiniert, um diskrete ATES-Klassen zu ermitteln. Es werden verschiedene Ansätze zur Parametrisierung von Teilmodellen untersucht und anhand von Referenzdaten bewertet. Die Studie zeigt, dass es eine Herausforderung ist, Auslaufwinkel mit verschiedenen Größenklassifizierungsansätzen in Einklang zu bringen. Die Bewertung von zwei ATES-Szenarien zeigt, dass ein weniger konservativer Ansatz zu einem differenzierten und ausgewogenen Kartenergebnis führt, das dem sehr komplexen Gelände Rechnung trägt. Die Anwendbarkeit des vorgestellten Arbeitsablaufs in der Pilotregion wird aufgezeigt, ebenso wie aktuelle Einschränkungen und potenzielle Verbesserungen, einschließlich der Segmentierung von Lawinenbahnen und der Wechselwirkungen zwischen Lawinen und Wald.

Schlüsselwörter: Lawine, Geländeklassifizierung, ATES, Flow-Py, potentielle Auslösegebiete

Abstract

The Avalanche Terrain Exposure Scale (ATES) classification categorizes the exposure and complexity of terrain concerning potential avalanche hazards into four classes, ranging from simple to extreme terrain. ATES maps support individuals or organizations in communicating, planning, and executing recreational or professional activities in alpine terrain. Since the mid-2000s, the ATES scheme has gained significance in North America and European mountain regions, but not in the Austrian Alps. The original manual ATES workflow has been complemented or replaced by automated processes utilizing high-resolution digital terrain data and recently developed open-source tools from various research groups. This thesis presents a feasibility study on the application and assessment of an automated ATES classification method for a 700 km^2 pilot region in Tyrol, Austria. The method is built upon freely available terrain data and comprises three sub-models: (i) automated delineation of potential avalanche release areas, (ii) identification of potential runout extents for size 3 avalanches (EAWS scale) using a data-based simulation tool for gravitational mass movements (Flow-Py), and (iii) a classification and mapping step. In the last step, the sub-model results are combined with the local slope angle, degree of forest cover, and glaciated areas to determine discrete ATES classes. Various sub-model parameterization approaches are explored and assessed using reference data. The study reveals challenges in aligning runout angles with different size classification approaches. The assessment of two ATES scenarios shows that a less conservative approach yields a differentiated and balanced map result, accounting for the highly complex terrain. The applicability of the presented workflow in the pilot region is demonstrated, along with current limitations and potential improvements, including avalanche path segmentation and avalanche-forest interactions.

Keywords: Avalanche, Terrain Classification, ATES, Flow-Py, Potential Release Areas

1 Introduction and motivation

The classification and delineation of avalanche-prone terrain is a valuable safety tool for individuals and organizations. It facilitates efficient communication, planning, and execution of recreational or professional activities in alpine environments (McClung & Schaerer, 2006). Over the past two decades, several classification schemes and resulting map products have been published focusing on the classification and mapping of avalanche terrain to improve and contribute to more safe navigation in the backcountry (Campbell & Gould, 2013; Harvey et al., 2018; Larsen et al., 2020; Schmudlach & Köhler, 2016; Schumacher et al., 2022; Statham et al., 2006). The large-scale automatic assessment of avalanche terrain has been made possible by the increasing availability of high-quality digital elevation models in combination with innovative geographic data analysis, especially for remote areas with insufficient field or historical avalanche data (Sharp, 2018). The capability of the different models to work at a regional or even national scale with minimal human input greatly decreases the cost and time to produce spatial information (Bühler, von Rickenbach, Christen, et al., 2018).

One foundational framework for terrain classification is the Avalanche Terrain Exposure Scale (ATES) introduced by Statham et al. in (2006). The ATES scheme provides a standardized framework to enhance the communication and evaluation of the terrain complexity, along with the potential risks associated with travel in alpine regions, particularly concerning avalanches and related hazards. The ATES terrain classes encompass simple (class 1), challenging (class 2), and complex (class 3) terrain categories. Recent developments have introduced an additional class for extreme terrain (class 4) (AAA, 2023). The ATES scheme has established the foundation for the automated delineation of distinct terrain classes concerning avalanche-prone terrain in Norway, utilizing open-source tools (Larsen et al., 2020; Schumacher et al., 2022).

Additionally, there exist other products, particularly for the Swiss Alps, designed to enhance safe navigation in the backcountry (Harvey et al., 2018; Schmudlach et al., 2018). Nevertheless, these products are either unavailable for Austria (Harvey et al., 2018; Larsen et al., 2020; Schumacher et al., 2022) or their workflow, or certain components of it, are not openly accessible (Harvey et al., 2018; Schmudlach & Köhler, 2016). This limitation hinders the thorough application and investigation of these products for Austria. This paves the way for the current study, which aims to assess and adapt an automated avalanche terrain classification scheme for a study area in Austria. The open-source terrain classification method introduced by Larsen et al. (2020) forms the base for this endeavor.

Figure 1: Symbolic illustration of the ATES classification applied on the terrain (left, picture: Lukas Ruetz), followed by its conversion into a two-dimensional map product (right).

The core motivation behind this study is to apply a methodology for classifying mountainous terrain prone to avalanches for a high-alpine test area of approximately 700 km^2 in the Central Alps (Sellrain in Tyrol, Austria). This study's underlying framework is based on utilizing open-source tools and geospatial data. The terrain classification focuses on incorporating regional avalanche mobility simulations and emphasizing the assessment of large-sized avalanches, considering their significant contribution to most avalanche-related incidents (EAWS, 2023). The novelty of this endeavor in the Austrian Alps underscores its motivational significance.

This thesis's main objective is to adapt and apply the model chain of the autoATES terrain classification (Larsen et al., 2020; Schumacher et al., 2022) to a study area in Austria. The model chain encompasses three sequential steps, each progressively building upon the preceding one. Each model step is subjected to individual testing and discussion in alignment with its respective sub-objectives. The model steps and their corresponding objectives of this thesis include:

(1) **PRA delineation**

Parameterization of the PRA model (Sharp, 2018; Sykes et al., 2022; Veitinger et al., 2016) to realistic delineate potential release areas (PRAs) within the study area (Section 4.1)

This is achieved by comparing three PRA model configurations, focusing on roughness parameter with the Swiss reference dataset of observed release areas. The plausibility is determined by assessing statistical skill scores. Within the application to the study area, the forestation effect is qualitatively assessed, and the final parameterization for the model chain is determined.

(2) **Avalanche mobility model**

Assessment of the data-based avalanche mobility model (D'Amboise, Neuhauser, et al., 2022) for regional runout modeling size three avalanches for the ATES terrain classification (Section 4.2)

This is achieved by three comparative optimization analyses (OA). OA 1 involves an investigation of various Flow-Py parameters using an avalanche reference dataset (Section 3.2.2) as a reference, which includes 19 mapped avalanche outlines in the study area. By qualitatively analyzing the impacts of these parameters, the primary aim of this OA is to determine an appropriate exponent parameter for further investigations.

OA 2 aims to assess the feasibility of utilizing a single alpha angle for back-calculating the travel lengths of the 19 reference avalanches. Plausibility is quantitatively assessed through the computation of the root mean square error (RMSE) for each set of avalanche simulations corresponding to different alpha angles.

OA 3 involves a quantitative comparison of 100 randomly selected avalanche simulations across the study area using discrete avalanche size classification ranges for travel length, impact pressure, and affected area. The goal is to evaluate the extent to which the modeled avalanches correspond to the specified size categories.

(3) **ATES classification**

Application and adaptation of the ATES classifier (Larsen et al., 2020; Schumacher et al., 2022) for size three avalanches in the study area (Section 4.3)

This is achieved by incorporating the findings of the PRA and the avalanche mobility model steps and a subsequent discussion on the ATES classification parameters and thresholds, such as for slope angle, avalanche runout, overhead hazard, and forestation.

To address the research objectives, the thesis is structured into the following sections:

Section 2, Theory, serves as an introduction to snow avalanches, providing foundational knowledge. It also explores diverse avalanche terrain classification methods, including recent automated approaches, laying the groundwork for the subsequent analysis.

In Section 3, Study area and data, detailed insights into the study area, and the data employed in this thesis are presented. It outlines the sources of data and information crucial for the research.

The subsequent Section 4, Application and testing of the model chain, provides detailed information on the application and testing of the model chain. This encompasses assessing the sequential model chain steps, such as the PRA model, avalanche mobility model, and ATES classification.

Section 4.3.2, Discussion of the model chain results, engages in a comprehensive analysis and discussion of the outcomes derived from the model chain. It delves into the implications of the results and offers interpretations that shed light on their significance.

The thesis concludes with Section 5, Conclusion and outlook, with a summary of the key findings, their significance, and potential future directions for research and application.

2 Theory

In the majority of snow-covered mountain environments around the globe, snow avalanches, hereafter called avalanches, pose a considerable natural hazard. They are rapidly flowing, down-slope snow mass movements driven by gravity. Furthermore, avalanches can entrain ice, soil, vegetation, or rocks. They are considered meteorologically driven hazards (Schweizer et al., 2003, 2015).

The introductory section of the theory chapter highlights the fundamental aspects essential for the automated classification of avalanche terrain. It starts by introducing two approaches to avalanche classification: the first approach focuses on genetic avalanche characteristics, which involves understanding the origin of avalanches and the factors that contribute to their formation, while the second approach revolves around avalanche terrain characteristics, specifically the morphological classification. Furthermore, different size classification schemes are introduced. The chapter reviews other concepts for delineating potential release areas (PRAs). It presents the two approaches for avalanche mobility modeling, essential for automated model chains for avalanche terrain classification. The chapter concludes with a literature review covering different avalanche terrain classification approaches, ranging from manual route classification and maps to automated model chains for avalanche terrain classifications.

2.1 Avalanche formation

The avalanche formation is a widely discussed topic, and various models for release mechanisms have been established. Schweizer (1999), Schweizer et al. (2003), McClung & Schaerer (2006), and Rudolf-Miklau & Sauermoser (2011) provide a comprehensive overview of these models. The avalanche formation factors (Schweizer et al., 2003) roughly align with the genetic avalanche classification (UNESCO, 1981).

For an avalanche to be triggered, it is mechanically essential for the stress within the snowpack to reach or surpass the strength of the snow. This can occur due to various additional loadings, such as new snow deposition, increased density due to sudden warming events, or human impacts (McClung & Schaerer, 2006).

According to Schweizer et al. (2003), avalanche formation is the result of a complex interaction between (1) snowpack, (2) meteorological, and (3) terrain conditions. However, meteorological and snow cover parameters respond dynamically to meteorological conditions and are subject to short-term variations (Veitinger & Sovilla, 2016). A comprehensive review is stated in Schweizer et al. (2003) and McClung &

Schaerer (2006). Terrain parameters, in contrast can be regarded as broadly constant; moreover, they can be derived from digital elevation models (DEMs) (Bühler et al., 2013; Maggioni & Gruber, 2003; Schweizer et al., 2003; Veitinger et al., 2016) and satellite data (Bühler et al., 2013; Sykes et al., 2022). The following section will outline the contributing factors to avalanches, with a specific focus on terrain-related factors. A thorough examination is presented in the mentioned literature.

(1) **Snowpack**

The contributing factors related to the snowpack can be categorized into two components: the snowpack stratigraphy, the presence or absence of a weak layer, and its spatial distribution. A comprehensive introduction to the contributing factors for avalanches related to the snowpack is stated in Schweizer et al. (2003).

(2) **Meteorology**

The meteorological factors cover new snow, wind, and the radiation balance of the snowpack. High accumulations of new snow play an essential role in the avalanche formation. They are associated with large and catastrophic avalanche events (Schweizer et al., 2015). In addition, wind-terrain interaction is a crucial factor in avalanche formation. On wind-exposed "windward" slopes, avalanches are less likely than on wind-protected "leeward" slopes (Gauer, 2001). Other significant meteorological interactions are the temperature, the slope aspect, and the altitude itself (McClung & Schaerer, 2006).

(3) **Terrain**

The inclination of the terrain slope strongly influences the potential avalanche release areas (Voellmy, 1955). McClung & Schaerer (2006) state that most avalanches are initiated at slopes from 35-45°. Research on avalanche occurrence in Switzerland and Canada has revealed that the first quartile for avalanche release is 37°, the median is 39°, and the third quartile is 41° (Schweizer & Jamieson, 2001). Munter (1997) states that on slopes steeper than 60°, avalanches are widespread but minor in size since no significant snow accumulation is possible. In addition to that, on slopes below 30°, the gravitational forces are too weak to cause an avalanche. However, if the liquid water content within the snowpack is high enough, a wet-snow avalanche can initiate at inclinations below 25° (Schweizer et al., 2015).

The morphology of the terrain affects the occurrence of avalanches. In general, convex slopes are generally considered less prone to avalanches (Maggioni & Gruber, 2003). Furthermore, the slope's roughness significantly influences stabilization forces (McClung, 2001) and the formation and spatial distribution of weak layers. However, while the terrain roughness still supports the stability of a shallow snowpack, the effects can be neglected for a thicker snowpack (Schweizer et al., 2003).

Schweizer et al. (2003) review that the presence of a dense forest plays a crucial role in reducing the likelihood of an avalanche initiation. Forests alter the accumulation and distribution of snow. The canopy of trees also regulates the incoming and outgoing radiation, which influences or even limits the formation of surface hoar and faceted crystals, which are highly related to the formation of weak layers (McClung & Schaerer, 2006; Schweizer et al., 2003). The physical barriers of tree stem can increase the friction on susceptible slopes to some extent and stabilize the snowpack (Teich et al., 2014). Therefore, forests are essential for avalanche mitigation measures (Bebi et al., 2001). However, if the potential impact of an large avalanche exceeds the stability of the forest, the trees hardly affect the avalanche. Large and extremely large avalanches can break single trees or destroy whole forests. The trees can also be entrained, causing a greater mass and, thus, a more significant potential for damage (McClung & Schaerer, 2006).

2.2 Avalanche terrain

As avalanches descend down-slope, they adhere to distinct routes known as avalanche paths. These paths can span across the entirety of a mountain slope or affect only a limited portion. When an area encompasses one or more avalanche paths, it is referred to as avalanche terrain (McClung & Schaerer, 2006). The avalanche path is divided into a (1) starting zone, (2) track, and (3) runout zone. Along an avalanche path, different avalanches with varying sizes can originate from different starting zones, each with its own track and runout zone (McClung & Schaerer, 2006). The Avalanche Atlas (UNESCO, 1981) includes these zones in its morphological classification and assesses attributes along the avalanche path.

2.2.1 Release area

The starting zone, also referred to as avalanche release area or zone of origin, is the area where the initial snow mass starts to move down-slope. It is subsequently referred to as release areas. The classification scheme (UNESCO, 1981) distinguishes between the manner of starting, the position of the sliding surface, and the liquid water content.

The characteristic of the different release mechanism involves different complex processes and will be mentioned briefly in this thesis. McClung & Schaerer (2006) and Schweizer et al. (2003, 2015) comprehensively review the different types and processes involved in the avalanche release process. In general, two main types can be distinguished based on the manner of release shape: loose snow avalanches and slab snow avalanches (Figure 2). Loose snow avalanches (Figure 2, left image) occur as a point release in or on the surface layer of relatively poor cohesive dry or wet snow. Loose snow avalanches gain mass as they move down-slope in a triangular shape (McClung & Schaerer, 2006; Schweizer et al., 2003).

The slab avalanches (Figure 2, right image) approximate a rectangle shape and leaves a typical fracture line, the crown, delineating the upper part of the starting zone (McClung & Schaerer, 2006). The release of a slab avalanche involves a cohesive snow layer, the slab, which can be dry or wet. Slab avalanches are associated with a weak layer's initial failure and the fracture's propagation within the weak layer. A broad introduction to the topic of weak layer and avalanche formation is presented in Schweizer et al. (2003). A detailed review of wet-snow slab and glide snow avalanches can be found in Mitterer & Schweizer (2013).

Figure 2: Two types of avalanche release characteristics, loose snow avalanche (left) and slab avalanche (right). Pictures: EAWS (2023)

2.2.2 Transition zone

The transition zone, track, or path of avalanches, hereafter referred to as avalanche path, links the release area and the runout zone. According to avalanche classification (UNESCO, 1981), paths can be categorized as unconfined or channelized. While the path is a prominent terrain feature for larger avalanches, it may be less present in unconfined or smaller avalanches with shorter travel distances.

As the avalanche flow intensifies at the beginning of the track and diminishes towards its end, the maximum velocity of the avalanche is typically reached within the track (McClung & Schaerer, 2006). Unless hindered by narrow gullies or rough terrain features, significant accumulation of avalanche debris does not typically occur in the path after an avalanche event (UNESCO, 1981).

In mountainous regions, avalanche paths are often identified by areas devoid of trees within forested regions. Tree vegetation's presence or absence can offer valuable insights into avalanche frequency (Nairz et al., 2011).

Regarding movement, avalanches can occur as dense snow avalanches or powder snow avalanches (UNESCO, 1981). Dense snow avalanches primarily follow the terrain's morphology in their flow path. In contrast, the path of a powder snow avalanche is less constrained by the terrain, as the powder cloud can easily flow over terrain features (Sauermoser et al., 2014).

Concerning the movement, avalanches can occur as dense snow avalanches or powder snow avalanches. In the case of dense snow avalanches, the flow path is predominantly determined by the terrain's morphology. The terrain less influences the path of powder snow avalanche as the powder cloud easily overflows terrain features (Sauermoser et al., 2014).

2.2.3 Runout area

In general, the runout area is the area where avalanche debris accumulates due to a decrease in energy caused by friction. The extent of the runout can vary for each avalanche along the same path. For powder avalanches, the runout area is determined by the sedimentation of the snow cloud (UNESCO, 1981). According to Gruber et al. (1999), a rough estimate of a 10° slope angle signifies the point at which large dry slope avalanches start decelerating and reducing their movement. However, it should be noted that smaller avalanches can deposit even at steeper slope inclinations, while larger avalanches tend to roll over them. Consequently, achieving precise classification becomes challenging (Nairz et al., 2011).

2.3 Avalanche size classification

A standardized framework for the wide range of avalanche sizes, serves to establish consistent criteria for assessing and categorizing avalanches. Such a framework enables researchers, practitioners, and stakeholders to compare and contrast avalanche events, and examine the specific characteristics associated with each avalanche size category (McClung & Schaerer, 2006).

Several size classification systems are currently in use since there has yet to be an internationally standardized approach for classifying avalanche sizes. One such system is the Canadian Avalanche Association (CAA, 2016) classification, which categorizes avalanches into five classes based on their destructiveness, see Table 1. This system provides a qualitative description of the potential damage caused by avalanches to individuals, vegetation, infrastructure, and settlements. Additionally, the system provides quantitative parameters such as typical mass [t], impact pressure [kPa], and path length [m].

The CAA classification system was adopted and calibrated by Perla & Martinelli (1976) and McClung & Schaerer (1980).

Table 1: Avalanche size classification after CAA (2016)

Size	Destructive potential	Typical mass [t]	Typical path length [m]	Typical impact pressure [kPa]
D-1	Relatively harmless to people.	< 10	10	1
D-2	Could bury, injure, or kill a person.	100	100	10
D-3	Could bury and destroy a car, damage a truck, destroy a wood-frame house or break a few trees.	1,000	1,000	100
D-4	Could destroy a railway car, large truck, several buildings or a forest area of approximately 4 hectares.	10,000	2,000	500
D-5	Largest snow avalanche known. Could destroy a village or a forest area of approximately 40 hectares	100,000	3,000	1,000

Table 2: Avalanche size classification after AAA (2016)

Size	Avalanche size
R-1	Very small, relative to the path
R-2	Small, relative to the path
R-3	Medium, relative to the path
R-4	Large, relative to the path
R-5	Major or maximum, relative to the path

Table 3: Avalanche size classification after Bühler et al. (2019)

Size	Affected area [m^2]
Small	≤ 500
Medium	> 500 & $\leq 10{,}000$
Large	$> 10{,}000$ & $\leq 80{,}000$
Very large	$> 80{,}000$ & $\leq 500{,}000$
Extremely large	$> 500{,}000$

The American Avalanche Association (AAA, 2016) has implemented a separate classification scheme based on avalanche dimensions, specifically volume and, travel length, in relation to the slope (Perla & Martinelli, 1976). The AAA classification is stated in Table 2. This classification system comprises five classes, ranging from very small to major. Unlike other schemes, the size classification in relation to the path enables the comparisons and assessments of different avalanche events along the same path rather than different avalanches from different locations (McClung & Schaerer, 2006).

Table 4: Avalanche size classification after EAWS (2023)

Size	Potential damage	Run out	Typical length [m]	Typical volume [m³]
Small (Sluff) **E-1**	Unlikely to bury a person, except in run out zones with unfavorable terrain features (e.g. terrain traps). In extremely steep terrain, the danger of deep falls prevails the danger of burials.	Stops within steep slopes.	10 - 30	100
Medium **E-2**	May bury, injure or kill a person. Size 2 corresponds to the typical skier-triggered avalanche.	May reach the end of the relevant steep slope.	50 - 200	1,000
Large **E-3**	May bury and destroy cars, damage trucks, destroy small buildings and break a few trees. When skiers are caught by avalanches of this size, probability for severe consequences are very high.	May cross flat terrain (well below 30°) over a distance of less than 50 m.	several 100	10,000
Very large **E-4**	May bury and destroy trucks and trains. May destroy fairly large buildings and small areas of forest. Very large avalanches may occur at danger level 3-Considerable and are typical during periods with danger levels 4-High and 5-Very High.	Crosses flat terrain (well below 30°) over a distance of more than 50 m. May reach the valley floor.	1000 - 2,000	100,000
Extremely large **E-5**	May devastate the landscape and has catastrophic destructive potential. Typical for danger level 5-Very High.	Reaches the valley floor. Largest known avalanche.	$>$ 2000	$>$ 100000

The size classification of the European Avalanche Warning Services EAWS (2023) shares the same size classes as the CAA scheme but exhibit slight differences in their specific values and parameters. The EAWS has adapted this system by incorporating a more qualitative approach. The scheme incorporates a semi-quantitative parameter for the runout classification. Additionally, EAWS employs a volume-based [m³] parameter instead of mass [t] and describes path length [m] using typical ranges rather than typical values. The destructiveness is only classified with a description, which aligns with the CAA but does not provide typical values for the impact pressure.

According to the glossary of the EAWS (2023), an *avalanche* is defined as a rapidly moving mass of snow with a volume exceeding 100 m³ and a minimum length of 50 m. Smaller avalanches are referred to as "sluff" or small avalanches, representing the first size class in the EAWS size classification. The subsequent size classes are medium (size 2), large (size 3), very large (size 4), and extremely large (size 5). According to the EAWS, avalanches of sizes 2 and 3 are considered the most fatal for skiers, whereas avalanches of the size classes 4 and 5 threaten infrastructure and settlements. Table 3 represents the EAWS size classification.

In recent studies, Bühler et al. (2019) introduced a size classification parameter based on the affected area of avalanches (Table 3). Using satellite imagery, the authors employed this parameter to classify and analyze more than 18,000 mapped avalanches.

2.4 Introduction to automated avalanche terrain classification

Over the past two decades, several classification systems and resulting map products have been published focusing on the classification and mapping of avalanche terrain to improve and contribute to a more safe navigation in the backcountry (Campbell & Gould, 2013; Harvey et al., 2018; Larsen et al., 2020; Schmudlach & Köhler, 2016; Schumacher et al., 2022; Statham et al., 2006).

The following section provides an overview of existing classification and mapping methods as well as available products for mountain terrain prone to avalanches (Table 5). The autoATES approach presented by Larsen et al. (2020) is discussed in more detail, given its relevance for testing and applying within the Austrian study area.

The large-scale assessment of avalanche terrain has been made possible by the increasing availability of high-quality digital elevation models in combination with innovative geographic data analysis, especially for remote areas with insufficient field or historical avalanche data (Sharp, 2018). The capability of the different models to work at a regional or even national scale with minimal human input greatly decreases the cost and time to produce spatial information, which can help professionals and recreationists improve judgments regarding their exposure to avalanche hazards (Bühler, von Rickenbach, Christen, et al., 2018).

The Avalanche Terrain Exposure Scale (ATES), developed by Statham et al. (2006), provides a standardized framework to enhance the communication and evaluation of the complexity and potential risks associated with travel in alpine terrain. Following the classic ski area difficulty scale, they assigned a difficulty level to well-known backcountry routes. The scale ranges from simple (class 1), challenging (class 2), and complex (class 3). The recent development incorporates additional classes for extreme terrain (class 4) and an optional class 0 for non-avalanche terrain (AAA, 2023). The methods include geographic data analysis, visually interpreted aerial photographs, local expertise, and field assessments. Statham et al. (2006) develop two outcomes: the ATES Public Communication Model (Table 5) and the ATES Technical Model (Table 6). The former is intended to provide a simple, easy-to-read overview for the public; the latter contains more detailed information about the scheme's application for experienced and professional users.

Table 5: ATES Public Communication Model (v.1/04) (Statham et al., 2006); the extreme class (4) is adapted from Statham (2020)

Description	Class	Terrain Criteria
Simple	1	Exposure to low angle or primarily forested terrain. Some forest openings may involve the runout zones of infrequent avalanches. Many options to reduce or eliminate exposure. No glacier travel.
Challenging	2	Exposure to well defined avalanche paths, starting zones or terrain traps
Complex	3	Exposure to multiple overlapping avalanche paths or large expanses of steep, open terrain
Extreme	4	Exposure to very steep faces with cliffs, spines, couloirs, crevasses or sustained overhead hazard. No options to reduce exposure and even small avalanches can be fatal

Table 6: ATES Technical Model (v.1/04) (Statham et al., 2006)

	Simple (Class 1)	**Challenging (Class 2)**	**Complex (Class3)**
Slope angle Angles	generally $<$ 30º	Mostly low angle, isolated slopes $>$35º	Variable with large % $>$35º
Slope shape	Uniform	Some convexities	Convoluted
Forest density	Primarily treed with some forest openings	Mixed trees and open terrain	Large expanses of open terrain. Isolated tree bands
Terrain traps	Minimal, some creek slopes or cutbanks	Some depressions, gullies and/or overhead avalanche terrain	Many depressions, gullies, cliffs, hidden slopes above gullies, cornices
Avalanche frequency (events:years)	1:30 ≥ size 2	1:1 for $<$ size 2 1:3 for ≥ size 2	1:1 $<$ size 3 1:1 ≥ size 3
Start zone density	Limited open terrain	Some open terrain. Isolated avalanche paths leading to valley bottom	Large expanses of open terrain. Multiple avalanche paths leading to valley bottom
Runout zone characteristics	Solitary, well defined areas, smooth transitions, spread deposits	Abrupt transitions or depressions with deep deposits	Multiple converging runout zones, confined deposition area, steep tracks overhead
Interaction with avalanche paths	Runout zones only	Single path or paths with separation	Numerous and overlapping paths
Route options	Numerous, terrain allows multiple choices	A selection of choices of varying exposure, options to avoid avalanche paths	Limited chances to reduce exposure, avoidance not possible
Exposure time	None, or limited exposure crossing runouts only	Isolated exposure to start zones and tracks	Frequent exposure to start zones and tracks
Glaciation	None	Generally smooth with isolated bands of crevasses	Broken or steep sections of crevasses, icefalls or serac exposure

Delparte (2008) extends the consideration of individual routes to a spatial classification using geographic data analysis and determines that the slope and forest density significantly influence the ATES model. . Campbell and Gould (2013) introduce a zonal ATES model based on a semi-automated geographic data classification method with quantified ATES parameters (Statham et al., 2006). The method primarily emphasizes slope angle and forest density in assessing avalanche terrain exposure.

Table 7: Overview of areal coverage and accessibility across different avalanche terrain classification approaches

Author	Product	Areal coverage	Map view	Open accessible method
Larsen et al. (2020)	autoATES	Norway	temakart.nve.no	yes
Harvey et al. (2018)	CAT/ATHM	Swiss	map.geo.admin.ch	no
Schmudlach & Köhler (2016)	Skitourenguru	Alps	info.skitourenguru.ch	no

2.4.1 autoATES

Larsen et al. (2020) introduce an automated process chain, the autoATES model, for classifying avalanche terrain in Norway. The autoATES model is based on the quantitative zonal model proposed by Campbell and Gould (2013). The product availability is stated in Table 5.

The automated terrain classification process consists of three main steps. The first step involves the delineation of PRAs (Veitinger et al., 2016). The second step incorporates an avalanche mobility model to estimate potential runouts, the TauDEM model (Tarboton, 2005). In the last step, a comprehensive classification is performed using the so called *ATES classifier*. This step combines information from PRAs, modeled runout areas, and local slope gradient is combined. Two avalanche mobility scenarios are integrated, each interpreted to represent different frequencies of avalanche occurrence. The first scenario encompasses avalanches with a runout angle (alpha angle) of 18°, while the second scenario encompasses avalanches with an alpha angle of 23°. The resulting map product presents four ATES classes, ranging from class 0 (non-avalanche terrain), class 1 (simple terrain), class 3 (challenging terrain), and class 4 (complex terrain). The process chain is applied to map an area of over 365,000 km^2, encompassing the Norwegian mainland and nearby coastal islands. The input data is a digital terrain model (DTM) with a resolution of 10 m.

However, the maps had some limitations: Due to the need for more suitable forest data, the focus is shifted to areas above the tree line, which still accounts for 70% of the Norwegian backcountry terrain. Additionally, the algorithm does not account for overhead exposure to hazards, and the simulation of avalanches encountered difficulties in adequately representing flat runout areas (Schumacher et al., 2022).

Schumacher et al. (2022) updated the autoATES by integrating an enhanced PRA delineation (Sharp, 2018), as stated in Section 2.5.1.2, and included forest data in the terrain classification step. Moreover, the TauDEM model is replaced with the Flow-Py avalanche mobility model (D'Amboise, Neuhauser, et al., 2022). The forest advancements are facilitated by the forthcoming availability of spatial forest data derived from the National Forest Inventory of Norway (Breidenbach et al., 2020).

Schumacher et al. (2022) compare the updated model chain with the autoATES approach of Larsen et al. (2020) compared the results with 52 manual classified ski routes created by local experts as a reference. The study area covers approximately 3,200 km². The results indicate that incorporating forest data improves the accuracy of the process chain and contributes to a more realistic classification of the avalanche terrain. For example, the proportion of incorrectly classified terrain classes is reduced. The overall improvement increased by up to 12% compared to the model with no forest implementation.

The most recent adaptations of the model chain incorporate additional features such as an overhead hazard parameter and the inclusion of an extreme terrain class. These modifications are currently in the development phase. The overhead hazard parameter assesses and accounts for potential hazards originating from higher elevations in the terrain. In contrast, the newly introduced extreme terrain class (AAA, 2023; Statham, 2020) enables the characterization and analysis of particularly steep and hazardous terrain conditions.

2.4.2 CAT and ATHM

Harvey et al. (2018) propose an alternative method for classifying avalanche terrain. The authors highlight that too many tours are categorized as complex within the ATES system for the Swiss Alps. To address this, they introduce an automated geographic data analysis classification workflow, creating two map products for the Swiss Alps and Jura regions. The emphasis is placed on common skier-triggered avalanches, with a maximum size classification of 3. The resulting maps have a spatial resolution of 5 m. The product availability is stated in Table 5.

The initial map product, known as *classified avalanche terrain* (CAT), encompasses multiple components such as PRAs, modeled avalanche runout zones for avalanches of the size 3 with a release height of 0.5 m, and areas susceptible to remote avalanche triggering. This map is designed to offer both qualitative and quantitative insights into the spatial arrangement of avalanche hazards. Harvey et al. (2018) incorporate several key elements in developing the CAT map. The PRAs are identified using the approach proposed by Bühler et al. (2013; 2018). These PRAs serve as input for avalanche runout simulations. To carry out avalanche runout simulations, Harvey et al. (2018) utilize the process-based avalanche simulation tool RAMMS::EXTENDED (Bartelt et al., 2012, 2016), which is based on the work of Christen et al. (2010). In their study, approximately 860,000 individual avalanche simulations are performed within the study area. Determining remote triggering potential is grounded in analyzing 75 case studies of avalanches triggered remotely.

The second map product, *avalanche terrain hazard maps* (ATHM), focuses on the potential consequences of being caught in an avalanche. The ATHM provides continuous spatial information on the hazard level of the terrain. This data is generated by amalgamating avalanche deposit depth and pressure information with a fall trajectories model.

2.4.3 Skitourenguru

The Skitourenguru (Schmudlach & Köhler, 2016) provides two products aiming to provide a planning and communication tool for traveling in the backcountry: first, a spatial map product, and subsequently, a ski route planning tool. This review focuses on the map product. Schmudlach & Köhler (2016) developed a fully automated classification method for avalanche terrain at a national level. The product availability is stated in Table 5.

The approach distinguishes itself from previously mentioned products by assessing the relevant terrain from the skier's perspective (point of view) and exposure to avalanches or risks due to terrain characteristics impacting the point of view rather than calculating avalanche propagation models. If the current point of view is on a steep slope, for example, the terrain evaluation focuses more on the upward and downward perspectives. In contrast, all surroundings are equal in flat terrain, and the relevant slope area becomes a circle. As soon as the relevant slope area is defined, the algorithm further analyzes the terrain by following these steps: analyzing the slope characteristics and determining the level of danger based on the adapted ATES criteria. In contrast to the discrete ATES classes, this procedure is applied individually to each cell of a raster with a 10-meter cell size, resulting in a continuous ATES-rated hazard map. For instance, steeper slopes are assigned a higher hazard rating than flatter ones.

Subsequently, Schmudlach et al. (2018) introduced an optional step involving the computation of dynamic risk maps using real-time avalanche forecast data and a quantitative risk reduction approach. This process requires converting avalanche forecast data into continuous spatial map information, specifically focusing on key terrain attributes such as altitude and aspect.

2.5 Components for automated avalanche terrain classifications model chains

Automated model chains have been developed and utilized to capture and delineate avalanche terrain effectively, encompassing multiple avalanche paths with various avalanche release, transition, and runout areas (Campbell & Gould, 2013; Harvey et al., 2018; Larsen et al., 2020; Schmudlach & Köhler, 2016; Schumacher et al., 2022).

The main emphasis of this chapter lies in the methodology of the autoATES model proposed by Larsen et al. (2020), as it is subject to testing and application within the context of the present thesis for a study area in Tyrol.

The structure of this chapter follows the framework of the autoATES model. It begins with a brief introduction to the automated delineation of PRAs, followed by a deeper insight into the PRA model (Sharp, 2018; Veitinger et al., 2016), which is part of the autoATES model. The subsequent section focuses on the various methods used to calculate avalanche runouts, explicitly emphasizing the Flow-Py model (D'Amboise, Neuhauser, et al., 2022), constituting the second step in the autoATES model. In addition to the main components of avalanche terrain classification, such as PRAs and avalanche mobility, other factors are also considered in certain studies. Harvey et al. (2018), for instance, incorporate the assessment of potential hazards like remote triggering, deep burial, or serious injury resulting from a large fall. Lastly, the chapter examines the terrain classification steps, representing the model chain's final step.

2.5.1 PRA models

Potential release areas (PRA) are specific slope sections susceptible to avalanche release due to the factors contributing to avalanche formation described in Section 2.1. The spatial information about the PRAs and the different factors contributing to avalanche formation is crucial for understanding avalanches and developing automated assessment and mapping of the avalanche terrain (Bühler et al., 2013).

As stated in Section 2.1, terrain parameters can be regarded as broadly constant. Consequently, terrain parameters serve as the foundation for algorithms developed for automated PRA delineation. The different approaches use a combination of different derivations of a DEM, such as slope angle, curvature, roughness, and aspect. The spatial extents of avalanche release areas, calculated through PRA models, serve as input for numerical avalanche simulations or enhance terrain assessments with additional spatial information (Sykes et al., 2022).

In early stages of avalanche research, Voellmy (1955) discovered that the slope angle of the terrain is essential for determining PRAs. He stated that terrain areas with a slope angle ranging from 28°-60° are highly susceptible to avalanche releases. Munter (1997) emphasized that snow slab avalanches occur when gravity in the snowpack exceeds shear forces, which is rarely the case below 28°. On steeper slopes beyond 60°, on the other hand, avalanches often occur, but only to a small extent, as the slopes are too steep to accumulate large amounts of snow.

Based on topographic factors and the analysis of documented avalanche events, Maggioni et al. (2002) developed a geographic data analysis to identify PRAs. Maggioni and Gruber (2003), Maggioni (2005) as well as the findings by Ghinoi and Chung (2005) subsequently addressed the topic and established the basis for future approaches (Bühler et al., 2013; Pistocchi & Notarnicola, 2013; Veitinger et al., 2016). By analyzing documented avalanche occurrence and frequency, Maggioni and Gruber (2003) determined that terrain parameters that can be derived from DEM, such as slope, curvature, aspect, and ridge distance, significantly influence avalanche release susceptibility.

Two primary models for PRA delineation are utilized in the mentioned classification approaches in Section 2.4. The classification method proposed by Harvey et al. (2018) incorporates the PRA model introduced by Bühler et al. (2013; 2018), while the model chain developed by Larsen et al. (2020) incorporates the PRA model of Veitinger et al. (2016).

The main distinction between these two PRA models is that Bühler et al. (2013; 2018) identify individual PRAs in a vector data format. The algorithm introduced by Veitinger et al. (2016) generates a raster data layer. In this format, each cell is assigned a value on a scale from 0, representing no potential for avalanche release, to 1, indicating a high potential for avalanche release. Importantly, this approach does not delineate individual PRAs.

2.5.1.1 PRA delineation after Bühler et al. (2013)

Bühler et al. (2013) conducted a study on identifying individual PRAs. Their algorithm is validated using a dataset of observed avalanche release areas near Davos, Switzerland (CH ORA Dataset, Section 3.2.1). The delineation process involves parameters such as slope, curvature, and roughness. Forested areas are excluded from the PRAs using a binary forest layer. The separation into individual PRAs is done with a flow direction algorithm.

Building upon this research, Bühler et al. (2018)enhanced the PRA separation process by incorporating object-based image analysis (OBIA) techniques (Blaschke, 2010).

For the PRA identification process, Harvey et al. (2018) redefine the approach of Bühler et al. (2018) by replacing the simple curvature parameter with the fold parameter. The parameter was introduced by

Schmudlach & Köhler (2016) to quantify the significant changes in terrain morphology, such as gullies and crest lines, by determining the maximum curvature in each dimension. To optimize the delineation algorithm, they analyze the terrain morphology of 5200 well-documented avalanche release areas around Davos and subsequently compute a spatial density estimation correlating with the PRA probability. To delineate the PRAs for their map product, the OBIA workflow of Bühler et al. (2018) is used.

2.5.1.2 PRA delineation after Veitinger et al. (2016)

The PRA delineation model, which forms part of the autoATES model developed by Larsen et al. (2020), is based on the open-source PRA algorithm created by Veitinger et al. (2016). This model uses on a fuzzy logic approach (Zadeh, 1965). The PRA algorithm employs three DEM derivatives as criteria: slope, terrain roughness, and a wind shelter index, as well as an optional binary forest mask, to exclude forested areas from the PRA. Sharp et al. (2018) expanded the PRA model by including the forest parameter into the fuzzy operator to account for the forest density. The model uses Cauchy membership functions (Jang et al., 1997), which are generalized bell functions that address the problem of sharp changes caused by simplified triangular functions (Veitinger et al., 2016). The Cauchy membership function is defined by three parameters (a,b,c) that determine the location and shape of the curve and, in turn, the membership values of the different input parameters. Various studies (Schumacher et al., 2022; Sharp, 2018; Sykes et al., 2022; Veitinger et al., 2016) have explored and tested different sets of parameters for the membership function. The Cauchy membership function is given as follows:

$$\mu(x)=\frac{1}{1+\left(\frac{x-c}{a}\right)^{2b}}$$

To quantify the potential for an area to release an avalanche, the input raster layers with membership values for slope, terrain roughness, and wind shelter are combined using the "fuzzy AND" operator. This operator was first introduced by Werners (1988) and is comprehensively described in the corresponding literature by Veitinger et al. (2016).

While tested initially for a 2 m grid cell size, recent studies have adapted the model for coarser DEM resolutions (e.g., 10 m) in recent studies (Larsen et al., 2020; Schumacher et al., 2022). The output of the PRA delineation is a raster file with values between 0 and 1, where lower values indicate lower probability and higher values suggest a higher susceptibility to avalanche release. To use the output as input for modeling avalanche mobility, a PRA threshold is applied to create a binary layer, where values below the threshold are classified as no PRA, and values equal to or greater than the threshold are classified as PRA. The application of the Cauchy membership function on the DEM derivatives: slope, ruggedness, wind shelter index, and the forest layer is visualized in Figure 3.

The algorithm identifies slope areas with inclinations ranging from 28° to 60° as PRAs. In the implementation by Veitinger et al. (2016), the highest degrees of membership are assigned to inclinations between 35° and 45°, as the first row in Figure 3 visualizes.

A wind shelter index combines terrain curvature and potential wind effects based on the assumption that wind drift is a major component of snow redistribution at a slope scale (Gauer, 2001). The wind shelter parameter is calculated after Plattner et al. (2004). According to the membership function, wind-protected terrain morphologies are attributed large membership values. In contrast, terrain features exposed to wind are attributed low membership values, indicated by the reddish areas in Figure 3. In addition to that, the PRA model is designed to account for primarily wind directions. However, regarding the autoATES model, Larsen et al. (2020) and Schumacher et al. (2022) neglect a primarily wind direction.

The roughness parameter combines the terrain roughness derived from the summer DEM with smoothing effects due to snow accumulation in winter. The method uses the vector ruggedness measure after Sappington et al. (2007). The fuzzy logic method assigns low membership values to rough morphologies and high membership values to flat and smooth terrain parts, which are more prone to avalanches, indicated by the reddish areas in Figure 3. However, Schumacher et al. (2022) and Larsen et al. (2020) do not include the roughness parameter in their models due to using a 10 m grid cell size. These authors argue that applying the roughness parameter to a 10 m DEM would result in accounting for the mountain morphology rather than individual slope characteristics.

The forest is included by accounting for basal area, stem density, or percentage of canopy cover depending on the data availability (Schumacher et al., 2022; Sharp, 2018; Sykes et al., 2022). Figure 3 demonstrates the assignment of the membership function to the PCC Forest Layer (percentage of canopy cover). It is visible that areas with no forestation are assigned with high membership values.

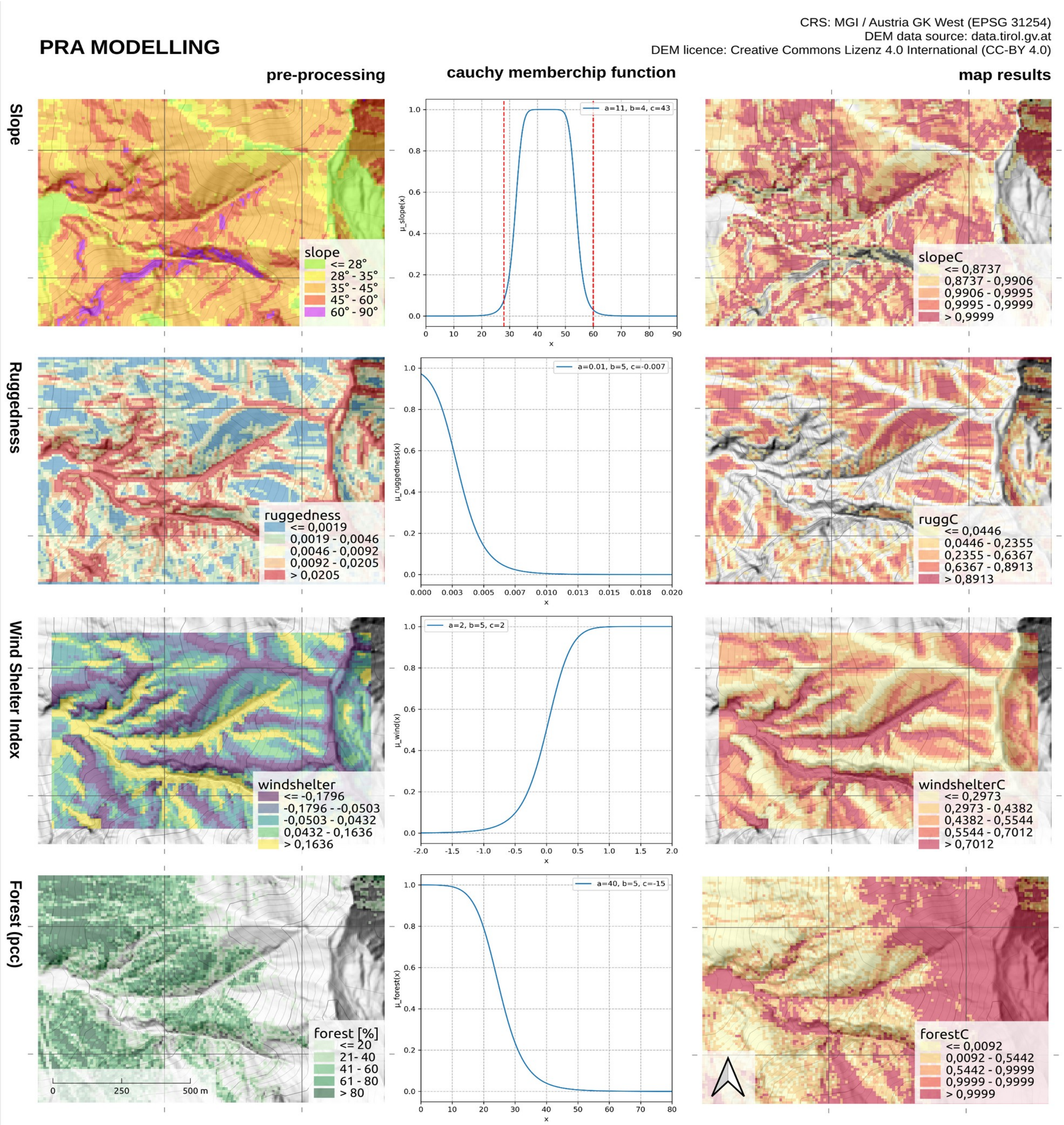

Figure 3: Visualization of the application of the Cauchy membership function on the 10m DEM derivatives: slope, ruggedness, wind shelter index, and the PCC Forest Layer. The depiction includes the input layers (first row), the Cauchy membership function with specified parameters a, b, and c (second row), and the output rasters (map results, third row) showing the effects of the applied Cauchy membership function. These are displayed in correlation with the corresponding inputs, such as slope with the 'C' suffix denoting the Cauchy transformation.

2.5.2 Avalanche mobility models

The movement of avalanches is a highly complex process that can only be approximated by simplified models. The available avalanche models differ in complexity, including the physical methods used and the level of detail of the calculation results. Computational models can be used to simulate avalanches, and parameter studies can be used to comprehend the sensitivity of the input parameter. Avalanche simulation models are the most objective tool to determine the characteristic features of avalanche movement for avalanche mitigation measures (Sauermoser et al., 2011).

According to Harbitz et al. (1998), avalanche calculation models can be divided into two approaches: physical-dynamic (process-based) and statistical-topographic (data-based) models. The former are physically motivated and usually require more input parameters than the latter models, which are empirically motivated and often less computationally intensive. However, Physical-dynamic models provide more detailed information about the process and its interaction with the terrain. The selection of the appropriate modeling method is determined by factors such as the intended objectives and accuracies, the input data, and the spatial scale of the simulations (D'Amboise, Neuhauser, et al., 2022).

A comprehensive review of used models in Europe is presented by Sauermoser et al. (2014).

2.5.2.1 Process-based physical models

Process-based models describe the physical processes involved in avalanche dynamics using mathematical equations that simulate avalanche movement from the release to the runout zone. These models can calculate dynamic quantities such as avalanche runout distance, pressure, and flow height (Maggioni, 2005). A widely used approach (Christen et al., 2010; Oesterle et al., 2022; Sampl & Zwinger, 2004) is the Voellmy-Salm model (Salm et al., 1990) with dry friction and a turbulent friction term, which is based on the early findings of Voellmy (1955) by determining the avalanche dynamics with the Voellmy fluid law, a combination of the Chezy friction term and Coulomb dry friction. The dry friction depends on snow properties and the pressure perpendicular to the slope. The turbulent friction refers to the roughness of the avalanche path (Sauermoser et al., 2014). Essential for a profound avalanche simulation is detailed knowledge about the initial conditions, such as release area, release height, and the two friction coefficients: μ and ξ (Maggioni, 2005).

The CAT / ATHM map products developed by Harvey et al. (2018) integrated the avalanche simulation tool RAMMS::EXTENDED, which is based on the work of Bartelt et al. (Bartelt et al., 2012, 2016) and Christen et al. (2010). These process-based avalanche propagation models require more detailed input parameters, including individual PRAs in a vector data format, release volumes, and friction parameter. To obtain these parameters, the approach described by Salm et al. (1990), as mentioned in Bühler et al.

(2018), is followed to determine the release height. The release volume is calculated by multiplying the release depth with the size of the PRAs resulting in an average release height of 50 cm. Additionally, the friction parameters are determined using the method proposed by Christen et al. (2010), with the classification of individual PRAs based on their size.

2.5.2.2 Data-based empirical models

Data-based empirical models are based on the quantitative assessment of avalanche runout distances (McClung & Schaerer, 2006). The runout distance of avalanches can be quantified as the angle of reach, the alpha angle, measured from the maximum point of the runout debris to the uppermost part in the release area, the starting point (Heim, 1932; Lied & Bakkehøi, 1980), as shown in Figure 4. The alpha angle is primarily determined by four parameters: the vertical drop height, the slope angle of the release area, the overall slope, and the longitudinal profile of the runout. To estimate the runout of avalanches, the alpha-beta model (Lied & Bakkehøi, 1980) was introduced. The model is based on a statistical analysis of avalanche runouts in Norway and correlates the alpha angle with the beta angle. The beta-angle is measured from the uppermost part of the release area to the 10° terrain point, which is associated with the point where the avalanche tends to decelerate. Lied et al. (1995) later also applied the method for the Austrian Alps.

Other data-based model approaches are, for instance, the runout ratio model, as presented in McClung & Schaerer (2006).

In addition, recent studies (D'Amboise, Neuhauser, et al., 2022) use a data-based approach to numerical estimate the runout dimensions by implementing the alpha angle as a stopping criterion for a two-dimensional avalanche simulation. The authors apply this approach to large-scale regional avalanche simulations without considering individual PRAs. In this study, the open-source Flow-Py model (D'Amboise, Neuhauser, et al., 2022) is incorporated into the automated avalanche terrain classification.

2.5.2.2.1 Flow-Py

Flow-Py is an open-source gravitational mass flow (GMF) simulation tool for avalanches, landslides, rockfall, and debris flows (D'Amboise, Neuhauser, et al., 2022). It is derived by a data-based, empirically motivated approach to model the magnitude, such as the dimensions of the runout, travel length, and intensity of the GMFs. In this study, it is applied to avalanches.

Flow-Py is programmed in Python3 (Rossum & Drake, 2010); the Flow-Py architecture follows an object-orientated approach, facilitating model adaptions. The model code is openly accessible (Neuhauser et al., 2021). The modeling process is done in three levels: (1) the cell level where the iterative routing is done, (2) the path level contains the spatial extent of the path from a corresponding release cell, and (3) the raster level which includes the quantities for all paths (D'Amboise, Neuhauser, et al., 2022).

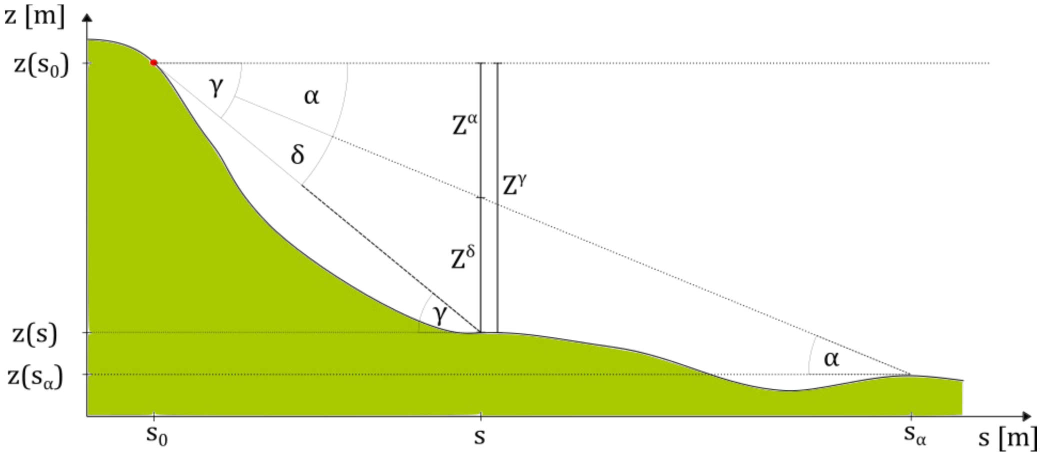

Figure 4: GMF path from release (s_0, $z(s_0)$) to runout area sα, z(sα)) characterized by the altitude z(s), projected travel length (s), and the local slope gradient. Derived geometrical quantities for the local runout point (s, z(s)) from the alpha angle concept are the total local geometrical vertical drop height (Z^γ), local travel angel (γ) and intensity measures Z^δ and Z^α

The data-based model uses geometric relationships derived from two fundamental principles: (1) routing and the (2) stopping. The routing framework (1) incorporates a model for three-dimensional flow path identification in a given terrain. The model is based on the path model for gravitational processes from Wichmann (2017). The model is designed to model mass movements in mountainous terrain, including flat or uphill terrain. The specific terrain, the flow direction, and process intensities determine the routing from the release area to the runout area.

Furthermore, the algorithm considers the concentration of the flow and the lateral dispersion. The stopping criteria (2) is defined by the runout angle concept, the alpha angle (Lied & Bakkehøi, 1980). In addition, the model incorporates stopping criteria for lateral spreading, which is determined by a cut-off threshold for the routing flux and the exponent. Following the assumption that a GMF must have specific fluid properties or a minimum routing flux to continue its propagation.

Determining the process intensity along the avalanche path and the subsequent runout is based on applying the alpha angle concept (Heim, 1932; Lied & Bakkehøi, 1980), allowing the derivation of the corresponding geometric parameters. In Figure 4, the alpha angle (ɑ) represents the total stopping criteria of the avalanche runout, therefore, from the line from the release area, s0, z(s0), to the runout, sɑ, z(sɑ). The local runout angle (γ), represented by a line from s0, z(s0) to the local runout point, s, z(s), can be used to derive quantitative properties to describe the process intensity. The local geometrical vertical drop height (Zγ) is derived by the difference of s, z(s0) and s, z(s). The geometrical drop height

($Z\gamma$) at the point s, z(s), is divided into two components: z delta ($Z\delta$) and z alpha ($Z\alpha$). Following the law of conservation of energy and Coulomb friction of a block movement (Heim, 1932), z alpha is associated with the dissipated energy (frictional dissipation) and z delta with the kinetic energy height. Consequently, z delta is associated with the energy associated with the process and allows the derivation of process intensity properties: velocity and impact pressure (D'Amboise, Neuhauser, et al., 2022). The deviation is shown in Section 4.2.

To perform a simulation, the model requires a digital elevation model and the location of the release areas as input data. In addition to the spatial input data, the algorithm is determined by four model parameters.

(1) alpha = stopping criterion for the avalanche runout. If alpha is set to 25°, the total angle from the runout to the release area measured along the projected path will be 25°.

(2) exponent = affects the lateral spreading. If the exponent is close to 1, the lateral spreading has a broad or even fluviatile characteristic, while approximating ∞ causes the flow divergence to become similar to a single-block characteristic.

(3) R stop = stopping criterion for the routing flux. The GMF initiates with R start = 1 and stops when R stop is reached.

(4) z delta limit = maximum limit for the local geometrical vertical drop height ($Z\gamma$), which is related to the maximum kinetic energy or the velocity of the GMF.

The output are numerous raster layers in the same resolution as the input layer, providing computed information about the avalanche mobility, the routing flux, which can be correlated with a theoretical mass (D'Amboise, Teich, et al., 2022), the cell count, which contains information about number of cells that propagate through a raster pixel, and the local geometrical vertical drop height ($Z\gamma$) which is associated with the kinetic energy height (D'Amboise, Neuhauser, et al., 2022).

2.5.3 Avalanche terrain classification models

In the context of the discussed approaches, avalanche terrain classification models represent the concluding phase of the model chain. Schmudlach & Köhler (2016) emphasize continuous ATES ratings based on geomorphological characteristics. On the other hand, Harvey et al. (2018) and Larsen et al. (2020) integrate an avalanche mobility model. Larsen et al. (2020) utilize discrete terrain classes for classification, while Harvey et al. (2018) developed two map products, the *Classified Avalanche Terrain* (CAT) and *Avalanche Terrain Hazard Maps* (ATHM), each with its unique classification scheme. In the CAT product, the PRAs are classified into four categories, represented by varying shades of reddish colors, which indicate the likelihood of avalanche release. The maximum runout of simulated avalanches, based on an average release height of 0.5 m, is depicted in yellow areas. Additionally, three shades of blue represent the potential for remote triggering.

On the other hand, the ATHM combines information about avalanche terrain (potential for avalanche release and remote triggering as well as runout) and the potential consequences of being caught in an avalanche. In the classification step, the raster values of these layers were normalized and merged to generate a continuous avalanche terrain hazard layer. The resulting map provides continuous values ranging from 0 (indicating low terrain hazard) to 1 (indicating high terrain hazard).

In the final step of the model chain proposed by Larsen et al. (2020), the ATES classifier is utilized to classify the terrain. The ATES classifier model merges information classified information on terrain slope, PRAs, and modeled potential runouts of avalanches to delineate the ATES classes. The parameters for the model are based on Campbell and Gould (2013).

The autoATES model (Larsen et al., 2020) has been enhanced through the contributions of various researchers (Schumacher et al., 2022; Sharp, 2018; Sykes et al., 2022). The model of Schumacher et al. (2022) considers the forest cover's density, which can range from open to dense, and considers its impact on the assessment of avalanche terrain. The algorithm is designed to consider parameters such as percent canopy cover, stem density, or basal area, depending on data availability. For instance, if the assigned ATES class from the previous step is initially classified as challenging, but a dense forest is detected in the area, the ATES classifier takes into consideration the mitigating effect of the forest and reduces the assigned class to simple (Schumacher et al., 2022).

In Section 4.3, Figure 23 visualizes the workflow of the autoATES classifier.

3 Study area and data

The study area is in Tyrol, Austria, and encompasses the mountainous terrain of the Stubaier Alps and parts of the Ötztaler Alps (Figure 5). The terrain is characterized by high alpine terrain, including rugged mountains, deep valleys, and glaciated areas. It stretches from the Kühtaisattel in the north to the main crest of the Alps in the south. The Ötztal valley defines the western boundary, while the eastern boundary is formed by the mountain ridge east of the Lüsenstal.

Regarding elevation, the study area ranges from 782 m a.s.l (meter above sea level) to its highest point at 3380 m a.s.l. The average elevation within the area is approximately 2258 m a.s.l.

The data used in this study is presented below. It is decided to work with a 10 by 10 m grid resolution to apply and test the model chain. However, finer digital elevation data is available. The 10 m resolution proved its computational efficiency within this study and is in line with previous studies (Larsen et al., 2020; Schumacher et al., 2022).

3.1 Digital elevation models

The digital elevation models (DEMs) splits into two products. The digital terrain models (DTMs) and the digital surface models (DSMs) both use geo-referenced positions and heights in a regular (height-) grid, also referred to as raster, of cells or pixels to describe the elevation of an area. The DTM specifically describes the terrain without vegetation or buildings, while the DSM includes all objects on the surface, including vegetation and buildings (BEV, 2023). Airborne laser scans from the summer terrain generate spatial data. For the application and testing of the model chain, the DTM with a 5 m resolution is obtained and resampled to 10 m, hereafter referred to as 10m DEM, for the derivation. In addition to that, the DTM and the DSM are also obtained in a 1 m resolution. The difference between the DTM and the DSM is used to obtain the spatial forest information, as described in Section 4.1.2. Hereafter, both data layers are referred to as 1m DTM and 1m DSM.

The data for the study area is obtained from the public web coverage service (WCS) from the Open Government Data of the Province of Tyrol and is licensed under a Creative Commons Attribution 4.0 International Public License. The coordinate reference system (CRS) is the MGI / Austria GK West – EPSG code: 31254.

The underlying digital elevation data for the PRA validation process is sourced from the swissAlti3D DTM, which is accessed from the public server of the Federal Office of Topography, swisstopo. The CRS used is LV95 – EPSG code: 2056. The raster data has a resolution of 2 by 2 m. For further processing, the DTM is resampled to 10 m resolution.

3.2 Reference data

To comprehensively evaluate the model chain components, diverse reference datasets are employed. Observed release areas contribute to assessing the PRA model, while a dataset of 19 documented avalanche outlines aids in the qualitative and quantitative analysis of the avalanche mobility model. To enhance the interpretation of the avalanche mobility model findings in relation to the ATES classification, a Swiss avalanche data analysis derived from satellite imagery is used, covering over 18,000 avalanches. Furthermore, the ATES terrain classification evaluation is supported by mapped avalanches in the study area, also obtained from satellite imagery, and documented ski routes categorized by difficulty.

3.2.1 Observed avalanche release areas

For the PRA validation process, a data set of observed release areas (ORAs) of the Swiss Federal Institute for Snow and Avalanche Research (SLF) is used, hereafter referred to as CH ORA Dataset. The data set covers the Davos region, considered one of the best reference data sets available (Bühler & von Rickenbach, 2018) with 5785 manually mapped release areas in the field from 1970 to 2016. Part of it is publicly available and covers the Rinerhorn, Jakobshorn, and Parsenn regions. The data set has 2129 individual PRAs in a vector data format. The test regions are limited to areas well observed from the ski resorts, and observations of natural and artificially triggered avalanche events are included in the database (Bühler et al., 2018).

3.2.2 Manually mapped avalanches within the study area

To compare the Flow-Py results within the study area, a data set of the affected areas (vector data) of 19 avalanches is used, hereafter referred to as AUT AWS Avalanche Reference Dataset. The avalanche size of the observed avalanches corresponds to the EAWS size class 3, determined by expert assessment. The mapping process is done with geographic data analysis and photo documentation.

The mapping is conducted and provided by avalanche experts from the Tyrol Avalanche Warning Service.

3.2.3 Large-scale avalanche data from satellite imagery

To enhance the interpretation of the avalanche mobility model findings in relation to the ATES classification, a large-scale Swiss avalanche data analysis derived from SPOT6 satellite imagery is used (Toft et al., 2023). The data analysis is based on over 18,000 mapped avalanches from an avalanche cycle in Switzerland (Bühler et al., 2019), hereafter referred to as CH SPOT6 Avalanche Reference Dataset. These avalanches span approximately 936 km^2 and are classified into size categories ranging from 1 to 5 based on the affected area (Table 3). Toft et al. (2023) analyzed this dataset, including assessments of quantities like travel length and the alpha angle.

To assess the ATES terrain classification, an additional avalanche dataset is utilized. This dataset is also generated based on SPOT6 satellite imagery and includes mapped avalanche runout areas. In addition to that, the dataset includes an avalanche size estimation based on the EAWS travel length. The mapping and the size estimation are conducted and provided by avalanche experts from the Tyrol Avalanche Warning Service. The SPOT6 data within the study area was acquired shortly after an avalanche cycle in February 2023. Hereafter, the dataset is referred to as AUT SPOT6 Avalanche Reference.

It is important to note that due to the recent completion of this mapping campaign, the dataset still needs to be published and could not be included in earlier assessments for the PRA and avalanche mobility models. However, this data opens up possibilities for enhancing the parameterization of the individual model chain components.

3.3 Additionally data

A reference dataset of mapped glaciers is integrated to incorporate glaciated areas into the ATES terrain classification (Buckel & Otto, 2018). The vector dataset is transformed into a binary raster file with a 10 by 10 meters resolution, hereafter referred to as the Glacier Layer. This dataset was generated through a mapping campaign primarily utilizing Google Earth satellite imagery from 2015. However, the dataset is not the most recent. It represents the latest data accessible. According to the Glacial layer, about 5% (34.3 km^2) of the total land area in the study area is covered by glaciers.

Figure 5: Study area; Stubaier Alpen and parts of the Ötztaler Alpen (approx. 700 km²), forestation is shown as percentage per canopy cover (derived in Section 4.1.2)

4 Application and testing of the model chain

The main objective of this thesis is to apply and test the model chain of the autoATES terrain classification (Larsen et al., 2020; Schumacher et al., 2022). The model chain encompasses three sequential steps, each progressively building upon the preceding one. Each model step is subjected to individual testing and discussion in alignment with its sub-objectives, thereby structuring this chapter. The model steps and their corresponding objectives include:

(1) **PRA delineation**

- Parameterization of the PRA model (Sharp, 2018; Sykes et al., 2022; Veitinger et al., 2016) to realistic delineate potential release areas (PRAs) within the study area (Section 4.1)

(2) **Avalanche mobility model**

- Assessment of the data-based avalanche mobility model (D'Amboise, Neuhauser, et al., 2022) for regional runout modeling size three avalanches for the ATES terrain classification (Section 4.2)

(3) **ATES classification**

- Application and adaptation of the ATES classifier (Larsen et al., 2020; Schumacher et al., 2022) for size three avalanches in the study area (Section 4.3)

4.1 PRA model

To establish a suitable parameterization for the PRA model (Sharp, 2018; Sykes et al., 2022; Veitinger et al., 2016) and, subsequently, the model chain, the following methodology is employed:

The initial phase involves evaluating the PRA model's performance in realistically delineating PRAs through a comparison with observed release areas using the CH ORA Dataset (Section 3.2.1) since there is no PRA validation set in our study area. This step involves comparing three different configurations of the PRA model, focusing on implementing the roughness parameter, detailed in Table 10. Statistical skill scores are derived from an error matrix and subsequently discussed to quantify the comparison and plausibility. Additionally, the study assesses the influence of the forest parameter (Sharp, 2018) by applying the PRA model to the study area, as the CH ORA Dataset lacks forested regions. While the impacts of forest effects are described qualitatively, a comprehensive analysis is not conducted, given that they are not the central focus of this thesis. In addition, by applying it to the study area, the determination of the PRA model parameterization for the model chain is enhanced by a qualitative assessment of the PRA roughness parameter.

4.1.1 Comparison of PRA model performance with observed release areas

An established approach for evaluating the precision of thematic maps in remote sensing, detailed by Congalton & Green (1999), involves calculating an error matrix and deriving statistical skill scores from it. This method has been previously employed to compare the performance of various PRA models (Bühler, von Rickenbach, Stoffel, et al., 2018). In this study, the Heidke skill score (kappa, or HSS) and the true skill statistic score (TSS) are adopted to assess the plausibility of different parameterizations of the PRA models and, consequently, the resulting outcomes. The prepossessing for the error matrix involves converting the reference vector data of the CH ORA Dataset into a binary raster map. In this map, 1 indicates the presence of observed release areas (ORA), while 0 indicates their absence (no ORA). Additionally, areas outside the validation domain are assigned a value of -1. Similarly, the continuous output raster map of the PRA model is converted into binary raster layers according to the applied PRA threshold. In this process, raster cells with a value equal to or above the PRA threshold are assigned as PRA (1), while those below the threshold are designated as no PRA (0). The PRA threshold is incrementally increased for each of the three PRA model setups from 0 to 1 in steps of 0.01, generating 100 binary PRA raster layers per PRA model setup. Subsequently, the error matrix is computed to compare each PRA file with the observed release areas. The error matrix only considers values within the validation domain, neglecting raster values with -1.

The error matrix distinguishes between:

- **True Positive (TP)**: The PRA model correctly identifies an ORA as a PRA.
- **False Positive (FP)**: The PRA model incorrectly identifies a no ORA area as a PRA.
- **True Negative (TN)**: The PRA model correctly identifies a no ORA as a PRA.
- **False Negative (FN)**: The PRA model incorrectly identifies an ORA as a no PRA.

Using the error matrices, specific quantities (Allouche et al., 2006) can be calculated to assess the precision of different model configurations and analyze the corresponding PRA thresholds. The quantities are:

(1) **Sensitivity (SE)**, in the context of the PRA model, represents the proportion of ORAs correctly identified as PRAs. It quantifies the model's ability to avoid omitting true release areas (omission errors).

$$SE = \frac{TP}{TP + FN}$$

(2) **Specificity (SP)**, in the context of the PRA model, represents the proportion of non-observed release areas correctly identified as no PRAs. It quantifies the model's ability to avoid falsely identifying areas as PRAs (commission errors).

$$SP = \frac{TN}{FP + TN}$$

Regarding the goals of this subsection, it is essential for the PRA model setup and the corresponding PRA threshold to exhibit a high probability of ORA detection (sensitivity) while simultaneously maintaining a low proportion of false positives, which equals 1 – specificity. The assessment of the overall model performance involves calculating a Receiver Operating Characteristic (ROC) curve (Fielding & Bell, 1997). However, due to the specific interest threshold, the focus shifts to evaluating only the HSS and the TSS.

(3) **Overall accuracy (OA)**, is a measurement to quantify the proportion of how well the PRA model performs in correctly identifying ORA and noORA.

$$OA = \frac{TP + TN}{TP + FP + TN + FN}$$

(4) **Heidke skill score (HSS)** or kappa is a statistical skill score that adjusts the overall accuracy by considering all four categories of the confusion matrix and incorporates the accuracy that would be achieved by chance. Kappa ranges from -1 to 1, with 1 indicating perfect agreement and 0 indicating agreement no better than expected by chance, and -1 worst than by chance.

$$HSS = \frac{OA - CA}{1 - CA} \quad \text{with:} \quad CA = \frac{(TP + FP) * (FP + FN) + (FN + TN) * (FP + TN)}{(TP + FP + TN + FN)^2}$$

(5) **True skill statistic score (TSS)** incorporates all four categories and ranges from -1 to 1, like kappa. The main advantage of the TSS is that the prevalence, or the varying proportions of the distinct classes of model and reference data, such as PRA or ORA and noPRA or noORA, do not bias it. Therefore, the Peirce skill score is a composite measure of the true positive and false positive rates. It is a valuable tool for validating and evaluating models used in natural hazard assessment and risk management, as stated by .

$$TSS = SE + SP - 1$$

In this study, three different model setups are investigated, each differing in the implementation of the roughness parameter. Table 8 provides a comprehensive summary of the different model setups, outlining the incorporation of the roughness parameter, cut-off values, and membership values (a,b,c), along with their respective references.

The integration of the roughness parameter is achieved through three distinct approaches: (1) as a binary mask layer, akin to the methodology utilized by Bühler et al. (2013), involving the subtraction of raster pixels exceeding a threshold of 0.02 during PRA delineation; (2) inclusion within the fuzzification step of the PRA model, following the original methodology introduced by Veitinger et al. (2016); and (3) without any roughness implementation, aligning with the approaches adopted by Larsen et al. (2020) and Schumacher et al. (2022).

In this study, the wind shelter parameter is not further examined and is implemented as suggested by Veitinger et al. (2016). The originally implemented parameter for the wind direction (Veitinger et al., 2016) is disregarded by setting the wind direction to 0° with a tolerance of 180°. This approach aligns with recent developments (Larsen et al., 2020; Schumacher et al., 2022). The combination of the membership values (a,b,c) aligns with recent developments from other working groups. Figure 6 provides a visualization of distinct model setups (rows) alongside three exemplary PRA thresholds: 0.01, 0.50, and 0.80 (columns), furthermore, a subset of the CH ORA Dataset.

Table 8: The PRA model setups vary based on the implementation of roughness, categorized as: binary roughness mask (labeled as 1 binary-rugg), fuzzy roughness (labeled as 2 fuzzy-rugg), and no roughness (labeled as 3 no-rugg). The membership values (a, b, c) of the parameter, the slope cutoff, and the corresponding literature for these membership values are also provided.

Model code	Parameter	Implementation	Membership value	Cutoff	Literature
1 binary-rugg	Slope	Fuzzy	a=11, b=4, c=43	< 28° & >60°	Veitinger et al. 2016
	Roughness	Binary	-	< 0.02	
	Wind shelter Index	Fuzzy	a=2, b=5, c=2	-	Veitinger et al. 2016
2 fuzzy-rugg	Slope	Fuzzy	a=11, b=4, c=43	< 28° & >60°	Veitinger et al. 2016
	Roughness	Fuzzy	a=0.01, b=5, c=-0.007	-	Sharp et al. 2018
	Wind shelter Index	Fuzzy	a=2, b=5, c=2	-	Veitinger et al. 2016
3 no-rugg	Slope	Fuzzy	a=11, b=4, c=43	< 28°& >60°	Veitinger et al. 2016
	Wind shelter Index	Fuzzy	a=2, b=5, c=2	-	Veitinger et al. 2016

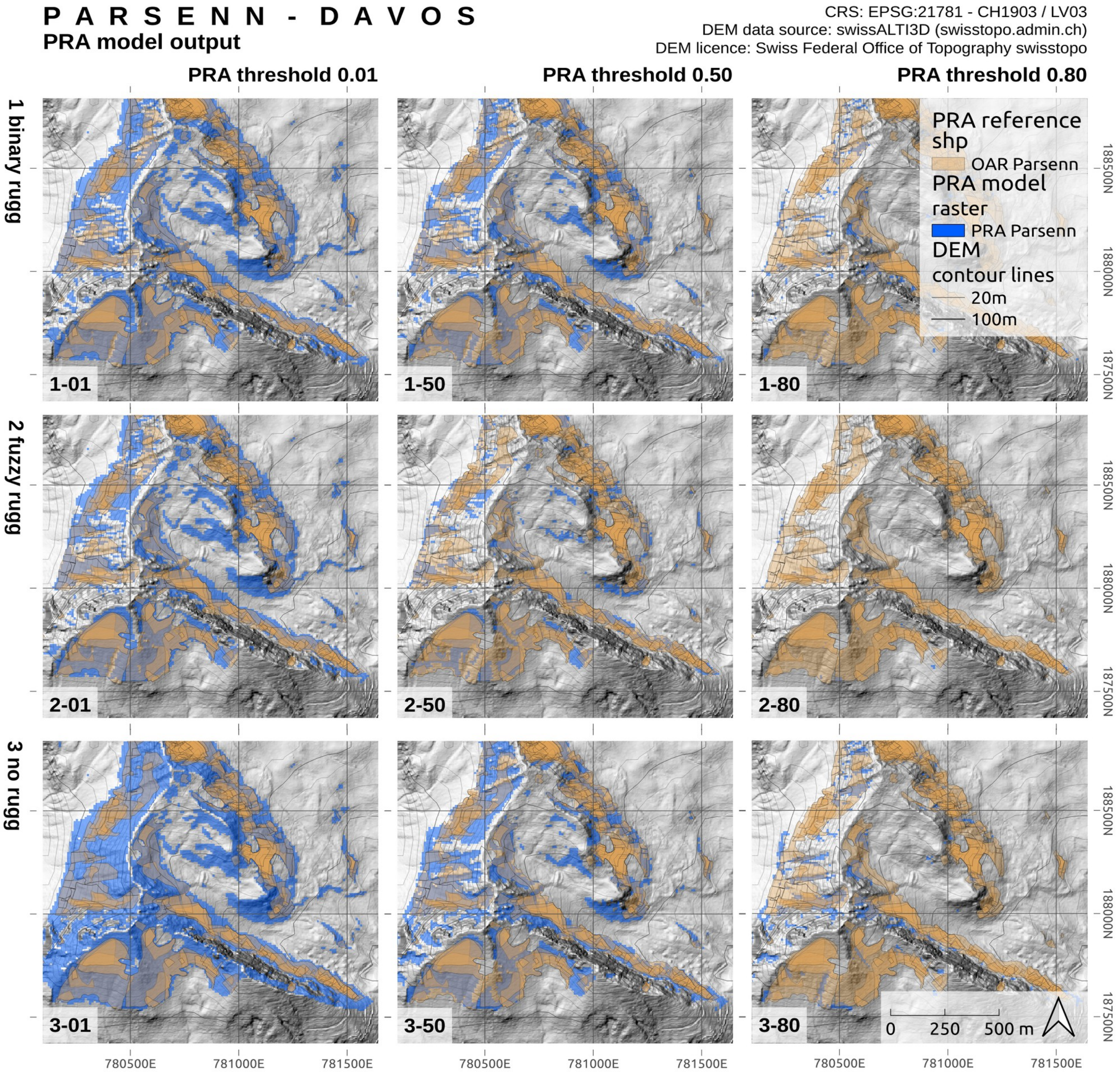

Figure 6: Comparison of the binary-rugg, fuzzy-rugg, and no-rugg PRA model output (blue), displayed in the rows of the figure, with a corresponding PRA thresholds of 0.01, 0.50, and 0.80 displayed in the columns of the figure. The ORA Reference Dataset is indicated with a transparent orange overlay.

The examination of the Heidke skill score (HSS) and the true skill score (TSS) is depicted in Figure 7. The figure reveals the relationship between the PRA threshold (x-axis) and the associated HSS (upper plot) and TSS (lower plot) score on the y-axis for the three distinct model setups. Examining the HSS plot, it is evident that all three models exhibit a similar trend. Initially, there is a sharp increase in the HSS score from PRA threshold 0 to 0.01, caused by delineating 0 ORA at a threshold of 0, whereas, at a threshold 0.01, the maximum of true positives is reached. However, at the same time, the maximum of false positives occurs. Following this initial rise, the HSS scores for all models stabilize and remain relatively constant up to a threshold of 0.1. The binary-rugg and fuzzy-rugg models display similar values, with the no-rugg model starting slightly lower. Beyond a threshold of approximately 0.1, all models achieve higher HSS scores due to the minimization of the false positives. While the binary-rugg model consistently performs the best (up to a threshold of around 0.7), the no-rugg model gradually approaches the performance of the binary-rugg model.

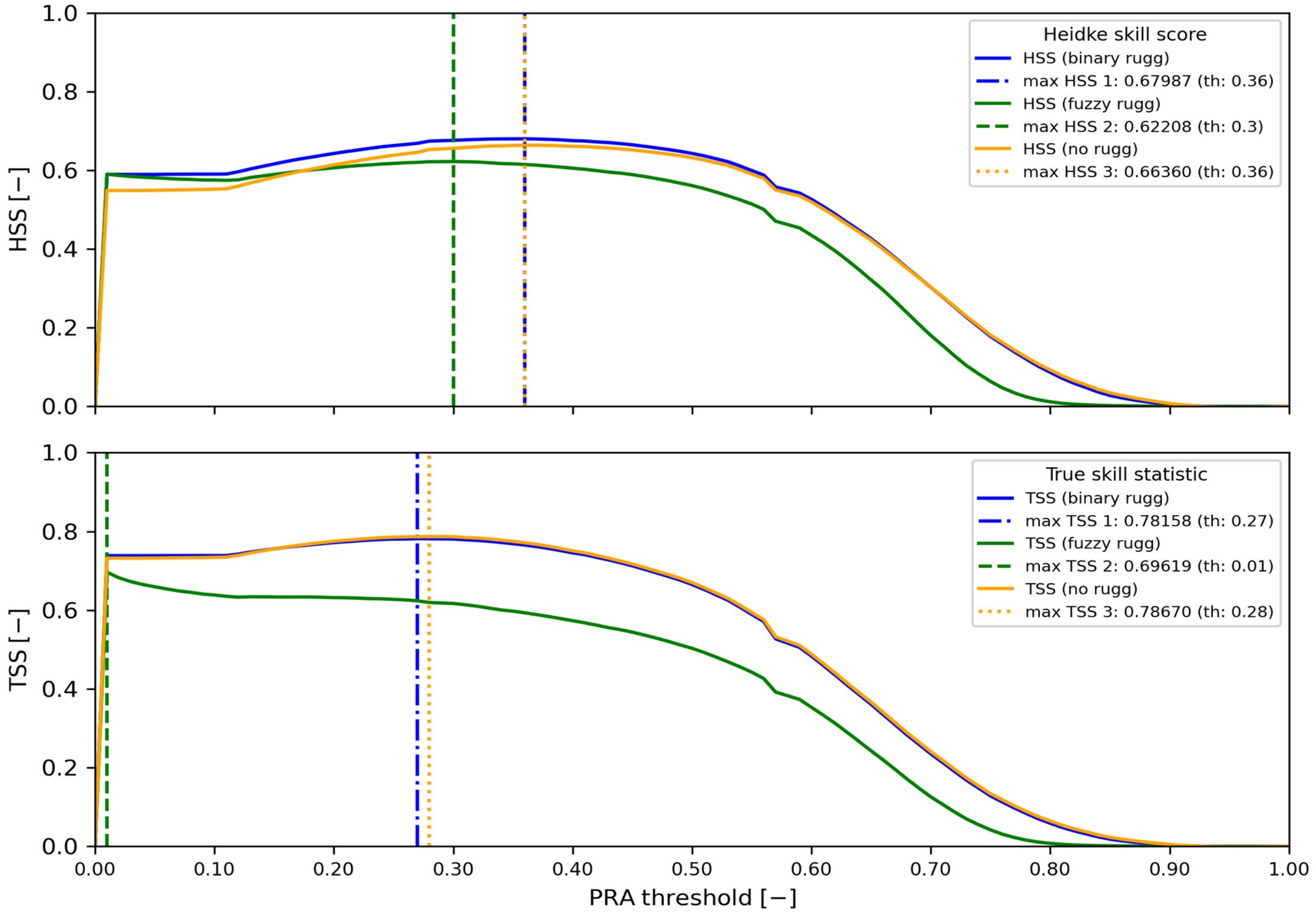

Figure 7: HSS and TSS Plots of the binary-rugg, fuzzy-rugg, and no-rugg PRA model, calculated from the error matrix derived from comparing the model's output and the CH ORA Reference Dataset with a PRA threshold range from 0 to 1.

Conversely, the fuzzy-rugg model exhibits a continuous decline in performance from a threshold of approximately 0.17. The peaks of the binary-rugg (0.67897) and no-rugg (0.66360) models occur at a threshold of 0.36 and exhibit a minimal deviation of 0.01627. The maximum of the fuzzy-rugg (0.62208) model is reached at a threshold of 0.30. Notably, the curves between thresholds 0.2 and 0.5 appear relatively flat, indicating a relatively stable performance range for the models within this threshold range. When examining the TSS plot, a clear pattern is evident: both the binary-rugg and no-rugg models exhibit a consistent trend. While the curve of the fuzzy-rugg model reflects this pattern, it does not exceed the initial value of 0.69619 after the detection of PRAs with a threshold of 0.01 when the threshold value increases. The other two models, binary-rugg and no-rugg, show a similar trend as observed in the HSS plot. Starting from a threshold of approximately 0.1, the TSS values of the binary-rugg and no-rugg models begin to rise again, reaching their maximum at thresholds of 0.27 with a value of 0.78158 for the binary-rugg model and 0.28 with a value of 0. 78670 for the no-rugg model. Both models show a relatively consistent TSS from a threshold of 0.2 to 0.4. However, it is not as dominant as depicted in the HSS plot. Beyond a threshold of 0.4, the no-rugg and binary-rugg models exhibit a decline.

In summary, evaluating the HSS and TSS scores of the binary-rugg and no-rugg models show similar performance in identifying ORAs as PRAs. However, the performance of the fuzzy-rugg model is considered insufficient for further investigation and, therefore, not used for the model chain.

4.1.2 Adaptation of the PRA model to the study area

The PRA model is applied to the study area in the following section to discuss a qualitative assessment of the binary-rugg and no-rugg PRA model setups. This includes the integration of a forest layer and a comparison between the binary-rugg and the no-rugg model. This section defines the PRA model setup with a corresponding PRA threshold for the subsequent model chain steps.

As discussed in Section 2.1, the presence or absence of forest is a crucial factor in mitigating avalanche releases. Therefore, it is reasonable to incorporate the forestation parameter in the PRA model. Since forested regions are not covered in the CH ORA Reference Dataset, the influence of integrating the forest parameter is qualitatively assessed within the study area. This is conducted using the no-rugg model, employing a corresponding threshold 0.25 (see Table 9). The parameterization of the fuzzy membership function of the forest layer is based on the work of Sykes et al. (2022).

Table 9: The PRA model setups vary based on the neglection (3-1 noForest) or the implementation of the forest parameter (3-1 Forest), accompanied by the model with no roughness (labeled as 3 no-rugg). The membership values (a, b, c) of the parameter, the slope cutoff, and the corresponding literature for these membership values are also provided.

Model code	Parameter	Implementation	Membership value	Cutoff	Literature
3-1 noForest	Slope	Fuzzy	a=11, b=4, c=43	< 28° & >60°	Veitinger et al. 2016
	Wind shelter Index	Fuzzy	a=2, b=5, c=2	-	Veitinger et al. 2016
3-1 Forest	Slope	Fuzzy	a=11, b=4, c=43	< 28°& >60°	Veitinger et al. 2016
	Wind shelter Index	Fuzzy	a=2, b=5, c=2	-	Veitinger et al. 2016
	Forestation (PCC)	Fuzzy	a=40, b=3.5, c=-15	-	Sykes et al. 2022

To integrate forest information into the PRA model, prior research has employed (Schumacher et al., 2022; Sharp, 2018; Sykes et al., 2022) various parameters such as stem density, basal area, or percentage of canopy cover (PCC). Given the data availability (Section 3) for the study area, the percentage of canopy cover is used, hereafter referred to as PCC Forest Layer. The PCC Forest Layer is derived from the difference between the 1m DEM and the 1m DTM (Section 3.1). The difference between the DEM and DTM is interpreted as the height of the vegetation or forest. This might result in potential misinterpretations concerning the presence of buildings and settlements. However, it is essential to note that the ATES classification applies to areas above 1,500 m.a.s.l., and buildings are primarily situated at lower elevations within the study area. Following the approach of Schumacher et al. (2022), the difference layer is converted into a binary layer by employing a threshold of 5 m for the difference. To calculate the PCC Forest Layer for a 10 m raster cell, the SAGA aggregate function (Olaya, 2005) is used. This function calculates the sum of the binary layer values (> 5 m difference) within a 10 m raster cell and assigns the sum as a new value to the aggregation layer. The resulting layer contains values from 0 to 100 representing the PCC Forest Layer, as shown as a sub-layer in Figure 5.

The findings of the visual validation demonstrate that the integration of forest information in the PRA model substantially affects the reduction of PRAs, as shown in Figure 8. The incorporation of the PCC Forest Layer in the PRA algorithm leads to a significant decrease in the overall PRA area by 10.3% throughout the study area. Furthermore, the reduction is even more significant below the treeline at 1800 m a.s.l., with a reduction of 36.1% (Table 10).

As discussed in Section 2.1, forested areas have a mitigating effect on the susceptibility of avalanche release. Incorporating a forest layer in the PRA model effectively captures this phenomenon, as evidenced by a visual comparison of the results (Figure 8). Although the study area in the high alpine region contains only 23% forested areas, the overall reduction in PRA is by 10.3% (Table 10). Furthermore, the reduction of PRA by approximately one-third below the 1800 m a.s.l. threshold is substantial and appears reasonable in a visual comparison. However, a rigorous validation using observed release areas in forested regions and more detailed spatial information on forests would further support these findings. However, this is not the focus of this study. In addition to that, it is essential to note that the forest structure changes over time. This aspect must be considered when incorporating forest information, such as PCC Forest Layer, into the model chain. However, incorporating this information enhances the PRA model since the mitigating effect of forestation is being considered. This enhancement is integrated into the model chain, aligning with the methodology proposed by Schumacher et al. (2022), Sykes et al. (2022).

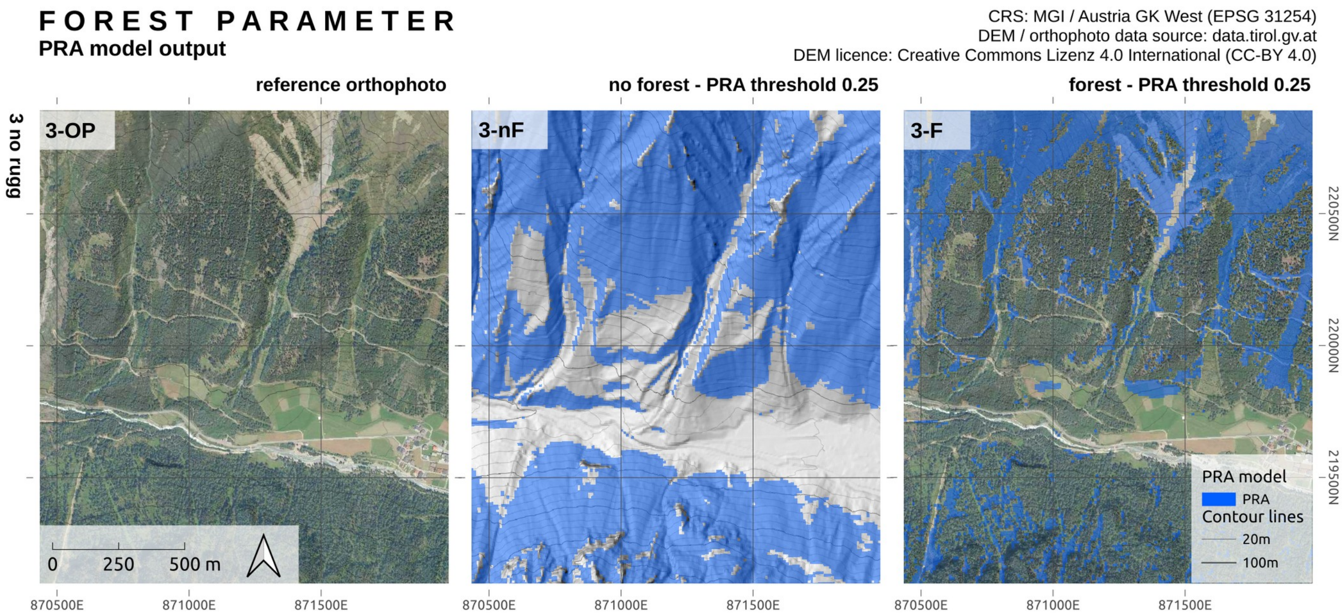

Figure 8: Effect of the forestation (PCC Forest Layer) on the PRA delineation applied to the study area. Figure 3-OP depicts the forestation on the orthophoto, Figure 3-nF displays the PRA result of the model without the forest parameter (3-1 noForest), and Figure 3-F shows both the orthophoto and the result of the PRA model with the forest parameter (3-1 Forest).

Table 10: Percentage of the area covered by PRA with and without the PCC Forest Layer compared to the total study area and the area below the treeline (1800 m a.s.l.).

	Reference area	PRA noForest		PRA Forest	
	Study area [km^2]	area [km^2]	% of area	area [km^2]	% of area
total height range	730.84	373.87	51.16	298.60	40.86
below treeline	148.68	70.77	47.59	17.09	11.50

Furthermore, including the ruggedness parameter in the PRA model is also under consideration. Subsequently, the qualitative impact of the binary ruggedness parameter is discussed. Figure 11 illustrates the PRA results obtained from the no-rugg model (left) and the binary-rugg model (right), each at a threshold of 0.3. The map in the middle displays the binary ruggedness mask, which is applied in the binary-rugg model.

It is evident that the no-rugg model delineates PRAs extensively across the slope without considering the presence of ridges or very rough morphologies. In contrast, the binary ruggedness mask effectively detects areas such as ridges and rough morphologies and subtracts them in the binary-rugg model. The exclusion of these morphological features within the PRA model is reasonable, as they are known to be less susceptible to avalanche release, as stated in Schweizer et al. (2003) or Section 2.1.

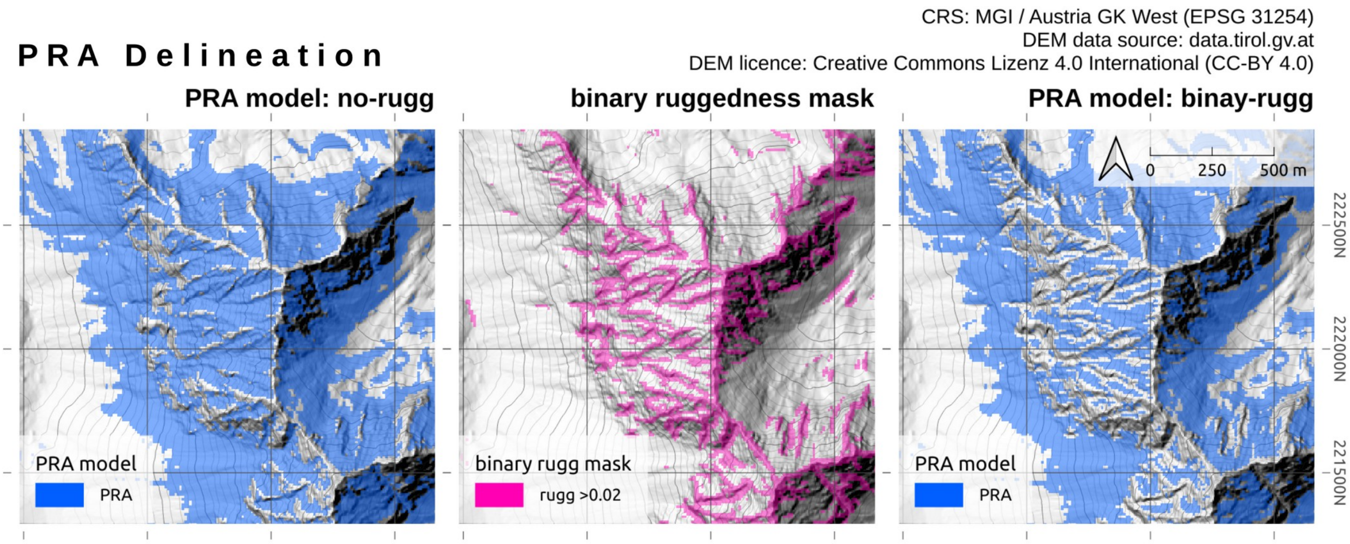

Figure 9: Comparison of the no-rugg and the binary-rugg PRA model, with the corresponding binary ruggedness mask.

4.1.3 PRA model parameterization for the model chain

The quantitative assessment of the three examined PRA models against the CH ORA Dataset reveals that both the binary-rugg and no-rugg models outperform the fuzzy-rugg model (Section 4.1.1). Prior research implemented the roughness parameter using a 2 m grid resolution (Veitinger et al., 2016); however, the application on a 10 m DEM accounts for the mountain morphology rather than individual slope characteristics (Larsen et al., 2020; Schumacher et al., 2022). This statement provide an explanation for the lower performance observed in the case of the fuzzy-rugg model.

The application of the binay-rugg and the no-rugg model to the study area is presented in Section 4.1.2. A qualitative assessment suggests that including the PCC Forest Layer is reasonable. However, the derivation of this layer from the 1m DTM and 1m DSM is based on the assumption that differences greater than 5 m between the two layers indicate the presence of forests. However, this approach may need to accurately reflect current conditions, as it captures only a specific moment of exploration data. Since forests undergo dynamic changes over time, this method may only partially capture their variability. Additionally, it is worth mentioning that this derivation needs to account for distinctions between deciduous and evergreen trees. A comprehensive examination beyond this thesis's scope can refine this incorporation further.

The binary-rugg and no-rugg models perform comparably in identifying the CH ORA Dataset. However, when qualitatively comparing within the study area, it becomes apparent that including a binary ruggedness mask results in excluding very rugged and convex terrain features, such as ridges. As discussed in Section 2.1, these specific terrain features have a lower susceptibility to avalanche release, reflected in their low occurrence covered in the CH ORA Dataset. Therefore, excluding these features from the PRA description is considered reasonable. Furthermore, more precise delineation of PRAs is a critical step in dividing PRAs into more detailed individual PRAs, as sharp terrain changes such as ridges serve as natural boundaries between PRAs.

Given these findings, the PRA model selected for subsequent steps in the model chain is the binary-rugg model, incorporating the PCC Forest Layer. The model yields optimal HSS and TSS results at thresholds of 0.27 and 0.36 (Figure 7). As the trend is relatively low in the range of 0.20 to 0.50 in the HSS analysis and between 20 and 40 in the TSS analysis, it is decided to work with a threshold value of 30 for the binary-rugg model. Table 11 summarizes the delineated PRA area in the context of the study area.

Table 11: Summary of the resulting area and percentage covered by PRAs within the study area. The applied model is the binary-rugg model, with forest parameter at a corresponding PRA threshold of 0.3.

Study area [km^2]	730.84
PRA area [km^2]	243.44
% of area	33.32

4.2 Avalanche mobility model

In the subsequent step of the autoATES model chain (Larsen et al., 2020; Schumacher et al., 2022), the avalanche mobility model Flow-Py developed by D'Amboise, Neuhauser, et al. (2022), is investigated. The simulation results are incorporated into the ATES classification step with two alpha angles, accounting for less and more frequent avalanches (Schumacher et al., 2022). The area between the runout determined by the two alpha angles is considered challenging terrain. In contrast, terrain below this range is classified as simple terrain, and terrain above the range is classified as complex.

The objective of the avalanche mobility model of this thesis is to connect the two alpha angles to the range of size characteristics typically associated with size 3 avalanches. The alpha angle threshold corresponding to the lower range of size three avalanches will establish the Flow-Py parameterization for the model chain. The findings of the alpha angle for the upper range of size three avalanches will also contribute to the parameterization for the ATES classification step. In order to achieve this, three comparative optimization analyses (OA) are established and discussed:

OA 1 involves an investigation of various Flow-Py parameters using the AUT AWS Avalanche Reference Dataset (Section 3.2.2), as a reference, which consists of 19 mapped avalanche outlines in the study area. Through a qualitative analysis of the effects of these parameters, the main objective of this OA is to identify a suitable exponent parameter for the ongoing investigations.

OA 2 aims to assess the feasibility of utilizing a single alpha angle for back-calculating the travel lengths of the 19 avalanches in the AUT AWS Avalanche Reference Dataset. Plausibility is evaluated by computing the root mean square error (RMSE) for each set of avalanche simulations corresponding to different alpha angles.

OA 3 quantitatively compares 100 randomly selected avalanche simulations across the study area using discrete avalanche size classification ranges for travel length, impact pressure, and affected area.

The simulation procedure for each OA involves systematically altering the alpha angle, ranging from 20° to 40°, with an increment of 2°. Additionally, varying exponents, which affect the lateral spreading (Section 2.5.2.2.1), are applied for the OA 1. The setup of input parameters is described in Table 12. The used DEM and the PRA layer have a raster resolution of 10 m.

Table 12: Input parameters for the Flow-Py simulations, varying in alpha angle and exponent, R stop, and z delta limit, are default values (D'Amboise, Neuhauser, et al., 2022)

Parameter	**OA 1**	**OA 2**	**OA 3**
alpha angle	26 – 36 (in steps of 2)	20 – 40 (in steps of 2)	20 – 40 (in steps of 2)
exponent	2, 4, 6, 8, 10, 15, 20, 30, 45	8	8
R stop	0.0003 (default)	0.0003 (default)	0.0003 (default)
z delta limit	270 (default)	270 (default)	270 (default)

To facilitate this multiple simulation procedure, an automated batched Flow-Py simulation code is used to explore different parameter combinations across multiple avalanches.

The Flow-Py output raster files are consolidated into a single comma-separated values (CSV) file per simulation, where each column represents the raster values of a specific output file. Although this consolidation results in losing geographic position information (longitude-, latitude-values), it enables an easily generalizable analysis workflow. The affected area in square meters is calculated by multiplying the number of entities in the cell count column of the CSV file by 100, accounting for a raster resolution of 10 by 10 m.

The impact pressure is obtained in accordance with Rudolf-Miklau & Sauermoser (2011) as the following:

$$\textit{impact pressure}[Pa]=\rho v^2$$

The flow density is assumed to be ~200 kg m^{-3}, which aligns with McClung & Schaerer (2006). Based on the energy-line method (Körner, 1980), the velocity can be estimated directly from the flow intensity result of Flow-Py (z delta), which represents the kinetic energy height, as the following:

$$\textit{velocity}\,[m\,s^{-1}]=\sqrt{z\,delta\,2\,g}$$

Runout length requires no additional calculations and can be derived directly from the simulations. Nevertheless, changes were made to the Flow-Py code to capture the maximum travel length achieved in the avalanche mobility simulation. The resulting file of calculated runout lengths contains values representing the projected horizontal travel distance along the avalanche path. For the OA, the 99th percentile is used. In the following section, all three OA are evaluated separately.

4.2.1 Qualitative comparison of the mobility model with mapped avalanches (OA 1)

The qualitative investigation of the Flow-Py simulation results encompasses the Flow-Py parameter alpha angle and exponent. The resulting PRA layer from Section 4.1.3 for the Flow-Py simulations is used as input. The PRA layer is cropped to the extent of the mapped avalanche outlines. It is important to note, that all calculated PRAs in the mapped avalanche extent are considered, which may deviate from the actual circumstances. In order to discuss the varying parameters, as stated in Table 12, three avalanches (ID 12 in Figure 11, ID 14 in Figure 10, and ID 5 in Figure 12) are used as an example.

Figures 11, 10, and 12 illustrate the effects of different alpha angles and exponent values. As examples for the alpha parameter and exponent values for avalanche ID 12 (Figure 11), the angles of 26°, 30°, and 34° are chosen, and exponent values of 2, 8, and 30. For avalanche ID 14 (Figure 10) and ID 5 (Figure 12), the angles of 26° and 28° are chosen and exponent values of 2, 8, and 30. In the figures, the blue pixels represent the delineated PRAs within the documented avalanche areas. The simulated travel lengths are displayed in the Viridis color map (Nuñez et al., 2018), with darker shades of blue indicate increasing travel lengths. The avalanches 12, 14, and 5 are selected based on their different slope geometries. Avalanche 12 (Figure 11) occurred on a steep slope with a sharp transition to the flat valley bottom. The shape of the slope in the upper part perpendicular to the slope gradient is convex, transitioning into multiple smaller channels towards the valley bottom. Avalanche 14 (Figure 10) exhibits a less steep slope gradient and a concave shape perpendicular to the slope gradient. Avalanche 5 (Figure 12) is characterized by a flat section in the upper part followed by a second steep area down-slope.

Figure 11 shows that the modeled travel length of avalanche 12 with an exponent of 2 results in a significant spread of the affected area. In contrast, the simulation result with an exponent of 30 affects a much smaller area. The variations in alpha angle from 26° to 30° exhibit relatively minor differences, as all avalanches reach the valley floor. Only from an alpha angle of 34° can the avalanche no longer reach the valley floor.

Figure 10 (avalanche 14) displayed a less pronounced effect of an increasing exponent value, resulting in similar lateral spreading across all modeled travel lengths. However, for alpha angles greater than 26°, the extent of the documented avalanche is no longer covered.

The modeled travel lengths of avalanche 5, shown in Figure 12, also exhibit minimal changes in the affected area with increasing exponents. However, another phenomenon becomes evident. The PRA pixels (bluish points) are divided into two distinct regions, an upper and a lower PRA section (the PRAs are omitted to enhance the readability of the modeled travel length in the lower row of Figure 12). With an alpha angle of 26°, the simulation results of the upper PRA section generosity overlap with the lower region, resulting in one contiguous avalanche. However, the effect is less pronounced with an alpha angle of 28°. In this case, a significant portion of the avalanche remains in the upper flat part of the slope, while only a tiny portion travels far enough to enter the lower part. This portion overlaps with the lower simulation results and spreads out based on the exponent value. The overlapping of the steeper section highlights the Flow-Py behavior in that pixels with a higher local energy height overrule lower ones.

In summary, the qualitative analysis reveals distinct patterns in the behavior of different avalanches in different slope morphologies. Avalanche 12 (Figure 11) demonstrates sensitivity to the exponent while displaying less sensitivity to the alpha angle. Conversely, avalanches 14 (Figure 10) and 5 (Figure 12) exhibit sensitivity to the alpha angle but display less sensitivity to the exponent. Moreover, the simulation results of avalanche 5 showcase the significant influence of *overruling effects*. These effects are observed when the simulation results are initiated from higher PRAs with a higher local energy height overlap with the simulation results initiated from lower PRAs. The analysis reveals a significant dependency of the sensitivity of the alpha angle or exponent on the different slope morphologies. Particularly the exponent, is strongly influenced by the shape of the slope perpendicular to the slope gradient. Convex slopes demonstrate heightened sensitivity, whereas concave slopes exhibit greater resistance.

Taking into consideration the observed phenomena, an exponent value of 8 is being utilized for the ongoing Flow-Py investigations and the model chain. This choice acknowledges the influence of slope morphology on the exponent parameter and ensures a balanced representation of avalanche behavior in varying slope morphologies in the Flow-Py simulations. Additionally, this exponent is supported by the statements of D'Amboise, Neuhauser, et al. (2022).

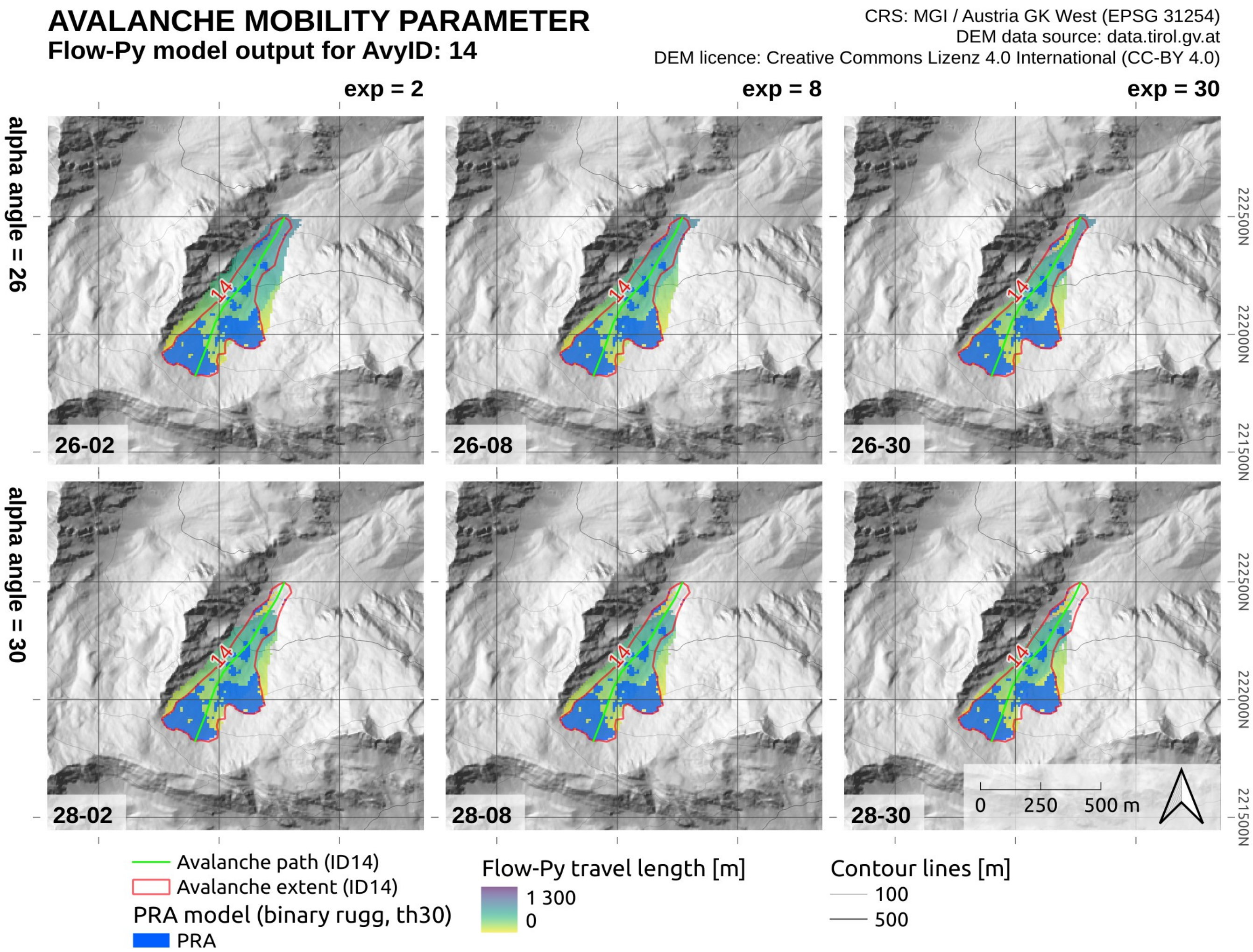

Figure 10: Qualitative assessment of the Flow-Py parameter, showing the comparison of the modeled travel length for avalanche 14 with an alpha angle of 26° and 30°, displayed in the rows of the figure, with a corresponding exponent value of 2, 8, and 30 displayed in the columns of the figure.

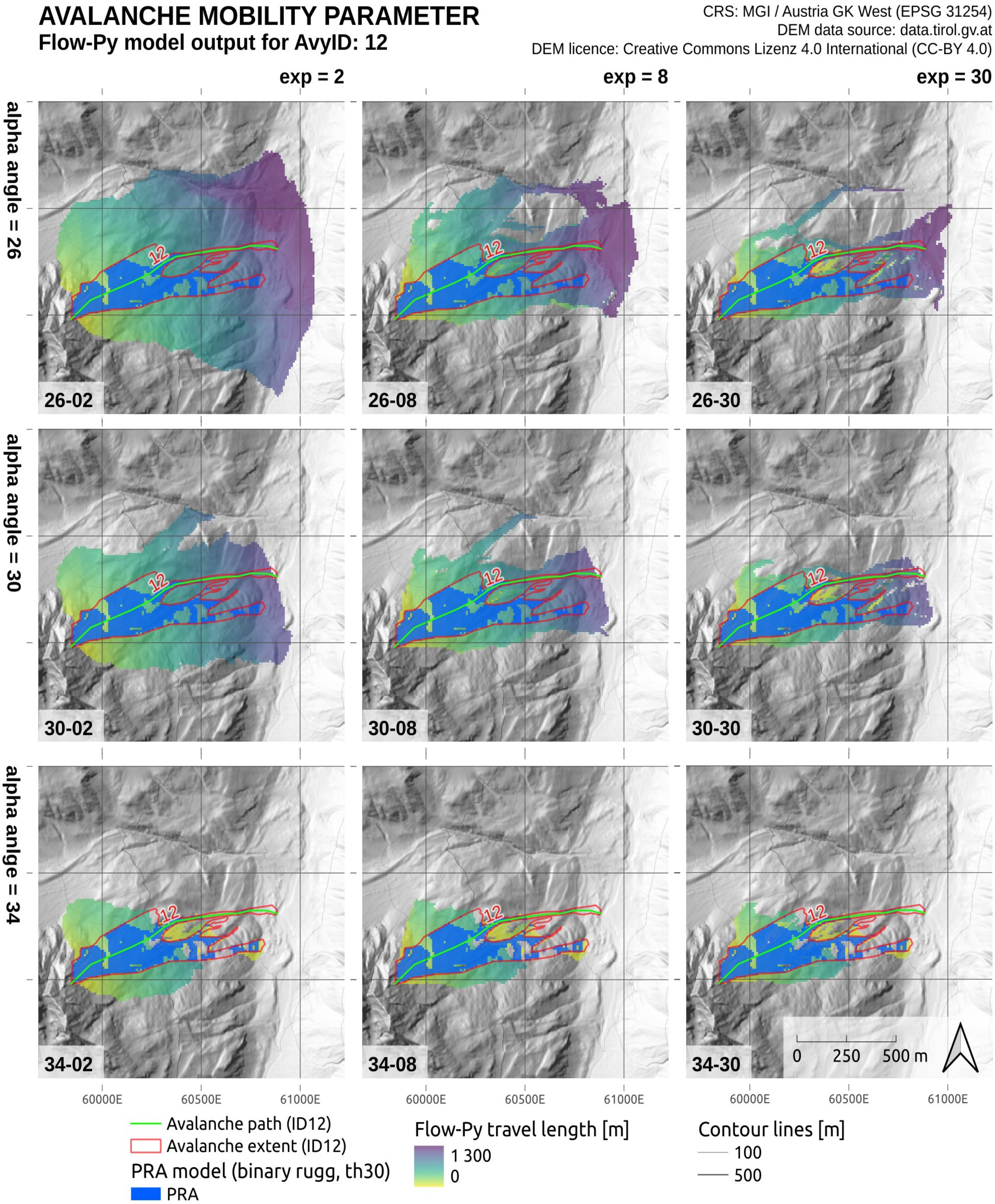

Figure 11: Qualitative assessment of the Flow-Py parameter, showing the comparison of the modeled travel length for avalanche 12 with an alpha angle of 26°, 30°, and 34°, displayed in the rows of the figure, with a corresponding exponent value of 2, 8, and 30 displayed in the columns of the figure.

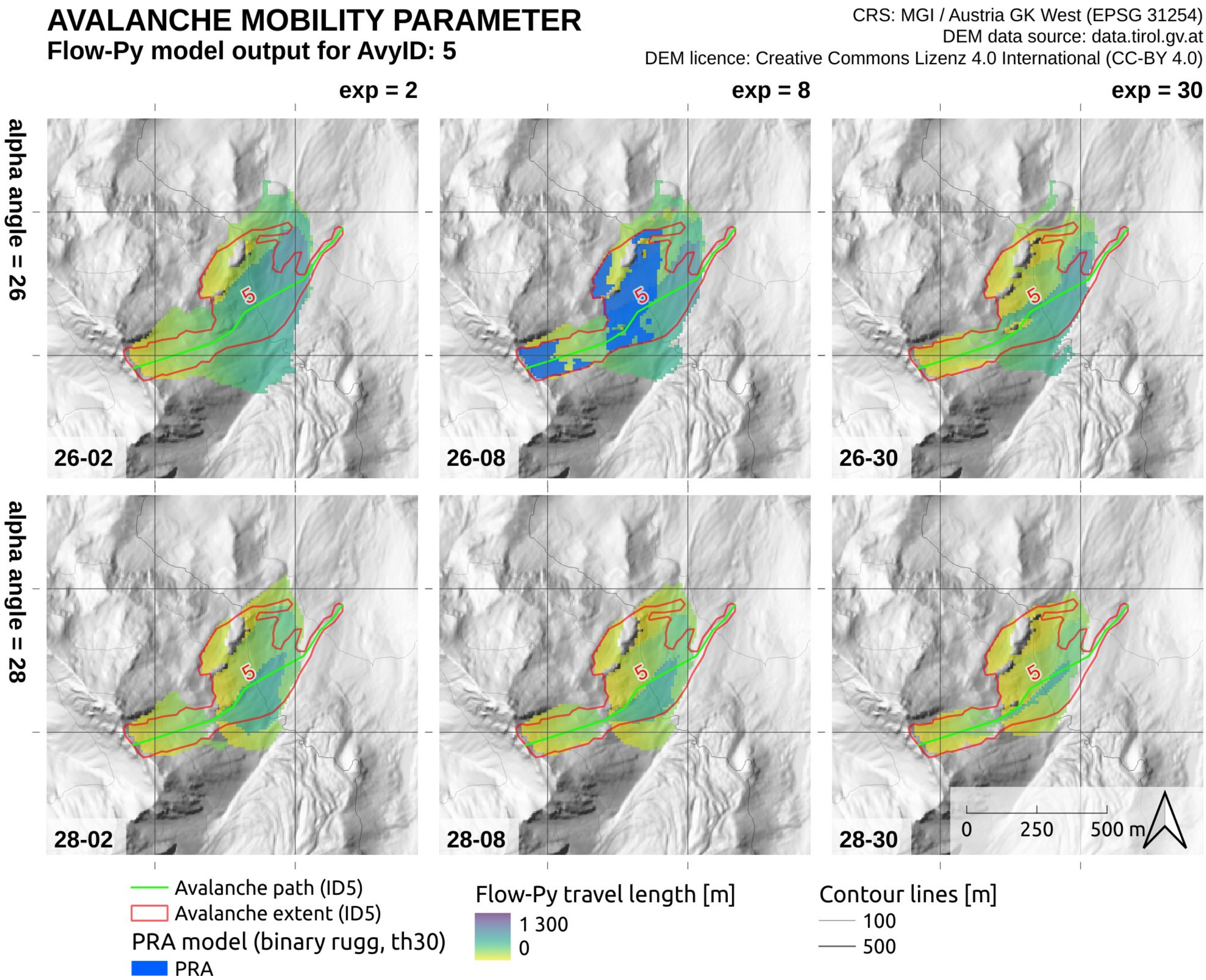

Figure 12: Qualitative assessment of the Flow-Py parameter, showing the comparison of the modeled travel length for avalanche 5 with an alpha angle of 26° and 28°, displayed in the rows of the figure, with a corresponding exponent value of 2, 8, and 30 displayed in the columns of the figure.

4.2.2 Quantitative comparison of modeled with mapped travel lengths (OA 2)

The modeled travel lengths are compared to the travel length of 19 avalanches of the AUT AWS Avalanche Reference Dataset (3.2.2). The same PRA layer as described in Section 4.2.1 is used as input. In order to compare the travel length of the simulations, the mapped avalanches of the AUT AWS Avalanche Reference Dataset are analyzed. The analysis involves the derivation of the alpha angle. The alpha angle is defined as:

$$\tan(\alpha) = \frac{vertical\, drop\, height\,[m]}{projected\ path\, length\,[m]}$$

The projected path length or travel length is derived from the manually defined avalanche path, which extends from the approximate highest point to the lowest point within the mapped area. The start and end elevations required to calculate the vertical drop height are extracted from the 10m DEM, along with the projected length of the defined path.

To evaluate the plausibility of a specific Flow-Py alpha angle parameterization, the RMSE is used as a criterion. The RMSE provides a measurement of the overall difference between the simulated and observed avalanches. A lower RMSE indicates a better fit, suggesting that the modeled travel lengths closely match the travel lengths of the AUT AWS Avalanche Reference Dataset. Conversely, a higher RMSE suggests overestimating or underestimating the modeled travel lengths. The RMSE is calculated for each alpha angle parameter separately, considering all 19 avalanches in one evaluation. The RMSE is calculated after the following equation:

$$RMSE = \sqrt{\frac{1}{n}\sum_{i=1}^{n}(y_i - \hat{y}_i)^2}$$

Table 12 presents the analysis of the 19 avalanches from the AUT AWS Avalanche Reference Dataset, providing statistical quantities. For instance, the mean travel length is 649.1 m, accompanied by a mean alpha angle of 26.85°.

Table 13: **Analysis of the AUT AWS Avalanche Reference Dataset**

Avalanche ID	**Alpha Angle [°]**	**Travel Length [m]**	**Vertical Drop Heigth [m]**
0	28.36	969.75	523.38
1	24.62	501.51	229.81
2	23.04	548.16	233.17
3	32.68	524.18	336.29
4	27.85	732.77	387.10
5	24.97	922.60	429.66
6	24.66	680.59	312.46
7	27.84	157.35	83.11
8	30.47	1218.78	717.16
9	28.64	736.87	402.45
10	24.76	403.14	185.93
11	27.98	483.56	256.90
12	31.40	1129.32	689.30
13	22.14	517.95	210.76
14	25.62	775.22	371.68
15	34.60	554.21	382.32
16	23.94	629.52	279.53
17	25.71	352.44	169.70
18	20.87	495.38	188.89
Min	20.87	157.35	83.11
Quartile 25%	24.28	489.47	199.83
Median	25.62	548.16	279.53
Quartile 75%	28.31	734.82	384.71
Max	34.60	1218.78	717.16
Mean	26.85	649.12	336.29

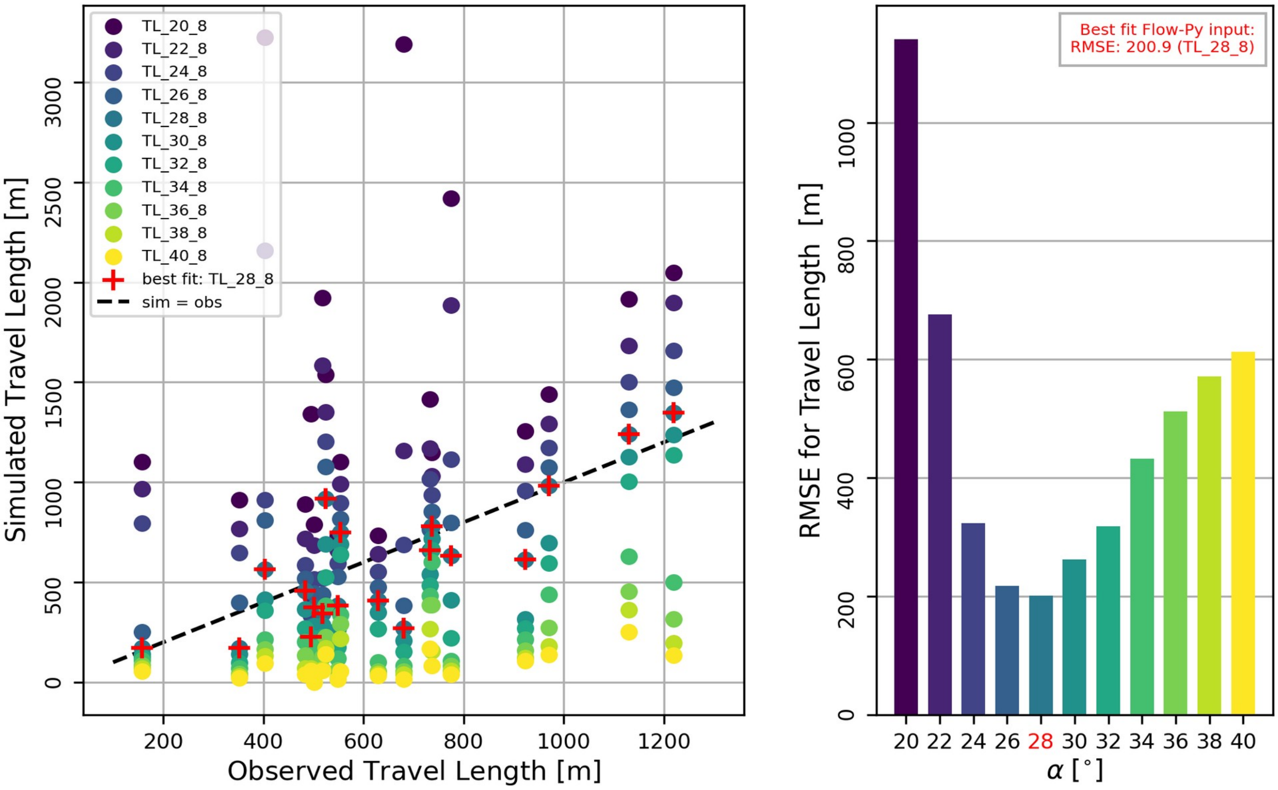

Figure 13:Quantitative analysis of modeled travel length with alpha angles ranging from 20° to 40° compared to AUT AWS Avalanche Reference Dataset (left). The dotted line represents a perfect 1-to-1 match, where modeled and observed travel lengths coincide. Corresponding RMSE values are shown in the right plot, with the lowest RMSE at 28° (marked in red).

Figure 13 depicts the effects of different alpha angles on the modeled travel length of the Flow-Py simulations. The dotted line represents a perfect 1-to-1 match, where the modeled travel length aligns with the observed travel length, as stated in Table 13. The vertical distance between the simulated travel length and the 1-to-1 line serves as an indicator of the accuracy of the simulation. A larger distance indicates a greater deviation in meters between the simulated and observed travel length. The RMSE serves as a metric to quantify the accuracy of the simulation results obtained with a specific alpha angle, as displayed in Table 12. Figure 13 reveals that larger alpha angles correspond to shorter travel lengths (yellowish points), while lower alpha angles result in longer travel lengths (blueish points). The trend of the RMSE is depicted in the right plot of Figure 13. The RMSE reaches its maximum value for the travel length with an alpha angle of 20° and steeply decreases over four steps as the alpha angle increases. RMSE values are minimized within the range of 26° to 30°, with the lowest value occurring at 28°, corresponding to an RMSE of 200.9 m. However, as alpha angles increase beyond this range, RMSE values gradually escalate.

In summary, the quantitative comparison of the modeled travel length with the 19 size 3 avalanches from the AUT AWS Avalanche Reference Dataset suggests that an alpha angle within the range of 26° to 30° yields plausible results, as evidenced by the minimal RMSE values. Table 14 displays the RMSE values for alpha angles within the range of 24° to 30°. The alpha angle of 26° exhibits the lowest RMSE at 0.85° to the mean alpha angle of the AUT AWS avalanche reference data, indicating a reasonable correlation of the simulated travel lengths with the observed mean alpha angle of 26.85° from the AUT AWS Reference Dataset.

Table 14: Correlation between RMSE of modeled travel length and corresponding RMSE for alpha angles of 19 avalanches in the AUT AWS Avalanche Reference Dataset. Presented for alpha angle range of 24° to 30°.

Alpha Angle [°]	RMSE travel length [m]	RMSE alpha angle [°]
24°	323.6	2.85
26°	217.0	0.85
28°	200.9	1.15
30°	261.9	3.15

Within the context of the ATES classification, these findings could be adopted as suitable alpha angle thresholds for the challenging class, aligning with size three avalanches based on their travel lengths and the agreement with the AUT AWS Avalanche Reference Dataset. However, due to the relatively limited size of the dataset, its robustness is somewhat constrained. To enhance the reliability of the findings, the analysis is extended to include a broader scope. Specifically, this involves the consideration of 100 randomly selected avalanches distributed across the entire study area, as detailed in the subsequent section.

4.2.3 Quantitative comparison of the mobility model with size classification ranges (OA 3)

A quantitative analysis is performed to refine further the determination of a plausible alpha angle range corresponding to size 3 avalanches for the ATES classification step. This analysis encompasses the evaluation of the modeled travel length, affected area, and impact pressure concerning established size 3 avalanche ranges. To conduct this comparison, distinct and well-defined ranges are essential. However, the existing size classification schemes, such as the EAWS (2023), offer only semi-quantitative descriptions of potential damage, runout, and length, while the CAA (2016) provides similar descriptions but also only includes typical values for impact pressure, path length, and mass rather than volume.

These schemes serve as a foundation for creating discrete classes, considering travel length, volume, impact pressure, and affected area. The typical dimensions for the length of the EAWS scheme are applied as travel length (E_{tl}). The limits of the E_{tl} ranges correlate with the typical path lengths from the CAA (2016).

The mean value between two classes is used as the boundary to establish discrete classes for volume (E_v, EAWS, 2023) and impact pressure (C_{ip}, Canadian Avalanche Association, 2016). Additionally, the affected area (B_{aa}) is applied according to the ranges outlined in Bühler et al. (2019). To correlate the typical mass [t], as indicated by the CAA (2016), with the typical volume values per size class provided by the EAWS (2023), a density of 200 kg m^{-3} is required. The derived size classification ranges are presented in Table 15 and Figure 14.

Table 15: Discrete avalanche size classification ranges for travel length (E_{tl}), impact pressure (C_{ip}), volume (E_v), affected area (B_{aa}) (Bühler et al., 2019)

Size	**Travel length** **E_{tl} [m]**	**Impact Pressure** **C_{ip} [kPa]**	**Volume** **E_V [m³]**	**Affected area** **B_{aa} [m²]**
Small	≤ 50	≤ 5	≤ 500	≤ 500
Medium	> 50 & ≤ 200	> 5 & ≤ 50	> 500 & ≤ 5,000	> 500 & ≤ 10,000
Large	> 200 & ≤ 1,000	> 50 & ≤ 250	> 5,000 & ≤ 50,000	> 10,000 & ≤ 80,000
Very large	> 1000 & ≤ 2000	> 250 & ≤ 750	> 50,000 & ≤ 150,000	> 80,000 & ≤ 500,000
Extremely large	> 2000	> 750	> 150,000	> 500,000

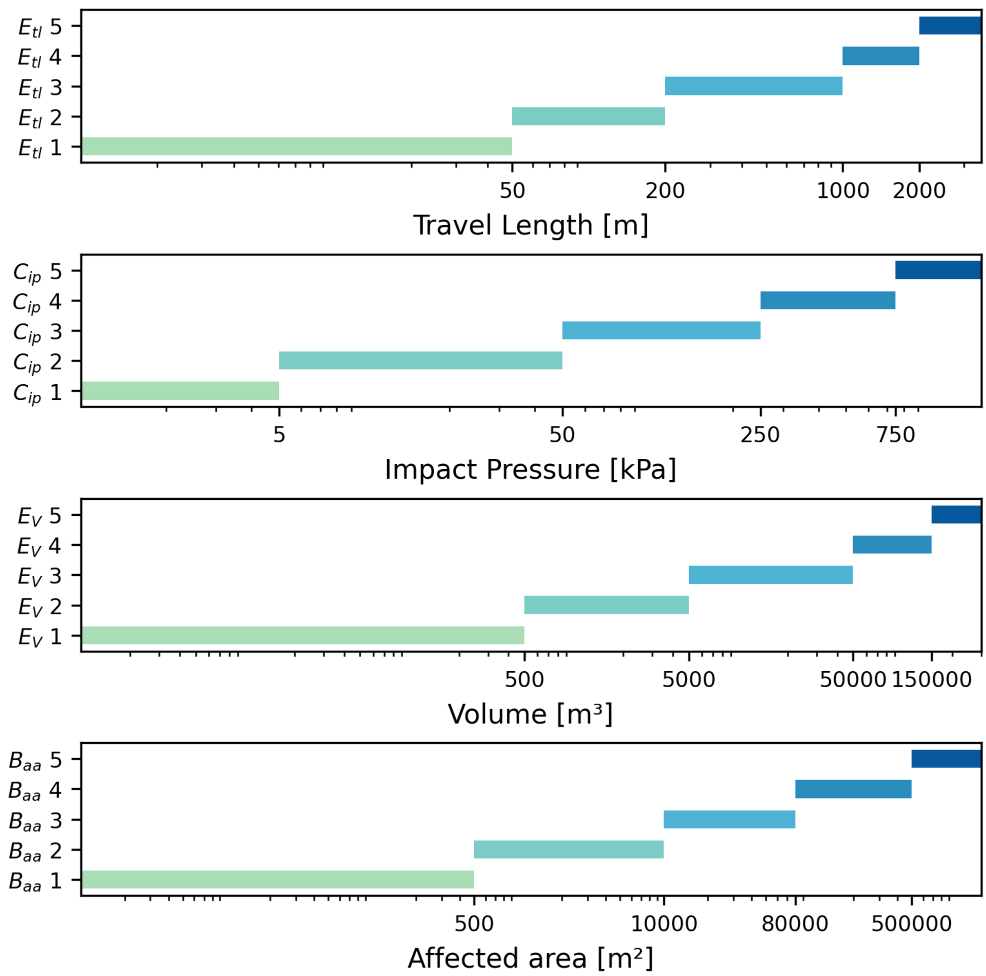

Figure 14: Discrete avalanche size classification ranges for travel length (E_{tl}), impact pressure (C_{ip}), volume (E_v), affected area (B_{aa}) (Bühler et al., 2019)

In OA 3, the initiating PRAs are randomly selected. The selection of PRAs is determined to match size 3 avalanches according to the size classification stated in Table 15. The size estimation is based on a simplified model, where the avalanche volume is approximated by multiplying an assumed average release thickness of 0.5 m with the area covered by the delineated PRA. The assumed release height is derived from Harvey et al. (2018), who utilized this release height for simulating size 3 avalanches. It is assumed that an avalanche initiated from an area of 20,000 m^2 can yield a maximum volume of 10,000 m^3, corresponding to an avalanche size 3 after the volume (EAWS, 2023). It is important to note that this estimation neglects potential entrainment processes. As a result of this assumption, PRAs with an area of 10,000 to 100,000 m^2 are considered for further analysis. The distribution of the area of the selected PRAs is displayed in Figure 15, indicating that almost two-thirds of the selected PRAs cover an area of below 30,000 m^2. The 100 chosen PRAs collectively span 3.10 km^2, accounting for approximately 1.3% of the total PRA-covered area within the study region.

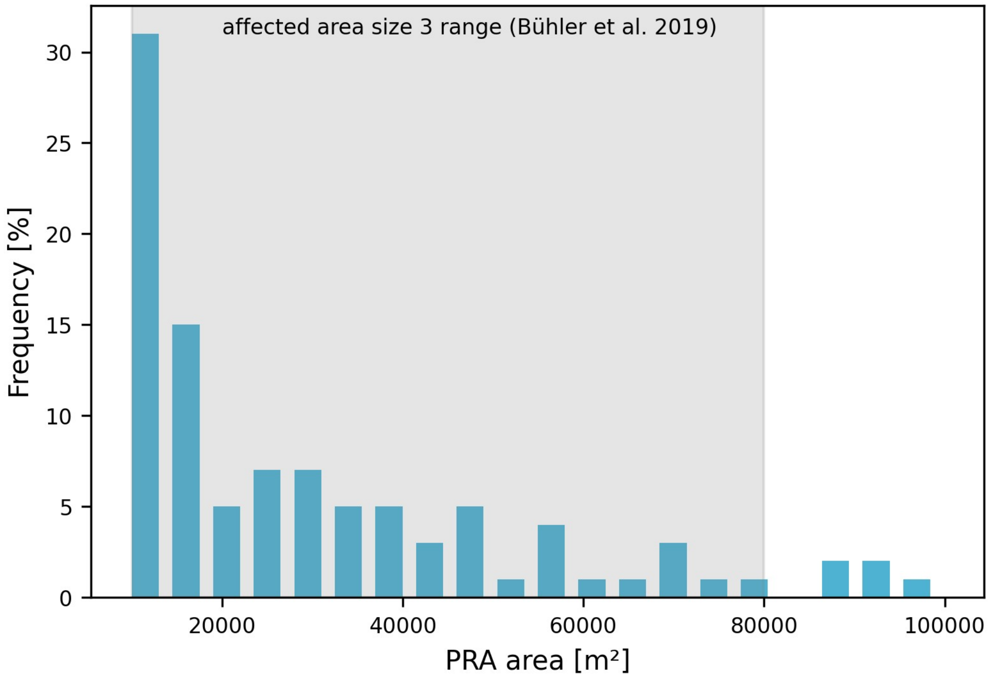

Figure 15: The distribution of the single PRA area coverage among the 100 selected PRAs is based on the classification of volumes corresponding to size 3 avalanches (E_v).

The results of the comparison are revealed in the following. The plots illustrate the distribution of the modeled travel length (Figure 16), the affected area (Figure 18), and the impact pressure (Figure 18) across the size classification ranges, modeled with rising alpha angles from 20° to 40° in steps of two. The blue bars represent the count of underestimated avalanches, while the red bars represent the count of overestimated avalanches. The green bars indicate the count of avalanche simulation results that fall within the defined size classification ranges, hereafter referred to as range fit TL for travel length, range fit AA for affected area, and range fit IP for impact pressure.

Figure 16 shows that within the alpha angle range of 26° to 38°, more than half of the modeled travel lengths align with the expected travel length classification of 200 to 1,000 m for size 3 avalanches. Within this range, the number of overestimations decreases from 39 at an alpha angle of 26° to 5 at an alpha angle of 38°. The maximum range fits TL are concentrated within the peak range of 28° to 30°, accounting for almost two-thirds of the total count. However, the number of avalanches exceeding the size range is between 29 to 25%. The analysis of the affected area (Figure 17) demonstrates that underestimations are extremely infrequent, with only two instances observed at 38° and 40°.

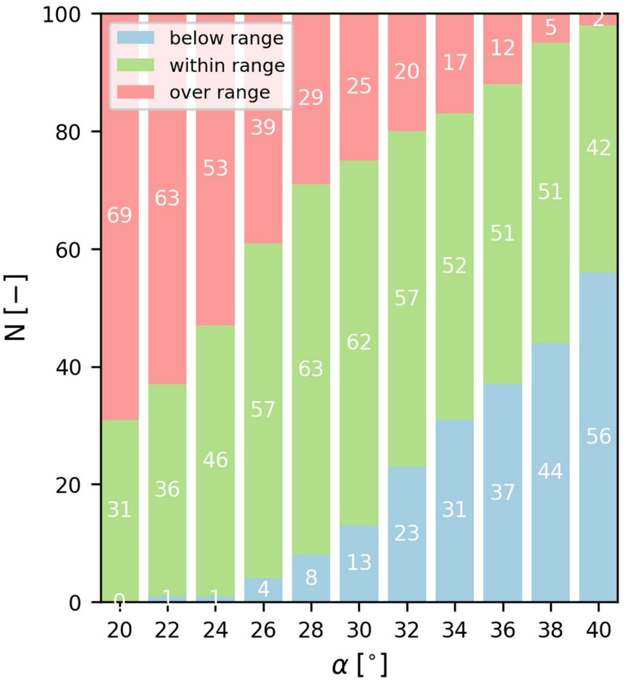

Figure 16: Comparisons of modeled travel length for 100 avalanches with varying alpha angles from 20° to 40°, relative to the travel length size 3 classification range (E_{tl}=200-1,000 m).

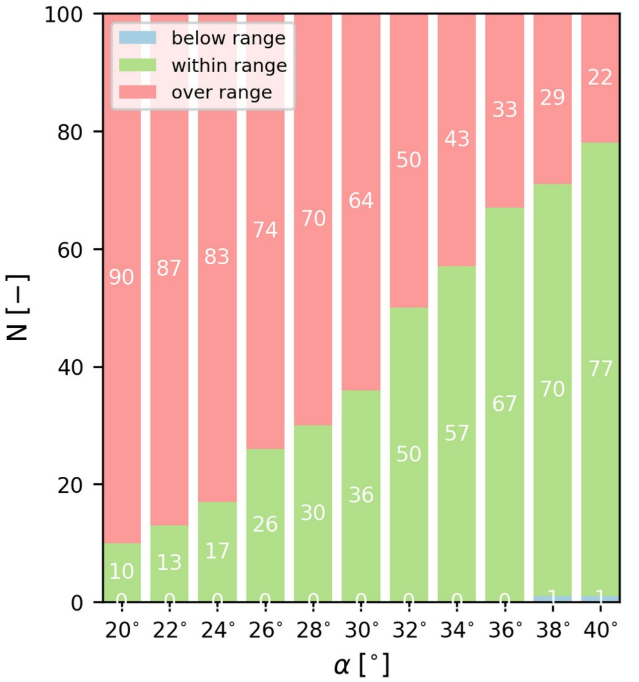

Figure 17: Comparisons of modeled affected area for 100 avalanches with varying alpha angles from 20° to 40°, relative to the affected area size 3 classification range (B_{aa}=10,000-80,000 m³) according to Bühler et al. (2019)

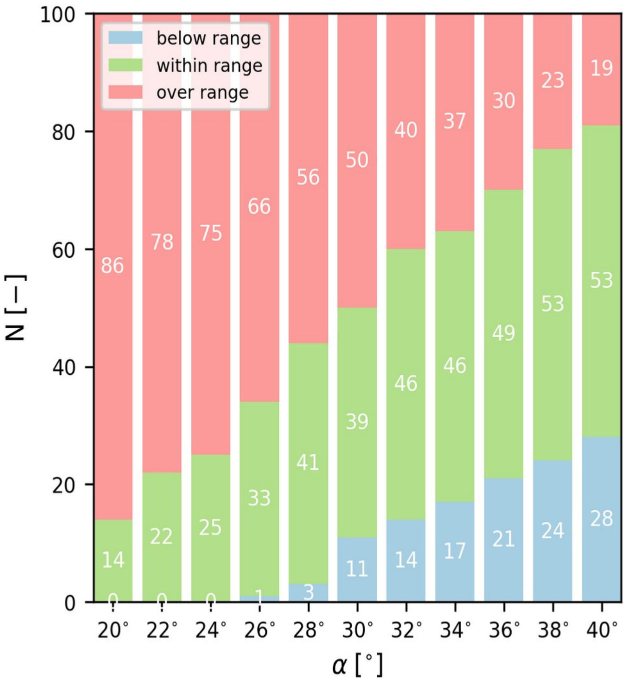

Figure 18: Comparisons of modeled impact pressure for 100 avalanches with varying alpha angles from 20° to 40°, relative to the impact pressure size 3 classification range (C_{ip} = 50-250 kPa).

Furthermore, consistent with the trends observed in the travel length analysis, the count of overestimation decreases from 90 at 20° to 22 at 40°. The relationship between the simulated impact pressure and the size classification range is depicted in Figure 18. The plot shows a continuous increase of range fits IP falling within the size classification range of 50 to 250 kPa as the alpha angle increases. With an alpha angle of 32° or higher, approximately 50% of the modeled avalanches are within the size 3 range. The number of overestimations in the range drops from 40 at 32° to 19 at 40°.

In summary, by comparing the modeled travel length, affected area, and impact pressure of 100 randomly selected avalanches with the size classification ranges outlined in Table 15 and Figure 14, identifying a single alpha angle that universally fits all size classification scopes proves challenging.

To differentiate the different size classification approaches in OA 3, the different size classification approaches are compared by plotting the assumed release volume against the affected area (Figure 19), as well as the modeled impact pressure (Figure 20) and the modeled affected area (Figure 21) against the modeled travel resulting from a 30° alpha angle. The plots show the travel length size classes on the x-axis and size classes for the affected area or impact pressure on the y-axis.

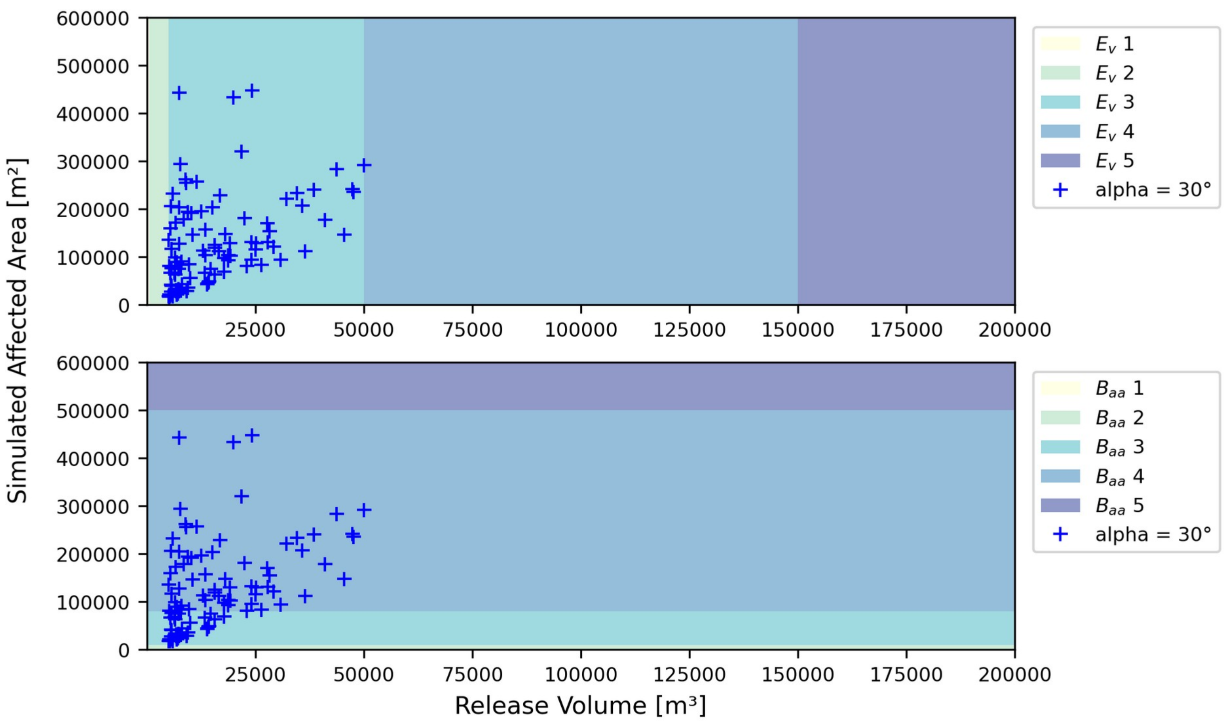

Figure 19: Release volume plotted against the simulated affected area, along with the size classification ranges based on release volume (E_v) in the upper plot and affected area (B_{aa}) in the lower plot.

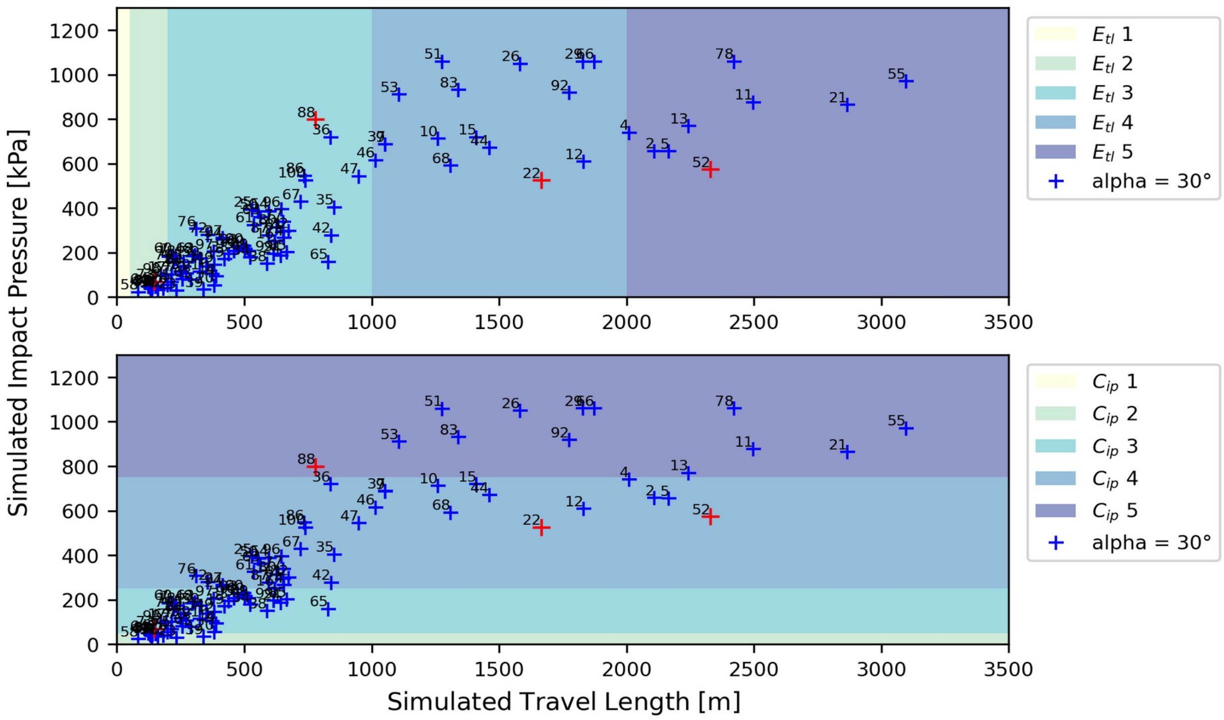

Figure 20: Simulated travel length plotted against simulated impact pressure, along with the size classification ranges based on travel length (E_{tl}) in the upper plot and impact pressure (C_{ip}) in the lower plot. The red crosses mark the examples for Figure 22.

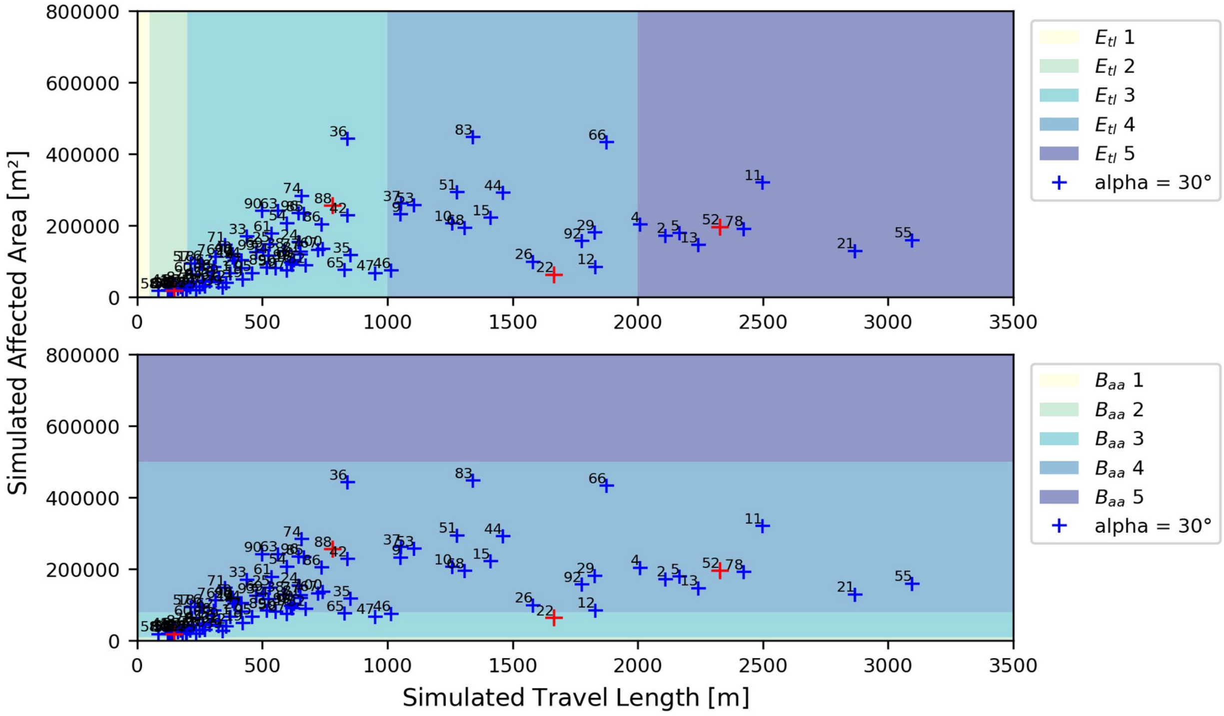

Figure 21: Simulated travel length plotted against simulated affected area, along with the size classification ranges based on travel length (E_{tl}) in the upper plot and affected area (B_{aa}) in the lower plot. The red crosses mark the examples for Figure 22

The plots reveal different outcomes for size classification based on travel length, impact pressure, or affected area. For instance, using travel length leads to 62 avalanches in size class 3. However, with affected areas, only 36 avalanches fall into class 3, and the remaining 26 are in class 4. Similarly, for modeled impact pressures, only 39 of the 62 avalanches are in class 3, while 11 are in lower classes, 49 in class 4, and 1 in class 5.

To visually illustrate these variations, Figure 22 displays four selected avalanches (marked with red crosses in Figure 20 and 21), all modeled at a 30° alpha angle and classified as size 3 according to the volume (E_v, Section 4.2.3). This visualization highlights significant variations with an alpha angle of 30° in travel length, affected area, and impact pressure across different avalanche simulations. For example, the travel length ranges from around 200 m (avalanche 73) to approximately 2500 m (avalanche 52). To establish a connection between the modeled avalanche size and slope coverage, a size classification relative to the path is estimated in classes R1 (Very small, relative to the path) to R5 (Major or maximum, relative to the path) (Table 2, American Avalanche Association, 2016). The orange line in Figure 22 represents the assumed avalanche path. The profile plots show the assumed avalanche path with vertical drop height against the projected path length.

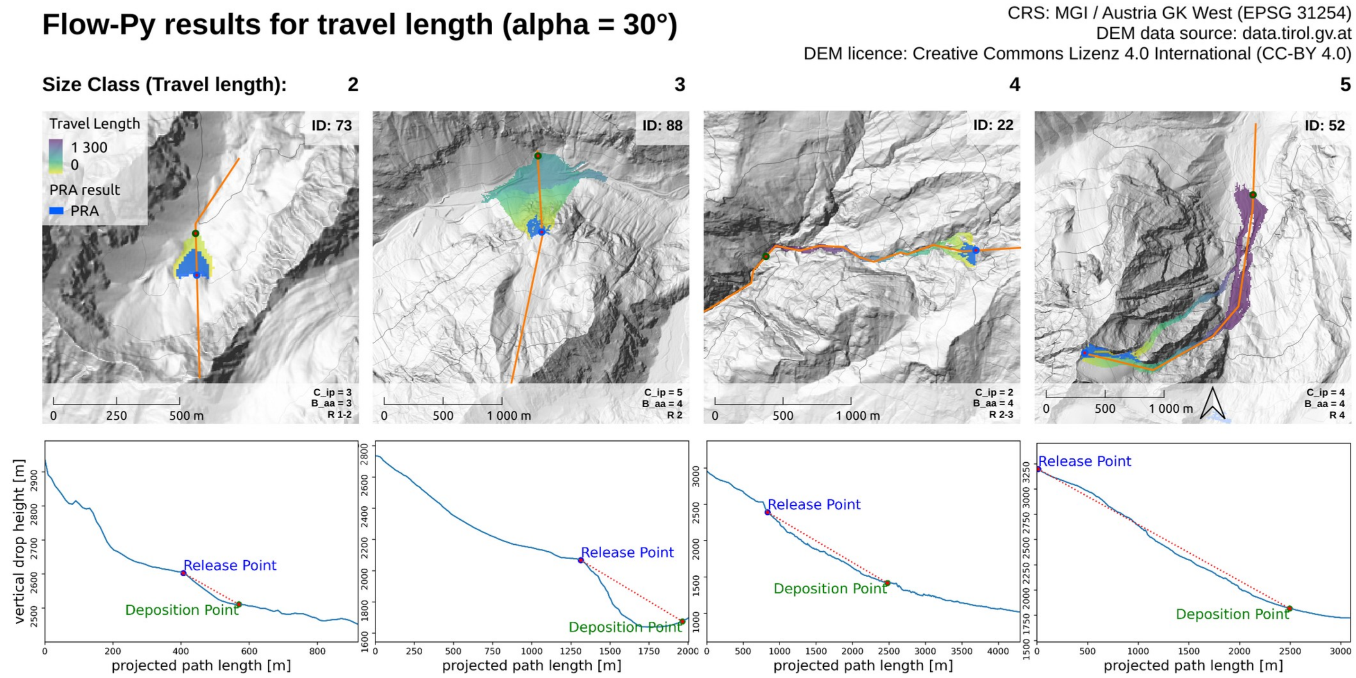

Figure 22: Maps view (upper row) showing varying avalanche size classes (E_{tl} 2 to 4 from left to right) based on the modeled travel length with an alpha angle of 30°, along with the corresponding assumed path (orange line), release point (blue point), and deposition point (green point), all avalanches are classified as size 3 according to the volume (E_v). The profile view (lower row) displays the energy height (red dotted line) across the avalanche path from release to deposition point.

For avalanche 73 (Figure 22), a size classification based on travel length falls within class 2, while considering the affected area or the impact pressure places the avalanche in size range 3. Compared to the classification based on the path, this could correspond to an R1 or even R2.

Avalanche 88 (Figure 22) exhibits two significant phenomena. Firstly, the avalanche fans out due to the convex shape perpendicular to the slope, as observed in the qualitative analysis in Section 4.2.1. Secondly, the narrow valley causes the avalanche to go uphill and spread even further. The steep release area results in a very high z delta (energy height), leading to a peak impact pressure of 813 kPa and a corresponding velocity of 64 m/s, classifying it as impact pressure class 5. However, this value appears somewhat unrealistic concerning the profile of the avalanche. Taking into account its size in relation to the slope, this avalanche would be classified as R2.

Avalanches 22 and 52 (Figure 22) are classified as size 4 and 5, respectively, based on the travel length, and both are classified as size 4 based on the affected area. The impact pressure is relatively low for avalanche 22, classifying it as class 2, while avalanche 52 is classified as size 4. Regarding the size relative to the slope, avalanche 22 would be classified as R2 to R3 and avalanche 52 as R4.

Table 16 summarizes the different size classes for the four chosen avalanches based on travel length, the affected area, and impact pressure and states a size assumption relative to the path.

In conclusion, the modeled avalanches with an alpha angle of 30° demonstrate a broad spectrum of results, highlighting the substantial influence of varying terrain. This suggests that slope morphology significantly determines the travel length, affected area, and impact pressure, leading to diverse outcomes for avalanches sharing the same alpha angle (Figure 22).

Table 16: Avalanche size classification for the avalanches with ID 73, 88, 22, and 52 based on the volume (E_v), travel length (E_{tl}), impact pressure (C_{ip}), affected area (B_{aa}) and relative to the slope (R)

Avalanche ID	**73**	**88**	**22**	**52**
E_v	3	3	3	3
E_{tl}	2	3	4	5
C_{ip}	3	5	2	4
B_{aa}	3	4	4	4
R	1-2	2	2-3	4

4.2.4 Avalanche mobility model parameterization for the model chain

The objective of evaluating the data-based avalanche mobility model Flow-Py (D'Amboise, Neuhauser, et al., 2022) for regional modeling of size 3 avalanche runout, particularly in the context of ATES terrain classification, is investigated along three comparison OA (OA 1, Section 4.1.1; OA 2, Section 4.2.2; OA 3, Section 4.2.3). This objective includes the essential definition of two different alpha angle thresholds within the ATES classification step. The determination of challenging terrain class considers the runout associated with the affected area between these alpha angle thresholds, while terrain affected by lower alpha angles is categorized as simple terrain, and terrain affected by higher alpha angles is considered as challenging terrain. The alpha angle threshold corresponding to the lower range of size three avalanches will establish the Flow-Py parameterization within the model chain. The findings of the alpha angle for the upper range of size 3 avalanches will also contribute to the parameterization for the ATES classification step.

In OA 1 (4.2.1), the impact of different alpha angles and exponents on the results of the Flow-Py simulations is presented. A qualitative parameter study is conducted using the documented affected area from observed avalanches. Figures 11, 10, and 12 present plausible results for back-calculating the affected area of the documented avalanches, using a sample of three avalanches as illustrative examples. However, a parameter set that fits all back-calculations cannot be determined. Through the evaluation process, an exponent value of 8 is determined to achieve a favorable balance between the different slope morphologies within the simulation results. This choice is reinforced by the statements of D'Amboise, Neuhauser, et al. (2022). Furthermore, the qualitative analysis highlights the importance of considering the impact of slope morphology on the simulation results of different avalanche paths.

In the quantitative analysis of OA 2 (4.2.2), the RMSE is used to analyze the deviation of modeled travel lengths across different alpha angles from the 19 size 3 avalanches of the AUT AWS Avalanche Reference Dataset. The analysis reveals that an alpha angle within the range of 26° to 30° yields plausible results, as evidenced by the minimal RMSE values. Regarding the ATES classifier, this result can be interpreted as a plausible alpha angle to capture the runout of size 3 avalanches and potentially serve as a threshold for the challenging terrain. However, the sample size of just 19 avalanches is rather small.

In OA 3, the modeled travel length, affected area, and impact pressures of 100 size 3 avalanches are compared with the avalanche size classification ranges, as stated in Table 15.

Comparing the modeled travel length with the expected travel length range for size 3 avalanches (E_{tl}= 200-1000 m), it is evident that over 50% of the avalanches lie within this size range for alpha angles between 26° and 38°. The peak count of avalanches within this size range occurs within the range of 28° and 30°. The alpha angles which result in the maximum count of avalanche within the size 3 range correlates with the lowest RMSE of OA 2.

A noticeable trend emerges in comparing the modeled affected area and impact pressure: the count of overestimations is approximately twice as high as the travel length counts across different alpha angles. This is due to the following limitations:

The selection of the PRAs is based on the volume assumption outlined in Section 4.2.3. This assumption involves multiplying the PRA area by an assumed release height of 0.5 m. As a result, PRAs within a size range of 10,000 to 100,000 m^2, corresponding to a volume range (E_v) of 5,000 to 50,000 m^3 (size 3 avalanches, Table 15), are included. This size range of PRAs significantly aligns with the classification by Bühler et al. (2019). However, two-thirds of the 100 selected PRAs have an area smaller than 30,000 m^2. The area covered by the PRAs already significantly overlaps with the size classification according to the affected area (B_{aa}).

Nevertheless, the volume or mass is linked to the routing flux; however, additional research is required to delve further into this matter. The consistently higher range of overestimation is also observed in the analysis of impact pressure as compared to the travel length. This observation might be linked to the derivation of the impact pressure (ip [kPa]) from the energy height (z delta). The derivation takes into account both the velocity (v [m s-1]) and the density (ρ [kg m-^{3}]). Obtaining an impact pressure estimate relies on the simple relation $ip = \rho\ v^2$ (Rudolf-Miklau & Sauermoser, 2011). The velocity (v) can be derived directly from the flow intensity result of Flow-Py (z delta) following the energy-line method after Körner (1980), and the flow density is assumed to be ~200 kg m^{-3}, which is in line with McClung & Schaerer (2006) but may deviate from actual circumstances. The frictional dissipation is given due to the geometric relations of the alpha angle concept (Heim, 1932; Lied & Bakkehøi, 1980) based on the law of conservation of energy and Coulomb friction of a block movement. This friction term can also be replaced or enhanced by other models, for instance, the Voellmy friction (Voellmy, 1955). Moreover, the size classification in the impact pressure scope considers the 99th percentile over the entire modeled avalanche path. An alternative approach could involve considering the impact pressure relative to specific path sections, such as the runout zone, as it is common for general avalanche hazard mapping for settlements and infrastructural facilities (Rudolf-Miklau & Sauermoser, 2011).

This observation indicates a relatively weak correlation and underscores the necessity for additional examination of these assumptions and constraints. When considering the parameterization of the Flow-Py model for the ATES classifier and addressing the limitations of the affected area and impact pressure, the focus for Flow-Py parameterization, based on the results from OA 3, will be placed on the travel length. Table 17 summarizes of the outcomes from OA 2 (Section 4.2.2) and 3 (Section 4.2.3). The determined alpha angle for the Flow-Py simulations is 26°, representing a conservative alpha angle for size 3 avalanches. This choice is based on the considerable RMSE increase and an 11% decrease in the range fit TL for smaller alpha angles, moreover, the alpha angle of 26° has the smallest alpha angle RMSE (0.85°). Further discussion on the alpha angle thresholds for the ATES terrain classification is presented in the subsequent section, focusing on the parameterization for the ATES classifier.

Table 17: Flow-Py assessment results for OA 2 and 3, the range fit reflects the count within the travel length, the affected area, or the impact pressure range of size 3 avalanches.

Alpha angle [°]	OA 2 RMSE [m]	OA 3 range fit TL [%]	OA 3 range fit AA [%]	OA 3 range fit IP [%]
20	1141.3	31	10	14
22	675.5	36	13	22
24	323.6	46	17	25
26	217.0	57	26	33
28	200.9	63	30	41
30	261.9	62	36	36
32	317.8	57	50	46
34	432.5	52	57	46
36	512.1	51	67	49
38	570.9	51	70	53
40	612.5	42	77	53

4.3 ATES classification

The autoATES v1.0 model (Larsen et al., 2020) is undergoing continuous improvements and enhancements (Schumacher et al., 2022). The ATES classifier used in this study builds upon recent developments and is provided by the working group of Sykes, J. and Toft, H. The classifier incorporates four distinct ATES classes: simple, challenging, complex, and a newly proposed class for extreme terrain (AAA, 2023; Statham, 2020). The terrain classification process relies on six layers: slope, PRA, avalanche runout, cell count, z delta, and a forest layer. This study uses the PCC Forest Layer, as derived in Section 4.1.2. In addition to that, this thesis incorporates an additional layer to account for glaciated areas (Glacier Layer, Section 3.3).

The flowchart (Figure 23) serves as a visualization of the workflow of the ATES classifier. In the first step of the ATES classification, the slope, avalanche mobility layer, and overhead exposure layer are reclassified along the corresponding thresholds, as stated in Figure 23 and Table 19. The algorithm combines the reclassified layers to generate the preliminary ATES classes by selecting the maximum value for each raster cell. In the subsequent step, the smoothing filter (Virtanen et al., 2020) is applied to the extreme class, using the ATES parameter sliding window size (WIN) to determine the smoothing effect. A WIN size of 1 will impact the data, while higher values for WIN will increase the smoothing effect; the autoATES default is 5.

The next step involves merging the PRA and forest information with the preliminary ATES classes. This is done by summing the preliminary ATES class value with the reclassified PRA and forest layers.

Subsequently, the raw ATES map is created using a rule-based classification approach. For example, if a forest is present, the preliminary ATES class is downgraded to a lower class. In the case of no PRA, moderate forest, and a preliminary ATES class of 3, the ATES class is reassigned as 1. Conversely, if there is PRA and open forest, along with a preliminary ATES class of 4, the ATES class remains 4 (Schumacher et al., 2022). In the subsequent step, the binary Glacier Layer is incorporated. A reclassification step assigns all raster values which are covered by glaciated areas at leased as challenging terrain.

In the final step of the ATES classifier, a smoothing algorithm is utilized to remove small isolated islands of equal classes. These isolated islands are determined based on the ATES classifier parameter ISL SIZE in square meters. In this step, the algorithm utilizes a label function (Fiorio & Gustedt, 1996; Wu et al., 2005), incorporating the connectivity information. The configuration allows for identifying neighboring pixels as connected, considering only the edges (connectivity = 1) or both the edges and vertices (connectivity = 2; auto ATES default).

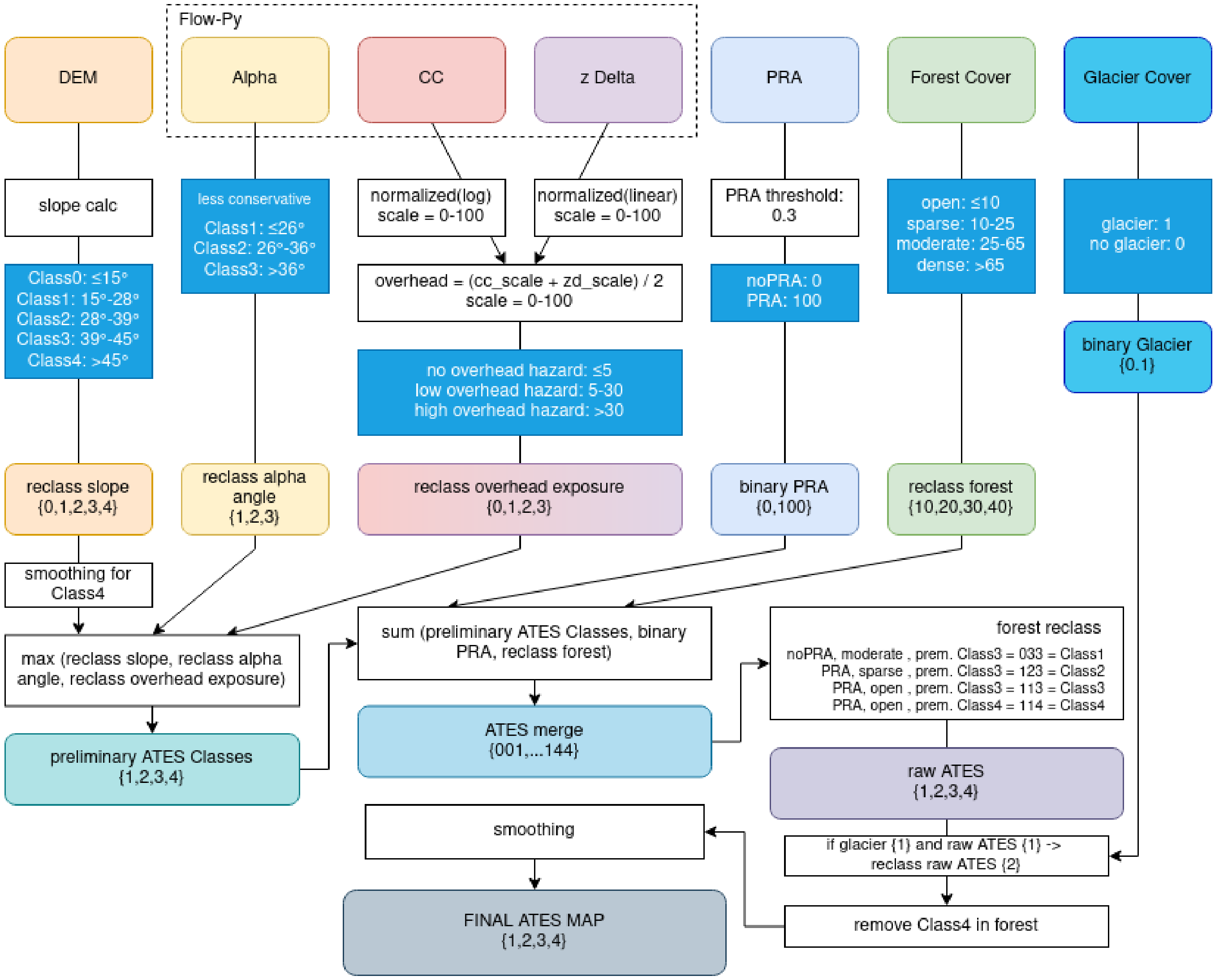

Figure 23: Workflow of the ATES classifier (third step of the model chain) based on Schumacher et al. and ongoing developments. The raster data formats are represented by the objects with rounded edges, such as input raster layers, the reclassification layers, preliminary ATES classes, raw ATES, and the final ATES map. Objects with sharp edges in blue represent thresholds for reclassification (regarding the less conservative alpha scenario). Additionally, white objects represent operations such as calculation, merging, reclassification, and smoothing applied to different layers. The Glacier Cover data and reclassification is incorporated in this study.

4.3.1 ATES parameterization

The parameterization process is described in detail below. As depicted in Figure 23, the classification step involves the integration of the 10m DEM, the forest layer, represented in the percentage of canopy cover (PCC Forest Layer), the results from the PRA model and the avalanche mobility model, as well as a newly introduced layer to incorporate glacier (Glacier Layer).

The availability of the 10m DEM is detailed in Section 3.1. The source of the Glacier Layer is provided in Section 3.3. The PCC Forest Layer is obtained through the difference between 1m DTM and 1m DSM, as demonstrated in Section 4.1.2. The PRA layer is determined in Section 4.1.3. Subsequently, the Flow-Py simulation results are obtained in Section 4.2.4.

The parameterization of the ATES classifier is discussed in the following:

(1) **Slope angle threshold**

The angle threshold forms with the alpha angle thresholds and the overhead exposure the primarily ATES classes. The following Table 18 states an overview about the slope angle thresholds in previous ATES studies.

Table 18: Summary of slope angle thresholds for ATES classification in previous studies and the current study (* regarding open slopes)

Literature	Approach	Simple	Challenging	Complex	Extreme
Statham et al. (2006)	Qualitative	generally < 30º	Mostly low angle, isolated slopes > 35º	Variable with large % > 35º	-
Larsen et al. (2020)	Quantitative	≤ 25°	> 25° & ≤ 40°	> 40°	-
Schumacher et al. (2022)	Quantitative	≤ 25°	> 25° & ≤ 31°	> 37°	-
AAA (2023) Statham (2020)	Qualitative	< 20°	< 30°; or some slopes > 35°	< 35°; with large proportions > 35°	> 35°; with a large proportion > 45°
This study	Quantitative	< 28°	> 28° & ≤ 39°	> 39° & ≤ 45°	> 45º

The alpha angle threshold for the simple-challenging boundary is set to 28°, which is less conservative as stated by previous studies (Larsen et al., 2020; Schumacher et al., 2022) but still aligns with the original ATES (Statham et al., 2006). Furthermore, 28° corresponds to the lower slope angle range for PRAs, as stated in Section 2.5.1. The upper limit for the challenging terrain is set to 39°, which seems to be a plausible balance among the stated values in Table 18. Moreover, 39° corresponds to the median slope angle of the avalanche release, as described in Section 2.1. The boundary between complex and extreme terrain is established at 45°. This threshold is derived from the qualitative description of the extreme class (AAA, 2023; Statham, 2020).

(2) **Alpha angle threshold**

To counter the challenge outlined in Section 4.2.4, aimed at establishing two alpha angle thresholds for the ATES classifier, an examination of the CH SPOT6 Avalanche Reference Dataset (Toft et al., 2023) is contextualized with the previous findings. This dataset comprises over 18,000 documented avalanches and includes parameters like affected area, travel length, and alpha angle.

Figure 24 illustrates the alpha angle distribution for observed avalanches and their corresponding avalanche size classifications (Toft et al., 2023). The plots illustrate two size classifications: firstly, based on the travel length range used in this study, and secondly, based on the affected area (Bühler et al., 2019). The plots reveal a weak correlation between the alpha angle and avalanche size, regardless of whether it is based on travel length or affected area. This observation aligns with the findings of the assessment of the avalanche mobility model in Section 4.2.4.

Concerning the ATES terrain classification, this indicates that establishing a distinct alpha angle that directly corresponds to a single-size class is challenging in a regional model scenario across multiple avalanche paths. Considering the variability of simulation results with a single alpha angle spanning various size classes (Figure 20, Figure 19, Figure 22) and the limited correlation between the alpha angle and size class as shown in Figure 24, an alternative approach is explored. This approach considers the empirical cumulative distribution function (ECDF) of the CH SPOT6 Avalanche Reference Dataset, as depicted in Figure 25. Notably, the data from the large-scale analysis approximates a normal distribution. The method entails matching reasonable alpha angles from OA s 2 and 3 with the ECDF and discussing the associated percentiles in the context of the ATES classification step.

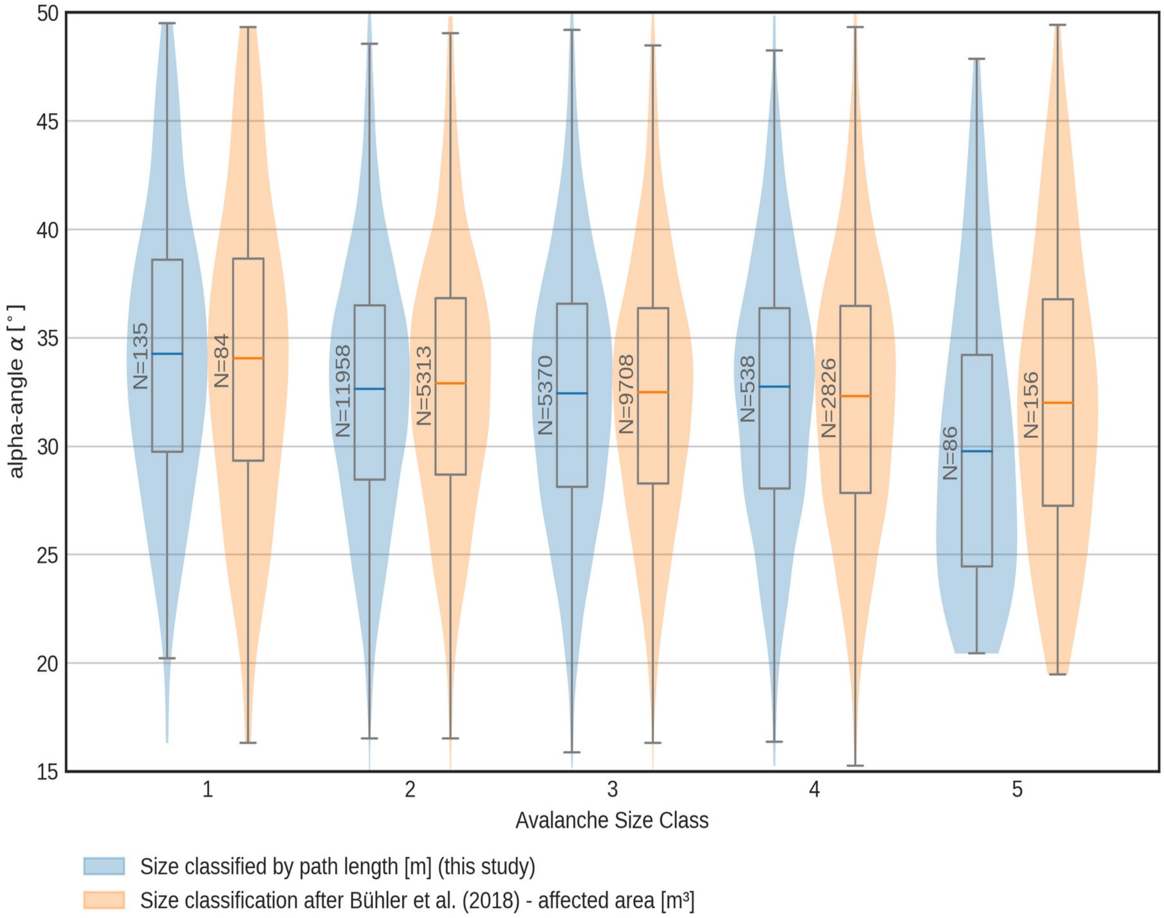

Figure 24: The distribution of alpha angles for avalanche size classes from the CH SPOT6 Avalanche Reference Dataset based on the classification after the travel length (E_{tl}) is shown in blue, while the classification after the affected area (B_{aa}) is represented in orange (EAWS, 2023; Heim, 1932; Jang et al., 1997; Lied & Bakkehøi, 1980; 2022; Statham et al., 2006; Toft et al., 2023).

In OA 2 (Section 4.2.2) and 3 (Section 4.2.3), alpha angles ranging from 26° to 32° demonstrate plausible outcomes, evidenced by their low RMSE for the travel length and range fit LT (> 57%) of modeled avalanches within the travel length size 3 class. In addition, the alpha angle 26° revealed the lowest a RMSE of 0.85° to the mean alpha angle of the AUT AWS Avalanche Reference Dataset. Regarding the ECDF analysis, the 15th percentile approximately corresponds to an alpha angle of 26°. The 50th percentile aligns with an alpha angle of around 32°. Moreover, a less conservative percentile is set to the 75th, which aligns with an alpha angle of 36°. In the context of OA 3, the less conservative alpha angle of 36° still accounts for over 50% of modeled travel lengths classified as size 3 avalanches. When establishing the alpha angle threshold for the ATES classification, these percentiles offer valuable insights for improving the interpretation of the integration of the avalanche runout model. In this context, the lower percentile serves as the threshold for the lower boundary of the challenging terrain class. In comparison, the higher percentile acts as the threshold for the lower boundary of the complex class.

Consequently, terrain falling between these two percentiles is designated as challenging. The terrain unaffected by the modeled avalanche runout is categorized as simple. Additionally, terrain exceeding the higher percentile is classified as complex. Notably, the extreme class lies outside the thresholds for the avalanche runout, implying that any potential avalanches are anticipated to traverse this class without stopping.

The more and the less conservative alpha angle for the challenging-complex terrain boundary are being considered for the ongoing assessment and testing of the model chain.

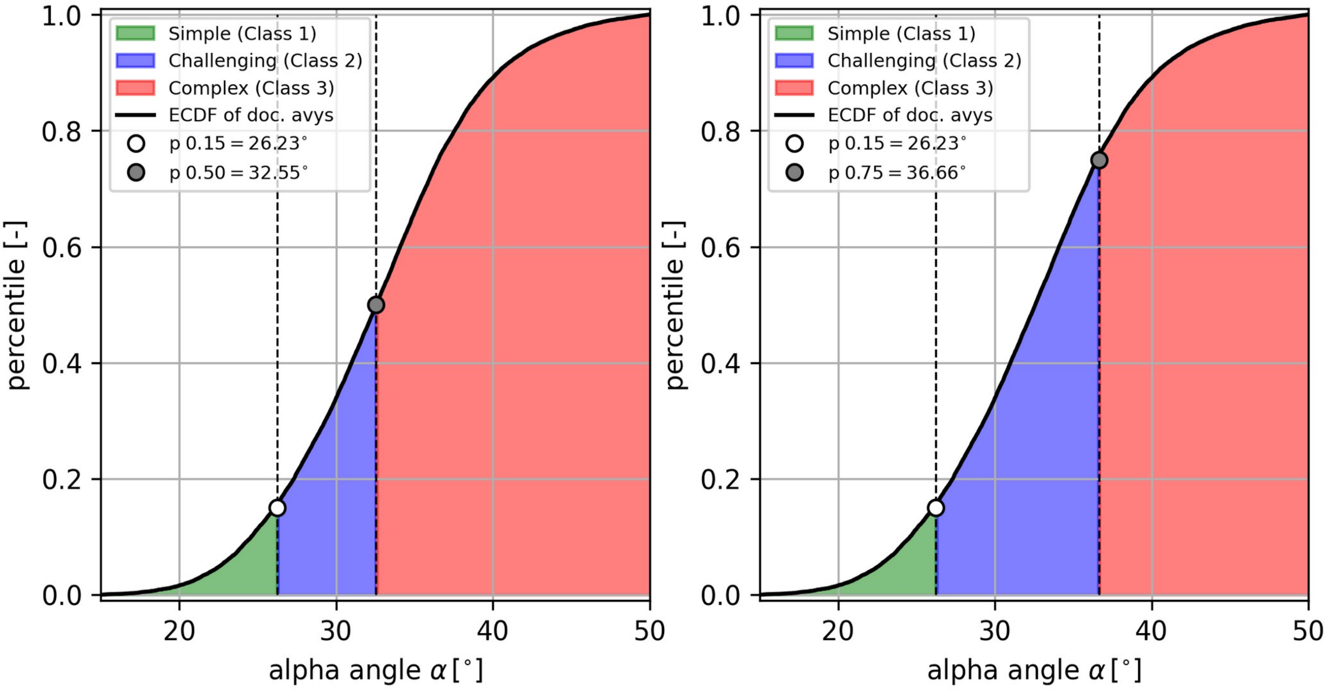

Figure 25: The ECDF (black) of CH SPOT6 Avalanche Reference Dataset (Toft et al., 2023), showing the 15th percentile (white point) and the 50th (left) and 75th (right) percentiles (gray point). The corresponding ATES classes (simple, challenging, complex) are indicated based on the percentile thresholds.

(3) Overhead hazard threshold

The overhead exposure parameter in the ATES classifier is derived from two Flow-Py outputs: the cell count and the z delta layer. The cell count represents the number of avalanche paths propagating through a raster cell (D'Amboise, Neuhauser, et al., 2022). In addition, the z delta layer represents the energy height or intensity of potential avalanches, which are associated with higher kinetic energies (D'Amboise, Neuhauser, et al., 2022) and, consequently, higher impact pressures. The cell count values are transformed using a logarithmic function and scaled to a percentage range. The z delta values are linearly scaled to match this percentage range. The scaled and normalized values of the cell count and z delta layers are added to calculate the overhead exposure parameter. This combination yields an overall measure of the level of overhead exposure in the terrain. A visual assessment of the layer reveals plausible results (Figure 29). However, a more in-depth investigation is required to evaluate the plausibility and integration into the ATES classification thoroughly. One prospective approach could incorporate routing flux information, as it can correlate with a theoretical mass assumption (D'Amboise, Teich, et al., 2022). Due to these uncertainties, the overhead exposure will be excluded from the primary ATES class delineation but will be added as an experimental additional layer in Section 4.3.2.

(4) **Forest threshold**

The PCC Forest Layer, which serves as a percentage of canopy cover, is derived and discussed in Section 4.1.2. and 4.3 of the PRA model and ATES classification. However, an issue arises when merging the avalanche mobility in the ATES classifier with the forestation. When an avalanche encounters a forested area, the ATES classifier lowers the classification based on the PCC Forest Layer density. If no forest is present, no reclassification occurs. This can lead to complex terrain classifications in valley bottoms but simple slopes classification above, which is not coherent, as shown in in the *Forest reclass detail* in Figure 26. To address this inconsistency, it becomes apparent that incorporating the mitigating effects of forests into the avalanche mobility model is crucial. As a temporary cartographic solution, areas below 1,500 m a.s.l. are disabled.

Moreover, a comprehensive evaluation of the forest density thresholds and the derivation of the PCC Forest Layer itself for the ATES classier is suggested as it is beyond the scope of this thesis. The parameterization for the ATES classifier, as presented in Table 19, follows Schumacher et al. (2022).

(5) **Isl size**

The smoothing step employs an isl size parameter set to 1,000 m², corresponding to the lower range of size 2 avalanches based on the Bühler et al. (2019) size classification in relation to the affected area. Furthermore, the small island size is interpreted as a means to account for the high diversity in the study area's mountainous topography.

A label function is incorporated to identify the islands in the raw ATES raster. To only detect connected pixels over the edges rather than edges and vertices, the connectivity of the label function (Fiorio & Gustedt, 1996; Wu et al., 2005) is set to 1. With this setting a smoother visual appearance is achieved.

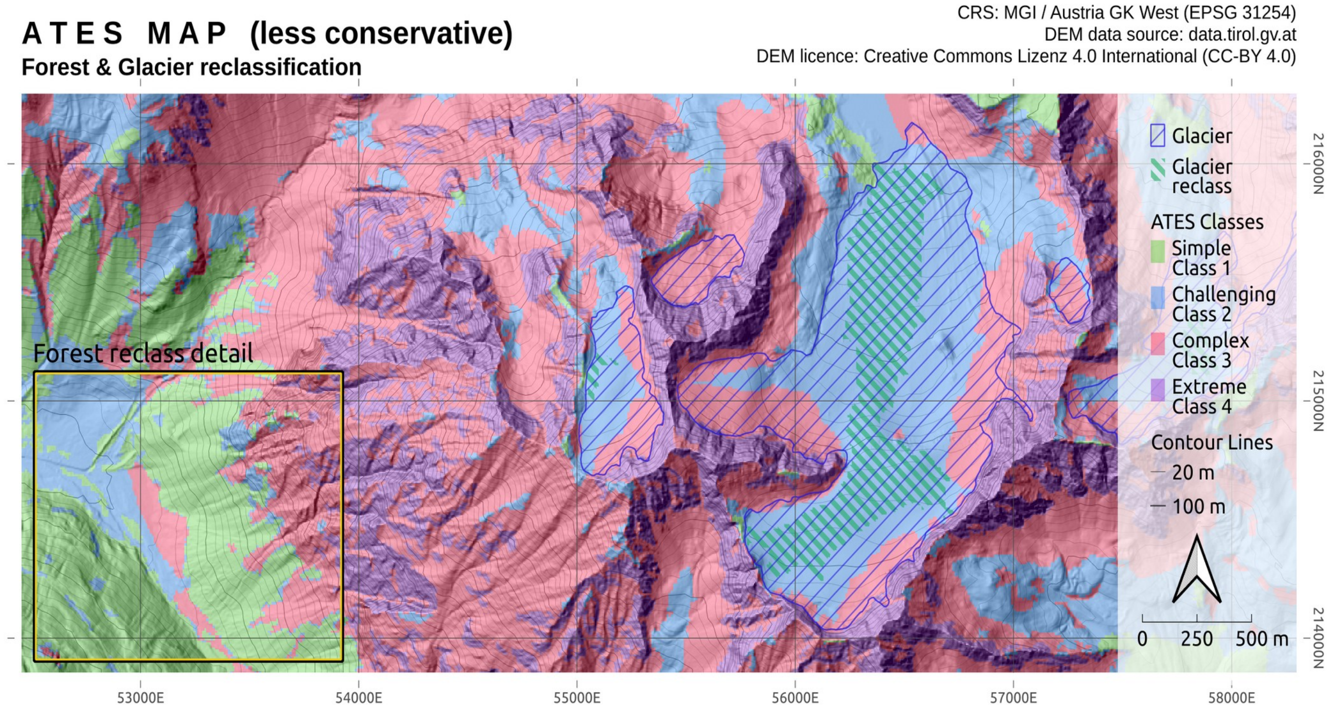

Figure 26: The map visually represents the less conservative alpha angle thresholds used for the ATES classification. The reclassification of forests (Forest reclass detail) highlights the challenges posed by reclassified avalanche paths in forested areas and non-reclassified avalanche runouts in areas lacking forestation. The Glacier Layer reclassification is showcased, showing glacier-covered areas at at least challenging terrain, along with the corresponding Glacier Layer and the reclassified simple terrain (Glacier reclass).

(6) Sliding window

The sliding window parameter is set to 1 to avoid smoothing for class 4. This ensures that class 4 is solely smoothed by the Isl size parameter, taking into account the study area's highly diverse and complex morphology, ensuring that even small areas covered by the extreme class are represented.

The parameterization of the ATES classifier is presented in Table 19.

Table 19: Parameterization of the ATES classifier applied on the study area

Input parameter	Class	Range	Parameter
Slope angle threshold	Simple (1) Challenging (2) Complex (3) Extreme (4)	≤ 28° > 28° & ≤ 39° > 39° & ≤ 45° > 45°	SAT12 = 28° SAT23 = 39° SAT34 = 45°
Alpha angle threshold (conservative)	Simple (1) **Challenging (2)** Complex (3)	≤ 26° **> 26° & ≤ 32°** > 32°	AAT12 = 26° **AAT23 = 32°**
Alpha angle threshold (less conservative)	Simple (1) **Challenging (2)** Complex (3)	≤ 26° **> 26° & ≤ 36°** > 32°	AAT12 = 26° **AAT23 = 36°**
Forest density threshold	Open Sparse Moderate Dense	≤ 10 > 10 & ≤ 25 > 25 & ≤ 65 > 65	TREE1 = 10 TREE2 = 25 TREE3 = 65
Isl size			ISLS = 1,000
Sliding window			WIN = 1

4.3.2 Discussion of the model chain results

The application and adaptation of the ATES classifier (Larsen et al., 2020; Schumacher et al., 2022) for size 3 avalanches in the study area is stated in Section 4.3 and discussed in the following. The derivation of the PRA layer is discussed in Section 4.1.3. The parameterization of the avalanche mobility model is discussed in Section 4.2.4. The workflow and the parameterization of the ATES classifier are described in Section 4.3.

In the following, the alpha angle thresholds, the integration of an additional Glacier Layer, and the overhead hazard are discussed.

The subsequent section discusses the conservative alpha angle threshold of 32° and the less conservative alpha angle threshold of 36° (as shown in Table 19) for delineating the boundary between challenging and complex terrain. Within both scenarios, the lower threshold remains consistent at 26°, serving as the alpha angle parameter for regional runout modeling using Flow-Py (D'Amboise, Neuhauser, et al., 2022). The area between the runout, determined by the two alpha angles, is considered challenging terrain, while terrain below this range is classified as simple terrain, and terrain above the range is classified as complex or extreme.

Regarding the analysis of large-scale avalanche data (CH SPOT6 Avalanche Reference Dataset, Section 3.2.3, the conservative thresholds (26° and 32°) align with the 15th and 50th percentiles of the ECDF (Figure 25). On the other hand, the less conservative thresholds (26° and 36°) correspond to the 15th and 75th percentiles. Table 20 summarizes of the runout reach likelihood for specific terrain classes.

The comparison between the conservative and less conservative scenarios demonstrates a difference in the percentage of area covered by the ATES classes due to the alpha angle thresholds shifting from 32° to 36°, especially the challenging and complex areal coverage is affected. The less conservative scenario covers 12.1% fewer complex areas but experiences a 12.6% increase in the challenging class and a 0.5% increase in the simple class, as depicted in Figure 27.

Given the pronounced variability of the high alpine geomorphology of the study area, especially considering narrow valleys and steep inhomogeneous slopes, the less conservative scenario leads to a more differentiated and balanced classification, given in the larger amount of the challenging terrain class, in total 28.3% on the study area. In contrast, the more conservative scenario leads to extensive complex terrain classification affecting 53% of the total area, where entire valleys and slopes are classified as complex, as shown in Figure 28.

Table 20: Correlation of the alpha angle thresholds for the ATES classification with the percentiles derived from ECDF of the CH SPOT6 Avalanche Reference Dataset (Toft et al., 2023)

ATES scenario	Class	Alpha angle	Percentile (ECDF)
Alpha angle threshold (conservative)	Simple (1)	≤ 26°	≤ 15th
	Challenging (2)	> 26° & ≤ 32°	> 15th & ≤ 50th
	Complex (3)	> 32°	> 50th
	Extreme (4)	-	-
Alpha angle threshold (less conservative)	Simple (1)	≤ 26°	≤ 15th
	Challenging (2)	> 26° & ≤ 36°	> 15th & ≤ 75th
	Complex (3)	> 32°	> 75th
	Extreme (4)	-	-

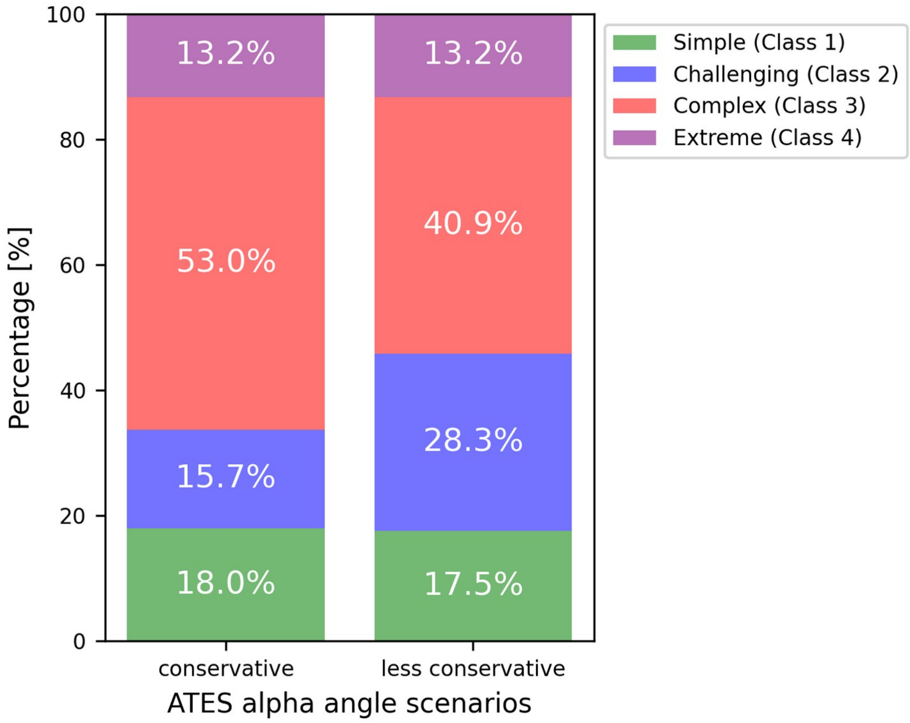

Figure 27: Comparison of the areal coverage of the conservative and less conservative alpha angle scenarios of the ATES classification, presented as percentages relative to the total study area

In the subsequent section, the conservative alpha angle threshold of 32° and the less conservative alpha angle threshold of 36° (as shown in Table 19 and 20) are discussed in the context of the AUT SPOT6 Avalanche Reference Dataset. The discussion involves a qualitative assessment by overlaying over 500 mapped avalanche runouts based on satellite imagery. The imagery was derived after an avalanche cycle in February 2023 (Section 3.2.3). The dataset includes an expert size estimation in the scope of travel length based on the EAWS (2023) classification scheme. It is important to note that due to the recent completion of this mapping, the data could not be included in earlier assessments for the PRA and avalanche mobility models. However, this data opens up possibilities for enhancing the parameterizations of the individual model chain components.

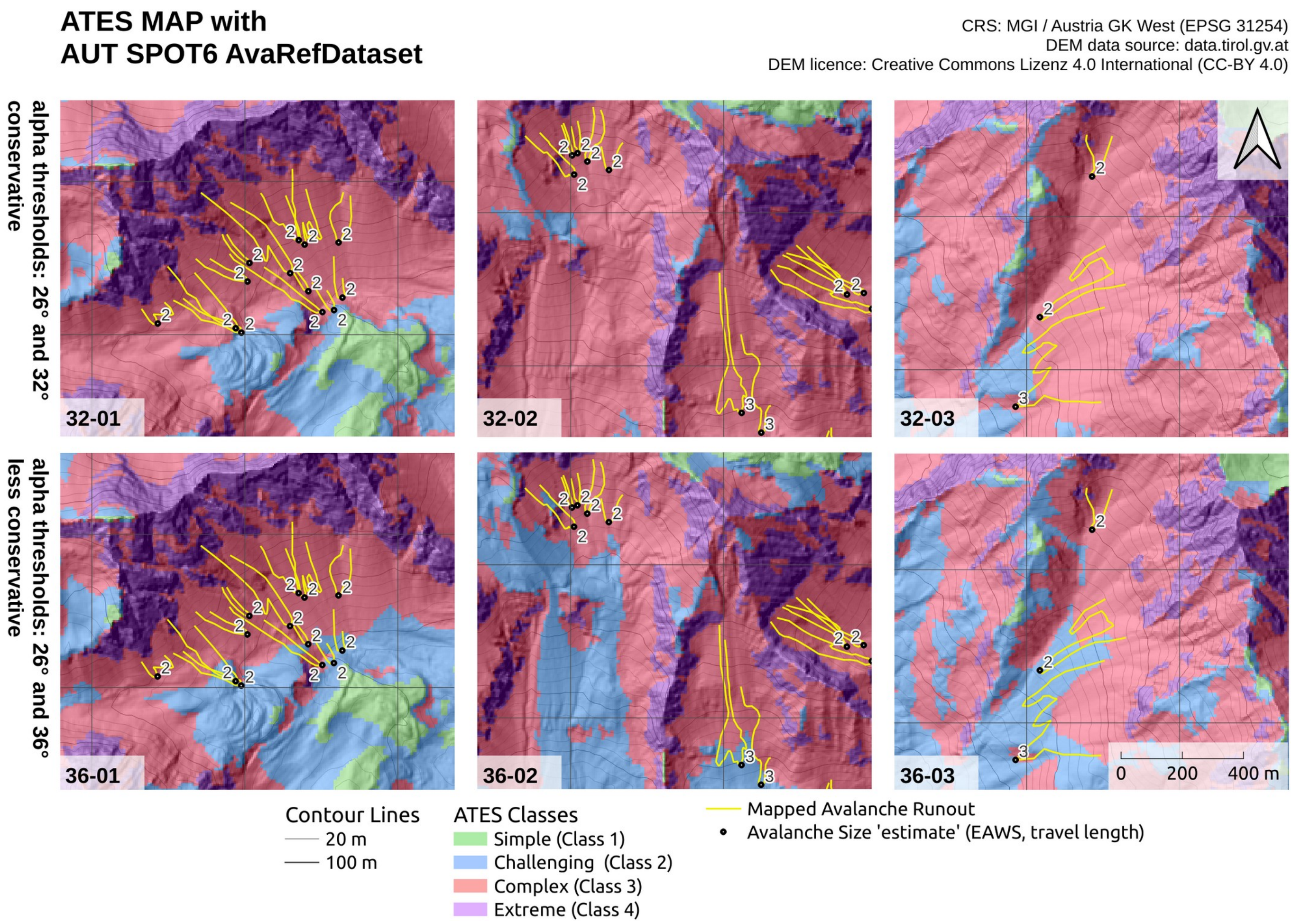

Figure 28: The provided visual exemplifies the comparison between conservative (32-01, 32-02, and 32-03) and less conservative (36-01, 36-02, and 36-03) alpha angle scenarios within the ATES classification. It also includes mapped avalanche runouts from the AUT SPOT6 Avalanche Reference Dataset, along with their corresponding size classification determined based on the EAWS travel length.

Figure 28 presents three representative comparison sets: The conservative scenario is depicted in sub-figures 32-01, 32-02, and 32-03, while the less conservative scenario is illustrated in sub-figures 36-01, 36-02, and 36-03. Upon qualitative assessment, it becomes evident that nearly all size 2 and 3 avalanches are encompassed within the extensively covered complex areas (sub-figure sets 01, 02, and 03). However, the less conservative scenario reveals that avalanches of size 2 are predominantly situated within the complex class or at least near the boundary of the complex-challenging class (sub-figure sets 01 and 02). Moreover, size 3 avalanches are observed to reach the challenging class in the less conservative scenario (sub-figure sets 02 and 03).

The correlation between the mapped avalanche runouts and size estimation further enhances the aforementioned differentiated and balanced classifications. This enhancement stems from the recognition that a substantial proportion of size 2 avalanches align with the complex class, while size 3 avalanches extend into the challenging class. For this reason, the less conservative scenario is interpreted as more reasonable. Figure 30 shows the less conservative scenario applied on the total study area. However, since avalanches are a very dynamic phenomena that are difficult to define in static classes, as underscored by this study, there will be scenarios where the conservative scenario is more realistic regarding the prevailing avalanche problem or danger level.

Within the study area, approximately 5% (34.3 km^2) of the total land area is covered by glaciers (Buckel & Otto, 2018). Despite the occurrence of low slope angles, these areas would potential delineated as simple terrain class. However, glaciers are excluded from the simple terrain class as defined by Statham et al. (2006). Therefore, it is imperative that glaciers in the simple terrain are also excluded in the ATES classification of the study area. The ATES classifier is modified to designate glaciated areas at least as challenging terrain (Figure 23). Nevertheless, the dataset is not up to date; it represents the latest available data. In addition to that, the Glacier Layer does not cover crevasses. However, it is deemed valuable for its inclusion in the ATES classification. This is particularly important since the presence of a simple terrain class on a glacier might lead to misinterpretations.

The overhead hazard layer yields an overall measure of the level of exposure in the terrain. A visual assessment of the layer reveals plausible results (Figure 29). However, a more in-depth investigation is required to thoroughly evaluate the plausibility and integration into the ATES classification. One prospective approach could incorporate routing flux information, as it can correlate with a mass assumption (D'Amboise, Teich, et al., 2022). This information could pertain to the intensity of avalanche burial. Combined with z delta, which indicates avalanche impact intensity, the alpha angle offers insight into the frequency, which could be additional information to the ATES classification.

Given these uncertainties, the overhead exposure is omitted from the primary ATES class delineation. However, it can be implemented as additional continuous raster information to further enhance the challenging and complex classes. The overhead hazard range spans from low to high, depicted in shades of blue for the challenging class and shades of red for the complex class. The layer information low corresponds to the ATES class definition as stated in Figure 23. The indication of a high overhead hazard indicates higher values calculated for the overhead hazard and serves as additional information for the challenging or the complex class. This novel approach goes beyond the original ATES concept of desecrated classes.

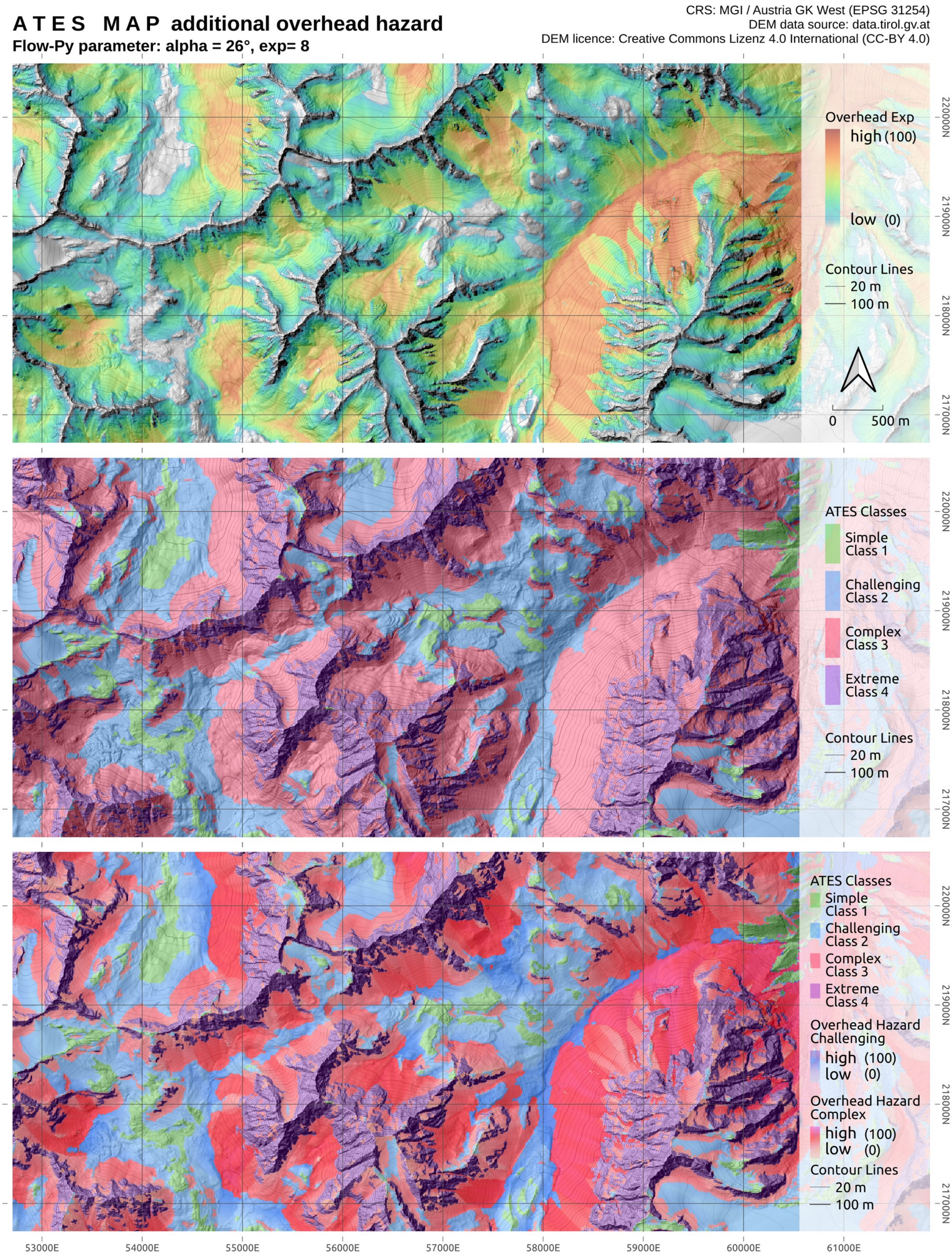

Figure 29: The first map visualizes the calculated overhead hazard, ranging from low to high. The second map represents the less conservative alpha angle thresholds used for the ATES classification. The third map, despite the overhead hazard as an overlay for the ATES classes challenging and complex.

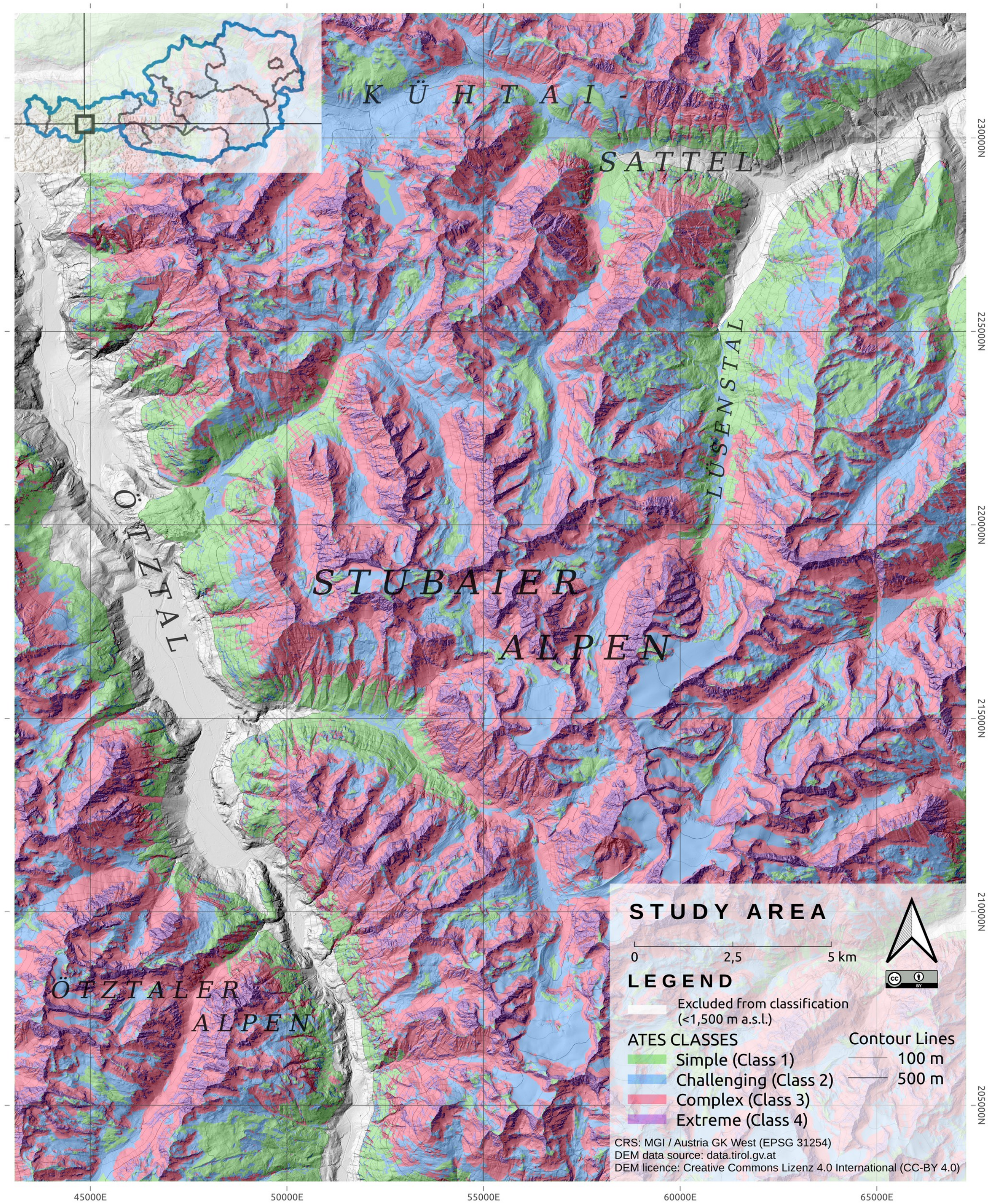

Figure 30: Final ATES map produced with the less conservative alpha angle thresholds for the ATES classifier. Areas situated below 1,500 m a.s.l. are devoid of ATES classification.

4.3.3 Alternative avalanche terrain classification approaches

ATES terrain classification is just one of the applications of the model chain data. The results can be merged to generate alternative cartographic outputs depending on the specific context and requirements. Similar to the methodology used by Harvey et al. (2018), specific focus maps can be developed by integrating various parameters, such as PRAs associated with alpha angles or the travel length of modeled avalanches. For example, Figure 31 demonstrates the combination of PRAs and alpha angles of modeled avalanches. Regarding the ECDF analysis, the map can also help assess the likelihood of areas being affected by avalanches of different sizes.

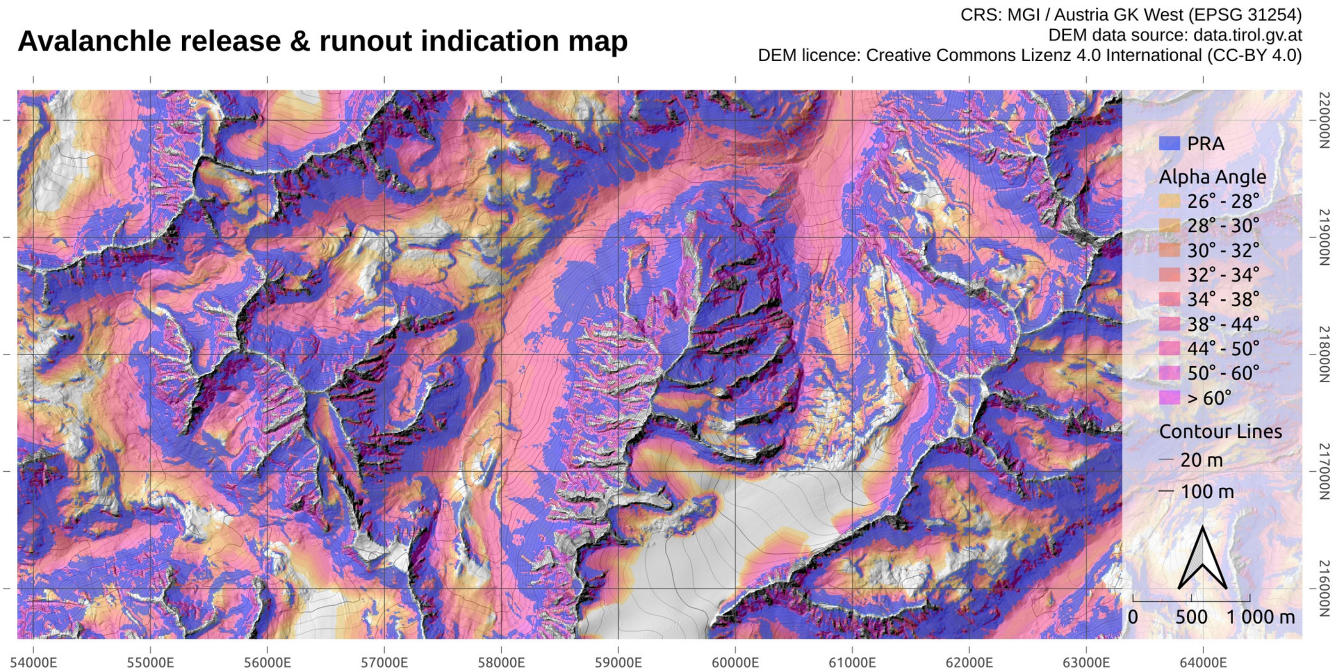

Figure 31: Avalanche release and runout indication map, displaying the PRA model results and the avalanche mobility results as runout angles.

5 Conclusion and outlook

The classification and delineation of avalanche-prone terrain is a valuable safety tool for individuals and organizations. It facilitates efficient communication, planning, and execution of recreational or professional activities in alpine environments (McClung & Schaerer, 2006). Over the past two decades, several classification schemes and resulting map products have been published. The focus of these maps is the classification of avalanche terrain to improve and contribute to more safe navigation in the backcountry (Campbell & Gould, 2013; Harvey et al., 2018; Larsen et al., 2020; Schmudlach & Köhler, 2016; Schumacher et al., 2022; Statham et al., 2006). However, these products are either unavailable for Austria (Harvey et al., 2018; Larsen et al., 2020; Schumacher et al., 2022) or their workflow, or certain components made off, are not openly accessible (Harvey et al., 2018; Schmudlach & Köhler, 2016). The limitation of accessibility hinders the thorough application and investigation of these products for Austria. Therefore, the open-source approach developed by Larsen et al. (2020) has been assessed and applied to a study area in Austria in this study. The model chain encompasses three sequential steps, each progressively building upon the preceding one. Each model step has been subjected to individual testing and discussion in alignment with its respective sub-objectives. The discussed model chain steps involve and reveal the following:

(1) **PRA delineation**

The sub-objective for the PRA delineation is the parameterization of the PRA model (Sharp, 2018; Sykes et al., 2022; Veitinger et al., 2016) to realistically delineate PRAs in the study area (Section 4.1).

The study compared three PRA models against the CH ORA Dataset and determined that the binary-rugg and no-rugg models outperform the fuzzy-rugg model, utilizing statistical skill scores (HSS and TSS). The application of both the no-rugg and binary-rugg models to the study area reveal two key insights:

Firstly, when applied to the study area, it highlights the potential advantages of incorporating a PCC Forest Layer; however, a more comprehensive analysis is suggested. The derivation of this layer from the 1m DTM and 1m DSM is based on the assumption that differences greater than 5 m between the two layers indicate the presence of forests. However, this approach may not accurately reflect current conditions, as it captures only a specific moment of exploration data. Since forests undergo dynamic changes over time, this method may only partially capture their variability. Additionally, it is worth mentioning that this derivation does not account for distinctions between forest type, such as deciduous and evergreen trees.

Secondly, incorporating a binary ruggedness mask is considered plausible, as it excludes rugged terrain features that are less susceptible to avalanche release.

As a result, the binary-rugg model with the PCC Forest Layer is selected for integration into the model chain. A PRA a threshold of 0.3 is determined to represent a well-balanced choice, given the inability to identify a discrete threshold. The total area of delineated PRAs covers 33.31% of the study area.

(2) **Avalanche mobility model**

The assessment of the data-based avalanche mobility model Flow-Py (D'Amboise, Neuhauser, et al., 2022) for regional runout modeling size 3 avalanches for the ATES terrain classification has been conducted in Section 4.2.

In summary, the assessment of back-calculated avalanches from the AUT AWS Reference Dataset highlights the impact of slope morphologies on Flow-Py results. An exponent value of 8 provides a balanced outcome for various slope forms. The selection of the alpha angle for the model chain is anchored at 26°. This choice corresponds to a very low RMSE, encompassing 57% of modeled avalanches within the size 3 classification range for travel length, and is consistent with the mean alpha angle of the AUT AWS avalanche reference data.

Valuable improvements could arise from identifying avalanche paths within Flow-Py simulations. This path identification could facilitate the subsequent segmentation of PRAs, which, once refined, might serve as input for process-based simulation tools rather than the data-based Flow-Py model. Furthermore, the identification of avalanche paths paves the way for the implementation of an alpha-beta model. Introducing an alpha-beta model has the potential to enhance the reliability of simulation outcomes across various slope shapes. As this model includes an additional topographical parameter, the beta angle, which is recognized for its increased correlation in predicting avalanche runout (Lied & Bakkehøi, 1980; Toft et al., 2023).

A consistent pattern emerges in the comparison between modeled affected area and impact pressure: overestimations in impact pressure and affected area counts are roughly double those in travel length counts across varying alpha angles. These discrepancies can be attributed to several limitations:

The challenges in selecting size 3 avalanches involve determining their release size and deriving volume by multiplying an average release height to align with the EAWS size range. Additionally, this selection approach overlooks potential entrainment processes.

Compared to travel length, a persistent trend of overestimation in impact pressure is observed. This could relate to the calculation of impact pressure. The calculation of the impact pressure is based on the velocity. The velocity is derived from the kinetic energy height (z delta) after Körner (1980). The frictional dissipation is determined by geometric relations of the alpha angle concept (Heim, 1932; Lied & Bakkehøi, 1980) based on the law of conservation of energy and Coulomb friction of a block movement. This friction term can also be replaced or enhanced by other friction models, for instance, the Voellmy friction (Voellmy, 1955). *F*urthermore, an assumed density of 200 kg m^{-3} has been applied for calculating the impact pressure, which correlates to the average release density for slab avalanches (McClung & Schaerer, 2006). This could deviate from actual circumstances. Moreover, the current size classification for impact pressure considers the 99th percentile across the entire avalanche path, while an alternative method could involve relative assessment at specific sections like the runout zone, as it is common for general avalanche hazard mapping for settlements and infrastructural facilities (Rudolf-Miklau & Sauermoser, 2011).

In conclusion, determining a suitable parameterization for the Flow-Py avalanche mobility model to fit avalanche size 3 is a challenge that is not straightforward. By evaluating three OA, a conservative alpha angle of 26° is determined. This alpha angle serves a dual purpose: as a parameterization for the Flow-Py model within the model chain and a threshold for distinguishing between simple and challenging terrain. Furthermore, the assessment highlighted the complexity of classifying avalanches into size classes. The same modeled avalanche could fall into several size classes based on different factors such as travel length, impact pressure, and affected area.

(3) **ATES classification**

The objective for the last model chain step, the ATES classifier (Larsen et al., 2020; Schumacher et al., 2022), is the application and adaptation for size 3 avalanches in the study area (Section 4.3). The ATES classifier is the last step of the model chain. It incorporates the results of the PRA model (Veitinger et al., 2016) and the avalanche mobility model, Flow-Py (D'Amboise, Neuhauser, et al., 2022). In addition, the PCC Forest Layer, derived in Section 4.1.2, and a Glacier Layer, derived in Section 3.3 have been incorporated into the ATES terrain classification.

The PCC Forest Layer (percentage per canopy cover) is based on the approach presented by Schumacher et al. (2022). The derivation of this layer from the 1m DTM and 1m DSM is based on an assumption and may not accurately reflect current conditions, as mentioned above. Regarding the ATES classification, the inclusion of forests in the ATES classification highlights the necessity to integrate forests into the avalanche mobility model. The mitigating effects of forests on slopes or runouts below forests are not considered and, therefore, not reclassified, which is inconsistent.

In the study area, around 5% (34.3 km^2) is glacier-covered. Due to their prevailing gentle slopes, glaciers are often classified as simple terrain. However, glaciers are excluded from the simple terrain class, as per Statham et al. (2006). To avoid misinterpretations, the ATES classifier designates glacier-covered areas as at least challenging terrain. Although the Glacier Layer lacks crevasse data and uses slightly dated information from 2015 (Buckel & Otto, 2018), it is still valuable for ATES classification.

The overhead hazard layer shows plausible results in its first visual assessment but requires further investigation for integration into the ATES classification. The potential inclusion of the layer as experimental continuous raster data could provide valuable insights into the challenging and complex classes. For further investigation, the routing flux could be considered instead of cell count, as it can be correlated to a mass assumption (D'Amboise, Teich, et al., 2022). This information could pertain to the intensity of avalanche burial. Combined with z delta, which indicates avalanche impact intensity, the alpha angle offers insight into the frequency, which could be additional information to the ATES classification.

Addressing the challenge of setting alpha angle thresholds for the ATES classifier, an analysis of over 18,000 avalanches from the CH SPOT6 Avalanche Reference Dataset has been conducted, concerning previous findings of the avalanche mobility model. The dataset reveals a weak correlation between the alpha angle and avalanche size. This led to an enlarged interpretation of the alpha angle thresholds for the ATES classifier, utilizing the empirical cumulative distribution function (ECDF). In correlation with the findings of the assessment of the avalanche mobility model, more conservative and less conservative alpha angle thresholds were determined. The 15th percentile of the ECDF aligns with approximately 26° and the 50th percentile with around 32°. The less conservative alpha angle of 36° aligns with the 75th percentile. These percentiles aid in the interpretation of the thresholds for the ATES classification. The two alpha angle thresholds establish the range for the challenging terrain class. The area between the runout, determined by the two alpha angles, is considered challenging terrain, while terrain below this range is classified as simple terrain, and terrain above the range is classified as complex or extreme.

The qualitative comparison between the conservative and less conservative scenario highlights notable differences in the area distribution of ATES classes due to the modification of the alpha angle thresholds. Using the less conservative approach results in a more differentiated and balanced classification that is particularly valuable when dealing with the pronounced variability of the inhomogeneous high alpine geomorphology of the study area. The less conservative scenario expands the representation of challenging terrain while limiting the complex areas. The comparison of mapped avalanche runout and size estimates (AUT SPOT6 Avalanche Reference Dataset) emphasizes this differentiated and balanced classification and demonstrates the suitability of the less conservative approach. Although the less conservative scenario proves more reasonable overall, the dynamic nature of avalanches underscores that both scenarios have their place in addressing varying avalanche problems and danger levels.

In addition, the applied model chain illustrates the versatility of the resulting data. Similar to the methodology used by Harvey et al. (2018), specific focus maps can be developed by integrating various parameters, such as PRAs associated with alpha angles or the travel length of modeled avalanches.

In conclusion, the application and testing of the autoATES terrain classification to a study area in Austria are successfully demonstrated. The individual sub-steps of the model chain yield plausible outcomes yet highlight certain aspects that warrant further discussion or suggest the potential for additional research for improvement. Furthermore, it is essential to emphasize that ATES terrain maps, despite their static nature, are confronted with a profoundly dynamic phenomenon - avalanches, which present challenges in precise spatial and temporal classification. Future enhancements could include dynamic mapping that considers prevailing avalanche problems or the avalanche danger level to further improve terrain classification and compensate the dynamic nature of avalanches.

6 References

AAA. (2016). *Snow, weather, and avalanches: Observation guidelines for avalanche programs in the United States*. American Avalanche Association.

AAA. (2023). *Avalanche Terrain Exposure Scale (ATES)*. American Avalanche Association (Avalanche.Org). https://avalanche.org/avalanche-encyclopedia/terrain/avalanche-terrain-exposure/avalanche-terrain-exposure-scale-ates/ (Accessed: 25 July 2023).

Allouche, O., Tsoar, A., & Kadmon, R. (2006). Assessing the accuracy of species distribution models: Prevalence, kappa and the true skill statistic (TSS): Assessing the accuracy of distribution models. *Journal of Applied Ecology*, *43*(6), 1223–1232. https://doi.org/10.1111/j.1365-2664.2006.01214.x

Bartelt, P., Bühler, Y., Buser, O., Christen, M., & Meier, L. (2012). Modeling mass-dependent flow regime transitions to predict the stopping and depositional behavior of snow avalanches: SNOW AVALANCHE FLOW REGIME TRANSITIONS. *Journal of Geophysical Research: Earth Surface*, *117*(F1). https://doi.org/10.1029/2010JF001957

Bartelt, P., Buser, O., Vera Valero, C., & Bühler, Y. (2016). Configurational energy and the formation of mixed flowing/powder snow and ice avalanches. *Annals of Glaciology*, *57*(71), 179–188. https://doi.org/10.3189/2016AoG71A464

Bebi, P., Kienast, F., & Schönenberger, W. (2001). Assessing structures in mountain forests as a basis for investigating the forests' dynamics and protective function. *Forest Ecology and Management*, *145*(1–2), 3–14. https://doi.org/10.1016/S0378-1127(00)00570-3

BEV. (2023). *Strukturinformation*. Bundesamit für Eich- und Vermessungswesen (bev.gv.at). https://www.bev.gv.at/Services/Produkte/Digitales-Gelaendehoehenmodell/Strukturinformation.html (Accessed: 25 July 2023).

Blaschke, T. (2010). Object based image analysis for remote sensing. *ISPRS Journal of Photogrammetry and Remote Sensing*, *65*(1), 2–16. https://doi.org/10.1016/j.isprsjprs.2009.06.004

Breidenbach, J., Granhus, A., Hylen, G., Eriksen, R., & Astrup, R. (2020). A century of National Forest Inventory in Norway – informing past, present, and future decisions. *Forest Ecosystems*, *7*(1), 46. https://doi.org/10.1186/s40663-020-00261-0

Buckel, J., & Otto, J.-C. (2018). *The Austrian Glacier Inventory GI 4 (2015) in ArcGis (shapefile) format* (p. 4 MBytes) [Application/zip]. PANGAEA. https://doi.org/10.1594/PANGAEA.887415

Bühler, Y., Hafner, E. D., Zweifel, B., Zesiger, M., & Heisig, H. (2019). Where are the avalanches? Rapid SPOT6 satellite data acquisition to map an extreme avalanche period over the Swiss Alps. *The Cryosphere*, *13*(12), 3225–3238. https://doi.org/10.5194/tc-13-3225-2019

Bühler, Y., Kumar, S., Veitinger, J., Christen, M., Stoffel, A., & Snehmani. (2013). Automated identification of potential snow avalanche release areas based on digital elevation models. *Natural Hazards and Earth System Sciences*, *13*(5), 1321–1335. https://doi.org/10.5194/nhess-13-1321-2013

Bühler, Y., & von Rickenbach, D. (2018). *Automated Avalanche Release Area (PRA) Delineation Davos* (1.0) [SHP,.tif]. EnviDat. https://doi.org/10.16904/ENVIDAT.55

Bühler, Y., von Rickenbach, D., Christen, M., Margreth, S., Stoffel, L., Stoffel, A., & Kühne, R. (2018). Linking modelled potential release areas with avalanche dynamic simulations: An automated approach for efficient avalanche hazard indication mapping. *Proceedings of the International Snow Science Workshop, Innsbruck, Tyrol, Austria.*

Bühler, Y., von Rickenbach, D., Stoffel, A., Margreth, S., Stoffel, L., & Christen, M. (2018). Automated snow avalanche release area delineation – validation of existing algorithms and proposition of a new object-based approach for large-scale hazard indication mapping. *Natural Hazards and Earth System Sciences*, *18*(12), 3235–3251. https://doi.org/10.5194/nhess-18-3235-2018

CAA. (2016). *Observation guidelines and recording standards for weather , snowpack and avalanches.* Canadian Avalanche Association.

Campbell, C., & Gould, B. (2013). A proposed practical model for zoning with the Avalanche Terrain Exposure Scale. *Proceedings of the International Snow Science Workshop, Grenoble–Chamonix Mont-Blanc, France*, 385–391.

Christen, M., Bartelt, P., & Kowalski, J. (2010). Back calculation of the In den Arelen avalanche with RAMMS: interpretation of model results. *Annals of Glaciology*, *51*(54), 161–168. https://doi.org/10.3189/172756410791386553

Christen, M., Kowalski, J., & Bartelt, P. (2010). RAMMS: Numerical simulation of dense snow avalanches in three-dimensional terrain. *Cold Regions Science and Technology*, *63*(1–2), 1–14. https://doi.org/10.1016/j.coldregions.2010.04.005

Congalton, R. G., & Green, K. (1999). Assessing the Accuracy of Remotely Sensed Data: Principles and Practices. *Lewis Publishers, New York.*

D'Amboise, C. J. L., Neuhauser, M., Teich, M., Huber, A., Kofler, A., Perzl, F., Fromm, R., Kleemayr, K., & Fischer, J.-T. (2022). Flow-Py v1.0: A customizable, open-source simulation tool to estimate runout and intensity of gravitational mass flows. *Geoscientific Model Development*, *15*(6), 2423–2439. https://doi.org/10.5194/gmd-15-2423-2022

D'Amboise, C., Teich, M., Hormes, A., Steger, S., & Berger, F. (2022). Modeling Protective Forests for Gravitational Natural Hazards and How It Relates to Risk-Based Decision Support Tools. In M. Teich, C. Accastello, F. Perzl, & K. Kleemayr (Eds.), *Protective Forests as Ecosystem-based Solution for Disaster Risk Reduction (Eco-DRR).* IntechOpen. https://doi.org/10.5772/intechopen.99510

Delparte, D. M. (2008). *Avalanche terrain modeling in Glacier National Park, Canada*. xvi, 179 leaves : ill.; 30 cm. https://doi.org/10.11575/PRISM/1858

EAWS. (2023). *Glossary.* European Avalanche Warning Services (Avalanches.Org). https://www.avalanches.org/glossary/ (Accessed: 25 July 2023).

Fielding, A. H., & Bell, J. F. (1997). A review of methods for the assessment of prediction errors in conservation presence/absence models. *Environmental Conservation*, *24*(1), 38–49. https://doi.org/10.1017/S0376892997000088

Fiorio, C., & Gustedt, J. (1996). Two linear time union-find strategies for image processing. *Theoretical Computer Science*, *154*(2), 165–181.

Gauer, P. (2001). Numerical modeling of blowing and drifting snow in Alpine terrain. *Journal of Glaciology*, *47*(156), 97–110. https://doi.org/10.3189/172756501781832476

Ghinoi, A., & Chung, C.-J. (2005). STARTER: A statistical GIS-based model for the prediction of snow avalanche susceptibility using terrain features—application to Alta Val Badia, Italian Dolomites. *Geomorphology*, *66*(1–4), 305–325. https://doi.org/10.1016/j.geomorph.2004.09.018

Gruber, U., Bartelt, P., & Margreth, S. (1999). Anleitung zur Berechnung von Fließlawinen: Neue Berechnungsmethoden in der Lawinengefahrenkartierung. *WSL Institut Für Schnee-Und Lawinenforschung SLF, Davos*, *15*.

Harbitz, C. B., Issler, D., & Keylock, C. J. (1998). Conclusions from a recent survey of avalanche computational models. *Proceedings of the Anniversary Conference*, *25*, 128–135.

Harvey, S., Schmudlach, G., Bühler, Y., Dürr, L., Stoffel, A., & Christen, M. (2018). Avalanche terrain maps for backcountry skiing in Switzerland. *Proceedings of the International Snow Science Workshop, Innsbruck, Tyrol, Austria.*

Heim, A. (1932). Bergsturz und Menschenleben. *Beiblatt Zur Vierteljahrsschrift Der Naturforschenden Gesellschaft in Zürich, Fretz & Wasmuth.*

Jang, J.-S. R., Sun, C.-T., & Mizutani, E. (1997). Neuro-fuzzy and soft computing-a computational approach to learning and machine intelligence [Book Review]. *IEEE Transactions on Automatic Control*, *42*(10), 1482–1484.

Körner, H. (1980). The energy-line method in the mechanics of avalanches. *Journal of Glaciology*, *26*(94), 501–505.

Larsen, H. T., Hendrikx, J., Slåtten, M. S., & Engeset, R. V. (2020). Developing nationwide avalanche terrain maps for Norway. *Natural Hazards*, *103*(3), 2829–2847. https://doi.org/10.1007/s11069-020-04104-7

Lied, K., & Bakkehøi, K. (1980). Empirical calculations of snow–avalanche run–out distance based on topographic parameters. *Journal of Glaciology*, *26*(94), 165–177.

Lied, K., Weiler, C., Bakkehoi, S., & Hopf, J. (1995). Calculation methods for avalanche run-out distance for the Austrian Alps. *Les Apports de La Recherche Scientifique à La Sécurité Neige Glace et Avalanche*.

Maggioni, M. (2005). *Avalanche release areas and their influence on uncertainty in avalanche hazard mapping* [PhD Thesis]. Universität Zürich.

Maggioni, M., & Gruber, U. (2003). The influence of topographic parameters on avalanche release dimension and frequency. *Cold Regions Science and Technology*, *37*(3), 407–419. https://doi.org/10.1016/S0165-232X(03)00080-6

Maggioni, M., Gruber, U., & Stoffel, A. (2002). Definition and characterisation of potential avalanche release areas. *Proceedings of the ESRI Conference, San Diego*, 13.

McClung, D. (2001). Characteristics of terrain, snow supply and forest cover for avalanche initiation caused by logging. *Annals of Glaciology*, *32*, 223–229.

McClung, D., & Schaerer, P. A. (2006). *The avalanche handbook* (3rd ed). Mountaineers Books.

McClung, & Schaerer. (1980). Snow avalanche size classification. *Proceedings of the International Snow Science Workshop, Vancouver, British Columbia*, *3*(5).

Mitterer, C., & Schweizer, J. (2013). Analysis of the snow-atmosphere energy balance during wet-snow instabilities and implications for avalanche prediction. *The Cryosphere*, *7*(1), 205–216. https://doi.org/10.5194/tc-7-205-2013

Munter, W. (1997). 3x3 Lawinen: Entscheiden in kritischen Situationen Agentur Pohl & Schellhammer. *Garmisch Patenkirchen, Germany*.

Nairz, P., Sauermoser, S., Kleemayer, K., Gabl, K., Stoffel, M., & Margreth, S. (2011). Lawinen: Entstehung und Wirkung. In *Handbuch Technischer Lawinenschutz* (pp. 21–62). Wiley Online Library.

Neuhauser, M., D'Amboise, C., Teich, M., Kofler, A., Huber, A., Fromm, R., & Fischer, J. T. (2021). *Flow-Py: Routing and stopping of gravitational mass flows* (1.0) [Computer software]. Zenodo. https://doi.org/10.5281/ZENODO.5027275

Nuñez, J. R., Anderton, C. R., & Renslow, R. S. (2018). Optimizing colormaps with consideration for color vision deficiency to enable accurate interpretation of scientific data. *PLOS ONE*, *13*(7), e0199239. https://doi.org/10.1371/journal.pone.0199239

Oesterle, F., Tonnel, M., Wirbel, A., & Fischer, J.-T. (2022). *avaframe/AvaFrame: Version 1.3* (1.3) [Computer software]. Zenodo. https://doi.org/10.5281/ZENODO.7189007

Olaya, V. (2005). *Tool Aggregate / SAGA-GIS Tool Library Documentation (v6.3.0)*. https://saga-gis.sourceforge.io/saga_tool_doc/6.3.0/grid_tools_1.html (Accessed: 25 July 2023).

Perla, R. I., & Martinelli, M. (1976). *Avalanche handbook*. US Department of Agriculture, Forest Service.

Pistocchi, A., & Notarnicola, C. (2013). Data-driven mapping of avalanche release areas: A case study in South Tyrol, Italy. *Natural Hazards*, *65*(3), 1313–1330. https://doi.org/10.1007/s11069-012-0410-3

Plattner, C., Braun, L., & Brenning, A. (2004). Spatial variability of snow accumulation on Vernagtferner, Austrian Alps, in winter 2003/2004. *Zeitschrift Für Gletscherkunde Und Glazialgeologie*, *39*(1), 43–57.

Rossum, G. van, & Drake, F. L. (2010). *The Python language reference* (Release 3.0.1 [Repr.]). Python Software Foundation.

Rudolf-Miklau, F., & Sauermoser, S. (Eds.). (2011). *Handbuch technischer Lawinenschutz* (1. Auflage). Ernst & Sohn.

Salm, B., Burkard, A., & Gubler, H. (1990). *Berechnung von Fliesslawinen: Eine Anleitung für Praktiker mit Beispielen*. Eidgenössisches Institut für Schnee-und Lawinenforschung, Weissfluhjoch/Davos.

Sampl, P., & Zwinger, T. (2004). Avalanche simulation with SAMOS. *Annals of Glaciology*, *38*, 393–398.

Sappington, J. M., Longshore, K. M., & Thompson, D. B. (2007). Quantifying landscape ruggedness for animal habitat analysis: A case study using bighorn sheep in the Mojave Desert. *The Journal of Wildlife Management*, *71*(5), 1419–1426.

Sauermoser, S., Granig, M., Kleemayr, K., & Margreth, S. (2011). Grundlagen und Modelle der Lawinendynamik und Lawinenwirkung. *Handbuch Technischer Lawinenschutz*, 63–101.

Sauermoser, S., Granig, M., Kleemayr, K., & Margreth, S. (2014). Avalanche dynamics: Models and impact. In F. Rudolf-Miklau, S. Sauermoser, & A. I. Mears (Eds.), *The Technical Avalanche*

Protection Handbook (pp. 55–90). Wilhelm Ernst & Sohn, Verlag für Architektur und technische Wissenschaften GmbH & Co. KG. https://doi.org/10.1002/9783433603840.ch03

Schmudlach, G., & Köhler, J. (2016). Method for an automatized avalanche terrain classification. *Proceedings of the International Snow Science Workshop, Breckenridge, CO, USA*.

Schmudlach, G., Winkler, K., & Köhler, J. (2018). Quantitative risk reduction method (QRM), a data-driven avalanche risk estimator. *Proceedings of the International Snow Science Workshop, Innsbruck, Tyrol, Austria*, 1272–1278.

Schumacher, J., Toft, H., McLean, J. P., Hauglin, M., Astrup, R., & Breidenbach, J. (2022). The utility of forest attribute maps for automated Avalanche Terrain Exposure Scale (ATES) modelling. *Scandinavian Journal of Forest Research*, *37*(4), 264–275. https://doi.org/10.1080/02827581.2022.2096921

Schweizer, J. (1999). Review of dry snow slab avalanche release. *Cold Regions Science and Technology*, *30*(1–3), 43–57. https://doi.org/10.1016/S0165-232X(99)00025-7

Schweizer, J., Bartelt, P., & van Herwijnen, A. (2015). Snow Avalanches. In *Snow and Ice-Related Hazards, Risks, and Disasters* (pp. 395–436). Elsevier. https://doi.org/10.1016/B978-0-12-394849-6.00012-3

Schweizer, J., Bruce Jamieson, J., & Schneebeli, M. (2003). Snow avalanche formation: AVALANCHE FORMATION. *Reviews of Geophysics*, *41*(4). https://doi.org/10.1029/2002RG000123

Schweizer, J., & Jamieson, J. (2001). Snow cover properties for skier triggering of avalanches. *Cold Regions Science and Technology*, *33*(2–3), 207–221.

Sharp, A. E. A. (2018). Evaluating the Exposure of Heliskiing Ski Guides to Avalanche Terrain Using a Fuzzy Logic Avalanche Susceptibility Model. *University of Leeds: Leeds, UK*.

Statham, G. (2020, October 17). Update to the Avalanche Terrain Exposure Scale. *Austrian Association for Snow and Avalanches (AASA)*. https://www.oegsl.at/update-to-the-avalanche-terrain-exposure-scale/ (Accessed: 25 July 2023).

Statham, G., McMahon, B., & Tomm, I. (2006). The avalanche terrain exposure scale. *Proceedings of the International Snow Science Workshop, Telluride, CO, USA*.

Sykes, J., Haegeli, P., & Bühler, Y. (2022). Automated snow avalanche release area delineation in data-sparse, remote, and forested regions. *Natural Hazards and Earth System Sciences*, *22*(10), 3247–3270. https://doi.org/10.5194/nhess-22-3247-2022

Tarboton, D. G. (2005). Terrain analysis using digital elevation models (TauDEM). *Utah State University, Logan*, *3012*, 2018.

Teich, M., Fischer, J.-T., Feistl, T., Bebi, P., Christen, M., & Grêt-Regamey, A. (2014). Computational snow avalanche simulation in forested terrain. *Natural Hazards and Earth System Sciences*, *14*(8), 2233–2248. https://doi.org/10.5194/nhess-14-2233-2014

Toft, H. B., Müller, K., Hendrikx, J., Jaedicke, C., & Bühler, Y. (2023). Can big data and random forests improve avalanche runout estimation compared to simple linear regression? *Cold Regions Science and Technology*, *211*, 103844. https://doi.org/10.1016/j.coldregions.2023.103844

UNESCO. (1981). *Avalanche Atlas Illustrated International Avalanche Classification Atlas Des Avalanches Classification Internationale Illustreint Atlas Des Avalanches: Classification Internationale Illustree Des Avalanches Atlas de Las Avalanchas: Classificacion Inter*. Unesco, International Institute for Educational Planning.

Veitinger, J., Purves, R. S., & Sovilla, B. (2016). Potential slab avalanche release area identification from estimated winter terrain: A multi-scale, fuzzy logic approach. *Natural Hazards and Earth System Sciences*, *16*(10), 2211–2225. https://doi.org/10.5194/nhess-16-2211-2016

Veitinger, J., & Sovilla, B. (2016). Linking snow depth to avalanche release area size: Measurements from the Vallée de la Sionne field site. *Natural Hazards and Earth System Sciences*, *16*(8), 1953–1965. https://doi.org/10.5194/nhess-16-1953-2016

Virtanen, P., Gommers, R., Oliphant, T. E., Haberland, M., Reddy, T., Cournapeau, D., Burovski, E., Peterson, P., Weckesser, W., Bright, J., van der Walt, S. J., Brett, M., Wilson, J., Millman, K. J., Mayorov, N., Nelson, A. R. J., Jones, E., Kern, R., Larson, E., … SciPy 1.0 Contributors. (2020). SciPy 1.0: Fundamental Algorithms for Scientific Computing in Python. *Nature Methods*, *17*, 261–272. https://doi.org/10.1038/s41592-019-0686-2

Voellmy, A. (1955). Über die Zerstörungskraft von Lawinen. *Schweizerische Bauzeitung 73*, 159–165.

Werners, B. M. (1988). Aggregation models in mathematical programming. *Mathematical Models for Decision Support*, 295–305.

Wichmann, V. (2017). The Gravitational Process Path (GPP) model (v1.0) – a GIS-based simulation framework for gravitational processes. *Geoscientific Model Development*, *10*(9), 3309–3327. https://doi.org/10.5194/gmd-10-3309-2017

Wu, K., Otoo, E., & Shoshani, A. (2005). Optimizing connected component labeling algorithms. *Medical Imaging 2005: Image Processing*, *5747*, 1965–1976.

Zadeh, L. A. (1965). Fuzzy sets. *Information and Control*, *8*(3), 338–353. https://doi.org/10.1016/S0019-9958(65)90241-X